UNIVERSITÀ DEGLI STUDI DI TRIESTE

FACOLTÀ DI SCIENZE MATEMATICHE FISICHE E NATURALI

Dipartimento di Astronomia

Tesi di Laurea in Astrofisica e fisica spaziale

Cooling dei barioni cosmici negli aloni di materia oscura:

modelli semi-analitici e simulazioni numeriche

Laureando :
Massimo VIOLA

Relatori :
Prof. **Stefano BORGANI**
Dott. **Pierluigi MONACO**
Dott. **Giuseppe MURANTE**

Controrelatore :
Prof. **Marino MEZZETTI**

Anno Accademico 2006-2007

Presentazione

Una delle sfide più importanti per la cosmologia moderna è la comprensione dei processi fisici che portano alla formazione di una galassia. Negli ultimi anni è stato possibile vincolare in modo sufficientemente preciso (si faccia riferimento a Springel et al. (2006) per una recente review) i valori dei principali parametri cosmologici, grazie soprattutto al numero sempre maggiore di osservazioni indipendenti dell'universo a grande scala. Ciò ha permesso di determinare in modo preciso le condizioni iniziali a partire dalle quali ha avuto luogo il processo di formazione delle strutture. Di conseguenza, comprendere i complessi processi astrofisici, legati all'evoluzione della componente barionica dell'universo, rappresenta oggi il tassello mancante per una descrizione soddisfaccente della formazione ed evoluzione delle galassie.

Fin'ora, per fare delle predizioni quantitative circa le proprietà osservative delle popolazioni galattiche e circa la loro evoluzione nel tempo, si sono seguiti due approcci, alternativi tra loro. Il primo è basato sui così detti Modelli Semi-Analitici. In questo approccio, il background cosmologico predice in modo univoco la formazione gerarchica degli aloni di materia oscura, all'interno dei quali il gas collassa e successivamente si raffredda (cooling), in seguito a perdite radiative di energia, dando origine alla formazione delle galassie. L'interazione reciproca tra il raffreddamento del gas, la formazione stellare, l'arricchimento chimico e il rilascio di energia da parte delle supernovae o degli AGN (Active Galactic Nuclei) viene descritto tramite modellini molto semplici, spesso puramente fenomenologici, che contengono al loro interno una serie di parametri liberi da fissarsi tipicamente a partire dalle osservazioni. Il vantaggio maggiore di questo approccio è il suo basso costo computazionale che permette di esplorare in modo sufficientemente flessibile lo spazio dei parametri del modello.

Il secondo approccio è basato invece sulle simulazioni idrodinamiche, che includono al loro interno la fisica del raffreddamento radiativo del gas e appropiate ricette per la descrizione della formazione stellare e dei meccanismi di feedback. Il vantaggio ovvio di questo metodo, rispetto ai Modelli Semi-Analitici, è che il processo di formazione galattica può essere descritto seguendo nel dettaglio l'evoluzione della componente barionica durante la formazione delle strutture cosmiche su grande scala. Tuttavia la grossa limitazione sta nell'alto costo computazionale, che rende impossibile esplorare nel dettaglio lo spazio dei parametri che descrivono il processo di formazione ed evoluzione galattica.

Appare quindi ovvio che i Modelli Semi-Analitici e le simulazioni numeriche

forniscono approcci complementari nello studio della formazione delle galassie. In particolare, la capacità delle simulazioni idrodinamiche di seguire in modo accurato la dinamica del gas suggerisce di effettuare un confronto con i Modelli Semi-Analitici per testare le assunzioni su cui essi si basano.

Lo scopo di questa Tesi è quello di mostrare in che modo tale confronto sia possibile per lo studio del raffreddamento radiativo del gas.

Il modo migliore per studiare nel dettaglio il comportamento del gas e per testare le assunzioni alla base dei modelli di cooling implementati all'interno dei Modelli Semi-Analitici, è quello di affrontare il problema in una sorta di "laboratorio numerico" dove (eclusa l'idrodinamica) l'unico processo rilevante per la componente barionica è il raffreddamento radiativo e tutte le complicazioni associate al merging gerarchico degli aloni vengono eliminate.

In particolare, abbiamo simulato, mediante un codice SPH (Smooth Particles Hydrodynamics), `GADGET-2`, degli aloni isolati di materia oscura (con un profilo di densità del tipo Navarro et al. (1997)) all'interno dei quali il gas è stato posto in modo tale da essere inizialmente in equilibrio idrostatico. Una volta accertata la stabilità del sistema, è stato acceso il cooling nella simlazione.

Come prima cosa abbiamo accertato la convergenza delle simulazioni, sia rispetto alla scelta del numero di particelle che del softening gravitazionale. Successivamente abbiamo confrontato i risultati delle simulazioni con le predizioni del modello di White & Frenk (1991) (modello classico) e con quelle dei modelli di cooling proposti all'interno del codice MORGANA per la formazione delle galassie (Monaco et al. 2007).

Abbiamo trovato che il raffreddamento radiativo del gas nelle simulazioni idrodinamiche non viene riprodotto nel dettaglio da nessuno dei modelli considerati.

Ci siamo quindi concentrati sulle predizioni dei diversi modelli circa l'evoluzione nel tempo della frazione di gas freddo, che costituisce la materia prima per la successiva formazione stellare ed in generale per il processo di formazione galattica. Abbiamo trovato che il modello classico sottostima in modo significativo tale quantità. Crediamo che tale differenza sia dovuta nei primi istanti dell'evoluzione allo scatter in densità e temperatura (e quindi nel tempo di cooling) delle particelle SPH, e successivamente all'aumento di pressione nelle vicinanze della regione nella quale avviene il cooling. Il modello MORGANA, basato su un insieme diverso di assunzioni, dà invece un fit migliore della frazione di massa raffreddata.

Dal momento che i modelli MORGANA non tengono conto in modo esplicito del comportamento del gas durante il suo raffreddamento radiativo, essi sono da considerarsi come modelli efficaci che possono essere utilizzati per ottenere delle predizioni realistiche ad esempio circa l'evoluzione della frazione di massa fredda.

Il primo passo successivo rispetto a questo lavoro di Tesi potrebbe essere lo sviluppo di un nuovo modello per il cooling che tenga conto esplicitamente dello scatter osservato nelle simulazioni e dell'aumento della pressione del gas.

Successivamente, una volta sotto controllo il raffreddamento radiativo del gas, l'approccio di questa Tesi potrebbe essere esteso allo studio del merging tra aloni di materia oscura per studiare le loro conseguenze sul riscaldamento del gas, oppure

allo studio dei processi di feedback che avvengono all'interno delle galassie.

L'obiettivo finale, che si vuole raggiungere con questi studi, è la diminuzione dei parametri liberi all'interno dei modelli e al contempo una descrizione quanto più realistica (e semplice) possibile della fisica del gas, che permetta in futuro di aumentare il potere preditivo dei modelli di formazione galattica.

Cooling in Dark Matter halos:

Semi-Analytical and numerical modeling

Contents

Introduction

According to the standard cosmological model, our universe is composed by Dark Energy(73%), Dark Matter (DM hereafter) (23%) and baryonic matter (4%). Once the cosmological parameters are fixed, is it possible to explain the formation of structure in the universe starting from the anisotropy seen in the Cosmic Microwave Background (CMB thereafter). All potential and density fluctuations started out small; from CMB temperature fluctuation spectrum we know that the potential fluctuations were of order 10^{-5}. Present-day density contrast within central parts of galaxies are $\simeq 10^5$, and about 10^3 in clusters, so we have to account for many order of magnitudes of growth in fractional over-density. We can divide the evolution of perturbations in two regimes: the liner regime ($\delta\rho/\rho \ll 1$) described analytically by the Jeans theory, and the non linear regime that today is described quite well thanks to numerical simulations.

The growth of the structure is driven (almost) entirely by gravity. Galaxies form when gas cools and condenses in the potential wells of dark matter (DM) halos. Then, as suggested by White & Rees (1978), the formation process must be in two stages: the collisionless collapse of DM halos and the condensation of baryon inside the DM potential wells. The rather stringent constraints on cosmological parameters now allow us to precisely set the initial conditions from which the formation of cosmic structures has started. As a consequence, understanding the complex astrophysical processes related to the evolution of the baryonic component represents now the missing link towards a successful description of galaxy formation and evolution. Two alternative approaches have been pursued to make quantitative predictions of the observational properties of galaxy populations and their evolution in the cosmological context. The first one is based on the so–called semi–analytical models (SAM hereafter). In this approach, the background cosmological model uniquely predicts the hierarchical build–up of the DM halos, where gas flows in, cools and gives rise to the formation of galaxies; the complex interplay between gas cooling, star formation, chemical enrichment and release of energy from supernova explosions and Active Galactic Nuclei (AGN) is modeled in a parametric way. A posteriori, the values of the relevant parameters should then be constrained by comparing SAM predictions to observational data. The second approach is based on resorting to full hydrodynamical simulations, which include the processes of gas cooling and suitable sub–resolution recipes for star formation and feedback. The obvious advantage of this methods, with respect to SAMs, is that the process of galaxy formation is described by following in details the evolution of

the cosmic baryons during the shaping of the large–scale cosmic structures. However, its limitations lie in its high computational cost, which makes it impossible to explore in details the space of the parameters describing the process of galaxy formation and evolution. This discussion demonstrates that SAMs and hydrodynamical simulations provide complementary approaches to the cosmological study of galaxy formation. The capability of hydrodynamical simulations in accurately following gas dynamics calls for the need of a close comparison between these two approaches, in order to test the basic assumption of the SAMs. The best regime to perform this comparison is when one excludes the effect of all those processes, like feedback in energy and metals, whose different modeling in SAMs and simulations codes would make the comparison scarcely telling. Since the gas cooling is the most basic ingredient in any model of galaxy formation, an interesting comparison would be performed when cooling is the only process turned on.

The purpose of this Thesis is that of presenting a detailed comparison between the predictions of cooling models, as implemented in SAMs, and results of hydrodynamical simulations in which gas is allowed to cool inside isolated halo.

The plan of the Thesis is as follows: in **chapter 1** we will discuss the galaxy formation process, pointing out the different role that DM and gas have in such process. Moreover we will concentrate on the possibility to combine SAMs and numerical simulations in order to improve the ability in the explanation of galaxy formation.

Chapter 2 will be devoted to the description of the structure of DM halo, that is one of the fundamental things that must be understood in order to follow properly the formation of a galaxy. We will also show how it is possible, under suitable assumptions, to derive an analytical expression for the gas density profile when the gas is assumed to be embedded in a DM halo.

Since the core of this Thesis is gas cooling, we describe in **chapter 3** the most important atomic processes that take place in an optically thin plasma (which is a good approximation for the gas in DM halos) and that are responsible for the gas radiative cooling. Moreover we will show how it is possible to collect together all the information coming from atomic processes to calculate a so–called "cooling function" for the plasma.

In **chapter 4** we will present and critically discuss (mainly theoretically) two different recipes for gas cooling, implemented in SAMs. The first one, that we call "Classical cooling model" was proposed for the first time by White & Frenk (1991) and is implemented in most of SAMs, while the second one, referred as "MORGANA cooling model", was proposed more recently by Monaco et al. (2007).

Chapter 5 will be dedicated to numerical simulations. We will discuss in details hydrodynamical simulations, presenting the different equations integrated by the Smoothed–Particles–Hydrodynamics (SPH) codes. In particular we will concentrate on the `GADGET-2` code (Springel et al. (2001),Springel et al. (2005)), which is the ones used to perform the simulations used in this Thesis.

In **chapter 6** we will present the details of the simulations that we have performed. In particular we will show how the initial conditions for the isolated halos

have been generated, and we will make a qualitative analysis of radiative simulations (i.e. the simulations in which cooling is turned on).

In the last chapter (**chapter 7**) we will discuss the cooling models, described in chapter four, in the light of numerical simulations. The goal of this chapter is to point out which of the cooling recipes described in chapter four gives the most reliable description of the radiative cooling in numerical simulations.

In **Appendix A** we will present briefly the main result of the general relativity theory and the Friedmann cosmological models that is the framework for the description of the evolution of perturbations. The perturbation theory will be therefore present in **Appendix B**.

The results of this Thesis are contained in a paper (Viola et al., 2007) which will be submitted for pubblication to MNRAS (Monthly Notices of the Royal Astronomical Society).

Chapter 1

Galaxy formation in cosmological models

Understanding galaxy formation is one of the most challenging and difficult topics in modern cosmology. The idea that cosmic structures grow up through the mechanism of gravitational instability is the oldest part of the paradigm. The application of perturbation theory (see appendix B) and numerical simulations (see chapter 5) to understand this process started in the early 1970s (Peebles, 1980). Gunn & Gott (1972) looked at the growth of galaxy clusters through the infall of material, using the spherical top–hat model (see appendix B.2) to track the evolution of the cluster over-density. Press & Schechter (1974) used the top–hat model to compute the abundance of structures of different masses that form by gravitational collapse in a density field with a Gaussian distribution of fluctuations. The first calculation of the pattern of density fluctuations expected at early time in a cold dark matter (CDM hereafter) universe was made by Peebles (1982). The first numerical simulations of the hierarchical growth of structures in a CDM universe were carried out by Davis et al. (1985). Two of the core ideas at the basis of today's paradigm of galaxy formation can be traced back more than fifty years ago to Fred Hoyle. Hoyle (1949) was the first to propose that the rotation of galaxies could be generated by the tidal torques which operate during their collapse. This idea was expanded upon by Peebles (1969) and White (1984), and tested with N–body simulations by Efstathiou & Jones (1979). Hoyle also argued that the observed range of galaxy masses could be explained by considering the time taken for gas to cool and condense into galaxies (Hoyle, 1953). At the end of 1970s, White & Rees (1978) presented a synthesis of the theory of Press & Schechter, which describes the hierarchy of gravitational bound structures, and the gas cooling arguments used to motivate the observed size of galaxies, to produce a model of galaxy formation that set the foundations for today's models. They proposed that galaxy formation was a two stage process, with DM halos forming in a dissipationless, gravitational collapse, with galaxies forming inside these structures, following the radiative cooling of the baryons. The additional condensation of gas through dissipative cooling stabilized galaxies against the disruption caused by the merging of the DM halos. White &

Rees (1978) also argued that an additional process, feedback, was needed to make small galaxies more diffuse so that they would be less successful at surviving the merging process. As we have already mentioned in the introduction, two alternative approaches have been pursued to make quantitative predictions on the observational properties of the galaxy population and their evolution in cosmological context. The first one is based on the so–called semi–analytical models, briefly described in this chapter, while the second approach is based on resorting to full hydrodynamical simulations, which include the processes of gas cooling and suitable sub–resolution recipes for star formation and feedback. The obvious advantage of this methods, with respect to SAMs, is that the galaxy formation can be described by following in details the evolution of the cosmic baryons during the shaping of the large–scale cosmic structures. However, its limitations lies in its high computational cost, which makes it impossible to explore in details the space of the parameters describing the process of galaxy formation and evolution.

1.1 Dissipationless universe

In this section we will review the "first stage" of the galaxy formation, i.e. the growth and the dissipationless collapse of DM perturbations. Our starting point is to specify the cosmological background. The current "standard model" is a CDM universe with a cosmological constant (see Appendix A). In the cold dark matter model the process of perturbation growth is dissipationless. This means that the total kinetic and potential energy of a system of DM is conserved, although energy can be converted from potential to kinetic. Once the values of the basic cosmological parameters have been set, such as the density parameter of matter (Ω_M), the cosmological constant (Ω_Λ), the density parameters of baryons (Ω_b) and the current amplitude of the density fluctuations on some reference scale, the pattern of primordial density fluctuation is well determined and the timetable for their collapse into gravitationally bound structures is set. DM halos are the cradles of galaxy formation and the hierarchical galaxy formation models require three basic pieces of information about DM halos:

1. The abundance of halos of different masses;

2. The formation history of each halo, commonly called the merger tree;

3. The internal structure of the halo.

In the following subsections we will discuss this three points.

1.1.1 The abundance of DM halos

The first attempt to calculate the abundance of gravitationally bound structures was made by Press & Schechter (1974). They assumed a Gaussian density field, $\delta(\bar{y})$, for the primordial perturbations. They smoothed this field on a length–scale R (or equivalent on a mass–scale $M \propto \langle \bar{\rho} \rangle R^3$) :

$$\delta(\bar{x}) = \int \delta(\bar{y}) W_R(|\bar{x} - \bar{y}|) d\bar{y} \tag{1.1}$$

where $W_R(|\bar{x}|)$ is a "window function" that suppresses perturbations mode at a length–scale less than R. The original idea was to identify all the observable structures of mass M with the over-dense regions, exceeding a critical value δ_c, in the primordial density field . When the critical value is attained (in a EdS universe it is $\delta_c = 1.686$, as it shown in B.2) the over-dense region rapidly collapses. The structure formation takes place then hierarchically. Fixing now the smoothing scale R, the probability for a Gaussian field $\delta(\bar{x}, M)$ to exceed the critical value δ_c is;

$$P(\delta_c, M) = \frac{1}{\sqrt{2\pi}\sigma_M} \int_{\delta_c}^{\infty} \exp\left(-\frac{\delta}{2\sigma_M^2}\right) d\delta \tag{1.2}$$

where

$$\sigma_M^2 = \frac{\langle \delta M^2 \rangle}{\langle M \rangle^2} \tag{1.3}$$

From the above expression, we recognize a serious drawback of the Press & Schechter approach. Infact, taking $dP(\delta_c, M) = -(\partial P(\delta_c, M)/\partial M)dM$ to be the fraction of the total mass in structures with mass between M and $M + dM$, its integral over the whole mass spectrum is $\int_0^{\infty} dP(\delta_c, M) = \frac{1}{2}$ and it fails to account for half the mass in the Universe. The origin of this problem lies in the fact that equation 1.1.1 does not actually provide the fraction of mass in structures greater than M. For this to be the case, the mass in region where $\delta < \delta_c$ sholud be assaigned to structures of a greater mass, when smoothing the field on a larger scale.

Press & Schechter (1974) adopted a pragmatic approach to solve this problem and multiplied their expression for the halo mass function by a factor of two. Taking into account that artifact the number density of halos with mass in the interval $[M, M + dM]$ is:

$$n(M)dM = -\frac{2}{V_R} \frac{\partial P(\delta_c, M)}{\partial M} dM \tag{1.4}$$

where V_R is the volume corresponding to a windows with dimension R.

With some computations it is possible to get the following expression for the "mass–function":

$$\frac{dn}{dM} = \sqrt{\frac{2}{\pi}} \frac{\bar{\rho}}{M^2} \frac{\delta_c(z)}{\sigma_M} \left| \frac{d\log\sigma_M}{d\log M} \right| \exp\left(-\frac{\delta_c^2(z)}{2\sigma_M^2}\right) \tag{1.5}$$

More convincing arguments have been put forward for the missing factor of 2, which led to the development of "extended Press–Schechter" theory (Peacock & Heavens (1990), Bond et al. (1991), Bower (1991)...). The mass function predicted by this simple calculation agrees surprisingly well with the results obtained from N–body simulations (e.g. Efstathiou et al. (1988), Lacey & Cole (1994), Gross et al. (1998)). The accuracy with which the mass function of halos can now be predicted using N–body simulations has led to refinements in the Press–Schechter ansatz. Sheth

et al. (2001) presented a model in which the collapse of a fluctuation is allowed to proceed more quickly along one axis, replacing the spherical collapse model with an ellipsoidal collapse. Jenkins et al. (2001) established the mass function of halos over four decades in mass using a suite of N–body simulations and proposed a fitting formula that encapsulates the numerical results. An extension of this work to five orders of magnitude in mass was carried out by Springel (2005) and Warren et al. (2006).

Monaco et al. (2002) proposed a new approach for obtaining the information on the assembly history of DM halos, based on the Lagrangian Perturbation Theory (see (Moutarde et al., 1991),(Buchert & Ehlers, 1993),(Catelan, 1995) and on the Zel'dovich (1970) approximation. This algorithm, called Pinocchio (PINpointing Orbit-Crossing Collapsed HIerarchical Objects) can accurately reproduce many properties of the DM halos when compared with a N–body simulation that started from the same initial density field.

1.1.2   The assembly of DM halos

Once the first halos are formed through the collapse of primordial perturbations, they start merging together due to gravitational attraction. One of the crucial points in the description of the formation of galaxies is the reconstruction of the merging history of the DM halos present today in our universe (see figure 1.1 for a schematic merger tree of a DM halo). The merger history of DM halos can be extracted from N–body simulations which have sufficiently frequent output. This requires typically around 50 outputs over a redshift interval of approximately $z = 20$ to $z = 0$. Halos are identified in a given output using a percolation algorithm, such as friends–of–friends (Davis et al. (1985)). The idea is to define a "linking length" as a part of the mean inter-particle separation (White (2002)) and then to link together all the particles that are within the linking length of one another. In this way it is possible to identify the halos. Then the indices of the particles that belong to a particular halo can be tracked in the halo list generated from the preceding output.

Merger trees can also be generated using a Monte–Carlo approach by sampling the distribution of progenitor masses predicted using extended Press-Schechter theory (Lacey & Cole (1994), Somerville & Primack (1999), Cole et al. (2000a)). Monte–Carlo approach gives in general a less faithful representation of the merger tree than those extracted from N–body simulations. This happens especially if the difference in expansion factor increases between the parent halo and the progenitor branches (e.g. Somerville et al. (2001)). A fundamental assumption that underpins the Monte–Carlo approach to growing merger tree is that the formation history of the halo does not depend upon its environment. Early simulation results appeared to validate that assumption (Lemson & Kauffmann (1999), Percival et al. (2003)). However some of these results have recently been reanalyzed and found to show evidence in favor of an environmental dependence of halo properties (Sheth & Tormen (2004)). This effect was confirmed by recent analyses of the properties of
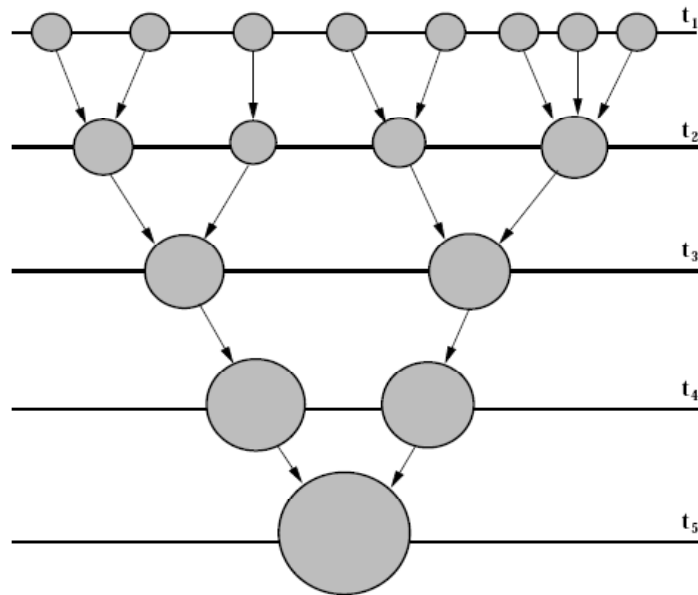
Figure 1.1: A schematic merger tree for a DM halo. The horizontal lines represent snapshots in the evolution of the history of the halo, corresponding to time-steps in an N–body simulation or Monte–Carlo realization of the merger tree ($t_1 < t_2$). The size of the circle indicates the mass of the halo. The halos grow through merger events between halos and by accretion of objects below the halo mass resolution (e.g. as depicted between steps t_3 and t_4). The final halo is shown at t_5. (Baugh (2006))

DM halos in a large volume, high resolution simulations (Gao et al. (2005), Harker et al. (2006), Wechsler et al. (2006), Reed et al. (2007), Zhu et al. (2006)). Both approaches, extracting the trees directly from an N–body simulation and growing Monte–Carlo trees, have their pros and contra. The N–body trees allow one to connect galaxies directly between outputs in the simulations and give predictions for galaxy positions within the halos. Overall, they are more accurate and incorporate the environmental effects. However, the N–body trees are not without problems. Objects, that a group finder has identified as one structure in a given output, may actually fly apart in a later output; spatial proximity doesn't guarantee that particles belong to a bound, self–gravitating structure. Furthermore, when objects do merge together, the mass of the remnant may not always be equal the mass of the progenitor. These two effects imply that the mass of a halo in a merger tree extracted from an N–body simulation may not always increase monotonically with time. The smallest halo that can be reliably identified as self–gravitating structure, does not, by definition, have a merger history that can be extracted from the simulation. The main drawback of N–body merger trees is their finite resolution (see Helly et al. (2003)). Monte–Carlo trees, on the other hand, can, in principle have arbitrarily high resolution, because all the computer memory can be devoted to one tree at a time, rather than to all the halos within some cosmological volume.

1.1.3 The structure of DM halos

As it will be clear in the following, the internal structure of DM halos is important for determining the rate at which gas can cool and the size and dynamics of galaxies. The first studies about the density profiles of DM halo have been done at the beginning of the 1970s. Gunn & Gott (1972) established, with their "secondary infall model", that gravitational collapse could lead to the formation of virialized system with almost isothermal density profile. This analytical work was extended by Hoffman & Shaham (1985) and Hoffman (1988), who pointed out that the structure of halos should also depend on the value of the density parameter Ω_M and the power spectrum of initial density fluctuation. It has become customary, until ten years ago, to model virialized halos by isothermal spheres characterized by two parameters: a velocity dispersion and a core radius. However numerical simulations of the formation of galactic halos and galaxy clusters provide no firm evidence for the existence of a core (Dubinski & Carlberg (1991), Warren et al. (1992),Navarro et al. (1996), Moore et al. (1998), Power et al. (2003), Navarro et al. (2004)...). These studies indicate that DM halos are not well approximated by isothermal spheres. The density profile of the DM halo varies with radius within the halo. Navarro et al. (1997) reported a density profile that is significantly shallower than $\rho \propto r^{-2}$ near the center but which tends to r^{-3} as the virial radius is approached. However over much of the radius, an isothermal halo density profile, $\rho \propto r^{-2}$, is a reasonable description. A complete treatment of the NFW profile will be done in the section 2.1.

1.2   Physics of the gas

In this section we outline the more complicated elements of hierarchical galaxy formation regarding the physics of the gas. These processes are often dissipative and non–linear and the physics behind these phenomena are in general poorly understood. Therefore it is very difficult to describe them properly and most of the time recipes or prescriptions which contain parameters are employed. The value of the parameters are set by requiring that the model reproduces a subset of the available observations, typically low redshift data. The form of the rule adopted to describe a process is motivated by a result from a more detailed numerical simulation or from observations.

1.2.1   Shock heating

When a non–linear perturbation decouples from the uniform expansion of the universe, it starts collapsing as a separate closed universe. It is reasonable to assume that virial equilibrium is reached at the end of the collapse:

$$2E_K + E_\Phi = 0 \tag{1.6}$$

where E_K is the kinetic energy and E_Φ is the potential energy. During the collapsing phase the gas is assumed to be heated through violent relaxation processes and shock waves up to an equilibrium temperature called *virial temperature*:

$$T_{vir} = \frac{\mu m_p \sigma^2}{3k_B} \tag{1.7}$$

where μ is the molecular weight of the gas, m_p the proton mass, σ the velocity dispersion and k_B the Boltzmann constant.

1.2.2   Gas cooling

The cooling of the gas is central to the process of galaxy formation, as it sets the rate at which the raw material for star formation becomes available (Blumenthal et al. (1984)). The cooling models are the core of this Thesis and therefore they will be treated in details in chapter 4. Here we just describe the schematic picture of the standard cooling model used in SAMs (see figure 1.2).

The gas initially has the same spatial distribution as the DM (t_1). As fluctuations in the DM separate from the Hubble expansion, turn around and collapse, the gas is assumed to be heated by shocks as it falls into the gravitational potential well of the DM halo, producing a hot gas halo that is supported against further collapse by the pressure of the gas (step t_2). The gas attains the virial temperature of the halo and start cooling radiatively through the mechanisms outlined in chapter 3. As the gas cools, the pressure of the gas drops and the removal of pressure support means that the gas sinks to the center of the halo (step t_3). The gas at the center of the halo advance outwards towards the virial radius of the halo and the cold disc, formed in step t_3, grows in size. The different cooling recipes implemented in SAMs will be described in detail in chapter 4.
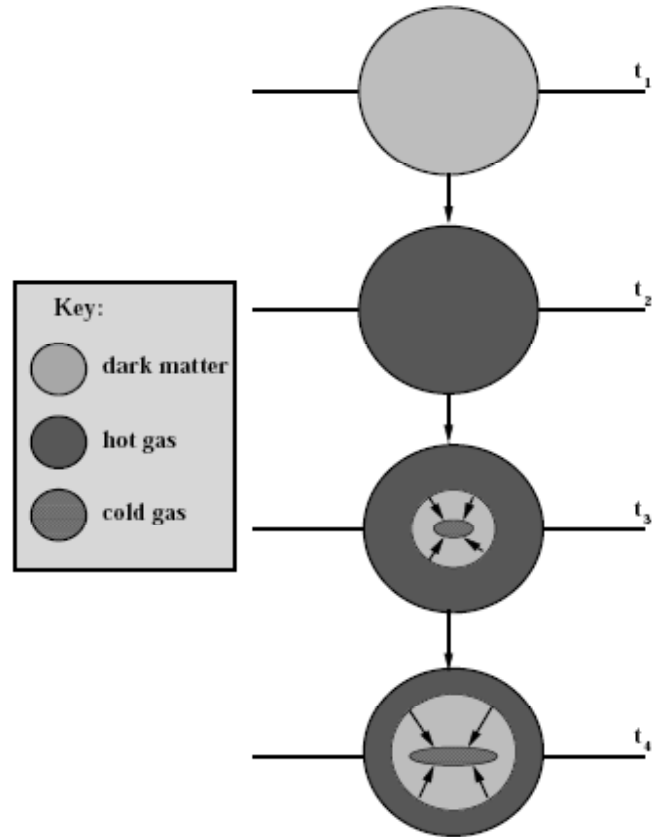
Figure 1.2: A schematic of the basic cooling model used in SAMs. In the first step t_1, baryons fall into the gravitational potential well of the DM halo. This gas is assumed to be heated by shocks as it falls into the potential well, attaining the virial temperature associated with the halo (t_2). In the third step (t_3), the inner parts of the hot gas halo cool, forming a rotationally supported disc. At later stage t_4, the radius within which gas had time to cool advances outwards towards the virial radius of the halo and the cold gas disc grows in size. (Baugh (2006))

1.2.3   Star Formation

Star formation takes place in the cooled gas cloud if their self–gravity is sufficient to overcome thermal pressure. For a uniform cold gas cloud of radius R, mass M, temperature T, density ρ and mean molecular weight μ this means:

$$M > M_J = \left(\frac{3k_B T}{2G\mu m_p} \right)^{3/2} \left(\frac{4\pi\rho}{3} \right)^{-1/2} \tag{1.8}$$

M_J is the so–called *Jeans Mass*. There are a wide range of theories of star formation from gas clouds which attempt to explain the slope of the Initial Mass Function (IMF) and the rate of star formation in galaxies. Semi–analytical modelers use to estimate the global rate of star formation on dimensional ground:

$$\dot{M}_\star \propto \frac{M_{cold}}{\tau} \tag{1.9}$$

where the star formation rate, $\dot{M}_\star$, depends upon the amount of cold gas available, M_{cold}, and a characteristic time-scale τ. The time-scale could be chosen to be proportional to the dynamical time within the galaxy, $\tau_{dyn} = r_{gal}/v_{gal}$, or to be some fixed value. Typically, some additional dependence on the circular velocity is incorportaed into the definition of τ, which is important when attempting to reproduce the observed gas fractions in spirals as a function of luminosity. The *effective* star formation timescale is in practice a modified version of *tau*, due to feedback processes, which deplete the reservoir of cold gas, and the replenishment of the cold gas supply by material that is recycled by stars.

1.2.4   Feedback processes

The need for physical mechanisms that are able to modulate the efficiency of galaxy formation as a function of halo mass, over and above the variation in the cooling time of the hot gas with halo mass, was recognized from the first calculations of the galaxy luminosity function in hierarchical clustering cosmology. In particular White & Rees (1978) found that their prediction for the faint end of the luminosity function was steeper than the observational estimates available at that time. All the different processes evocated to solve this problem are simply called *feedback processes*. Broadly speaking, two forms of feedback are considered in galaxy formation models: in the first, cold gas is heated and removed from a galactic disk and in the second, the rate at which gas cools from the hot halo is suppressed. Both modes of feedback diminish the reservoir of cold gas available to be turned into stars. The most common form of feedback used is the ejection of cold gas from a galactic disk by a supernova driven wind (Larson (1974), Dekel & Silk (1986)). The re-heated cold gas cloud be blown out to the hot gas halo, from which it may subsequently re-cools. There are now convincing observational evidence for the existence of supernova driven winds in dwarf galaxies (Martin (1997), Martin (1998), Martin (1999), Ott et al. (2005)).

Other forms of feedback act to modify the rate at which gas cools, either by altering the density profile or entropy of the hot gas (following the injection of energy into the hot gas halo) or by reducing the fraction of baryons that fall into DM halos and changing the cooling rate (i.e. photoionization suppression of cooling in low mass halos) or by stifling the cooling flow by injecting energy (Wu et al. (2000), Bower et al. (2001), Benson et al. (2003), Granato et al. (2004), Bower et al. (2006)). In recent years, the focus has shifted to reproduce the exponential cut off at the bright end of the luminosity function. Various fixes have been proposed to this problem. Kauffmann et al. (1993) suppressed the number of bright galaxies simply turning off star formation by hand in the cooling flows present in high circular velocity halos. Cole et al. (2000b) proposed that the hot gas follows a different density profile from that exhibited by the DM. An additional feedback mechanism is required that is effective in more massive halos, acting either to prevent gas from cooling in the first place or to eject gas before it forms stars. The standard supernova driven winds, while helping to reduce the number of faint galaxies to match observations, were found to have a little effect at the bright end. Benson et al. (2003) considered two more promising mechanism: thermal conduction in the hot halo and "super-winds" (the ejection mode of supernova feedback).

Another feedback mechanism implemented in SAMs in the last years is the so–called Active Galactic Nuclei (AGN) feedback. Croton et al. (2006) and Bower et al. (2006) use it in order to suppress gas cooling only in those halos in which a quasi–static hot halo has formed, i.e. where the cooling time of the gas exceeds the free–fall time. The new models reproduce the observed break in the present day luminosity and the bimodality of the color distribution of local galaxies (as measured by Kauffmann et al. (2003), Baldry et al. (2004), Balogh et al. (2004)). Bower et al. examined the predictions of their model with AGN feedback at high redshift. They find remarkably good agreement with observational estimates of the stellar mass function to $z \sim 5$. Other groups have also developed SAMs in which AGN act to suppress cooling, such as Cattaneo et al. (2006), Fontanot et al. (2006), Menci et al. (2006), Monaco et al. (2007).

1.2.5 Disc Formation

We have already described how the baryonic gas in DM halos cools down forming self–gravitating cold clouds where star formation and feedback processes take place. Catelan & Theuns (1996) have shown how, due to tidal torques by the large scale structure, the DM halos gain angular momentum J. It is possible to assume that the baryonic matter acquires the same specific J. For an isolated system the mass M, energy E, and angular momentum J are all conserved under gravitational evolution. The spin of the halo can be quantified in a dimensionless number λ:

$$\lambda = \frac{|J||E|^{1/2}}{GM^{5/2}} \tag{1.10}$$

If the conservation of angular momentum during the dissipative collapse of the gas is assumed, then the factor by which the radius of the gas is reduced is $\sim 0.5\lambda_H$

(Fall & Efstathiou (1980)). N–body simulations indicate $\lambda \sim 0.04$ (Efstathiou & Jones (1979), Frenk et al. (1988), Bullock et al. (2001)), which means that the gas collapses to a rotationally supported disk with a radius over an order of magnitude smaller than the virial radius of the dark halo. This simple argument has been used to predict disc properties (Mo et al. (1998)) and to estimate the sizes of galaxies in many SAMs (Lacey & Cole (1993), Kauffmann & Charlot (1994), Poli et al. (1999), Somerville & Primack (1999), Firmani & Avila-Reese (2000)...)

1.2.6   Bulge formation

It is easy to prove that not all the possible disc configuration reached with the mechanism described in the previous section are stable. In fact, when the self–gravity becomes dominant, the disc is dynamically unstable to the formation of a bar. Disc instability results in the stellar disc evolving into a bar and then into a spheroidal buldge. Bulge formation is also due to the interaction of the galaxy with the environment and with other objects, both through process of disc instability and merging.

1.2.7   Galaxy merger

During hierarchical clustering DM halos merge continuously, increasing their masses. Satellite galaxies loose their angular momentum due to dynamical friction and merge with the central galaxy, but they can also merge with others satellites in case of binary encounters. The product of the merging event depends on the masses of the progenitor.

The impact of a galaxy merger is usually quantified by the ratio of the mass of the accreted satellite galaxy to the mass of the central galaxy. In a violent merger, the disk of the central galaxy is assumed to be destroyed and all of the stars involved in the merger event form a spheroidal remnant. In many models, a major merger can also trigger a burst of star formation, in addition to changing the morphology of the star distribution (Baugh et al. (1996), Somerville et al. (2001), Baugh et al. (2005)). The properties of the resulting objects depend on the ratio between masses and orbital parameters, If a disk galaxy accretes an object of mass greater than 20–30 percent of its own mass, both theoretical arguments and numerical experiments suggest that the stellar disk will be disturbed and may no longer resemble a "typical" spiral disk. Detailed N–body simulations show that the result of such an event has the kinematical properties of an elliptical galaxy.

1.3   Semi–analytical models & direct simulations

In this section we will discuss how it is possible to combine SAMs and numerical simulations in order to improve our ability in the explanation of galaxy formation. It is not the aim of this Thesis performing this comparison for all the different processes presented in the previous section. Therefore we will concentrate only

on the construction of the merger tree and on gas cooling, that is the physical mechanism studied in detail in this Thesis. For a general review about the other process we refer to Baugh (2006).

1.3.1 Merger tree

The merger tree, as we have already discussed, is the foundation of any SAM. Two approaches can be used to build it: Monte–Carlo, based on the extended Press–Schechter theory, and N–body simulations. We can summarize as following the pros and cons of the two methods: Monte–Carlo trees tend to become progressively more inaccurate as they are followed over a long interval in time, but has not any resolution problems. On the contrary the main problem of N–body merger trees is limited mass resolution. Today one of the best available N–body simulation in terms of providing high resolution merger trees over a wide range of masses within a single computational box is the so–called "Millennium simulation" (Springel et al. (2005)). However it is still only able to yield trees whose mass resolution is a factor of three poorer than the standard Monte–Carlo trees used, for example, in the Cole et al. model. Helly et al. (2003) carried out a systematic study of the impact of using N–body merger trees on the predictions of the SAMs. They found that, using N–body merger trees instead of Monte–Carlo ones, the prediction for the luminosity function for objects brighter than around one tenth of $L_\star$ (typical luminosity of a bright galaxy, $L_\star \sim 4 \cdot 10^{10} L_\odot$) is similar. Also the predicted star formation–rate per unit volume are similar over the bulk of the history of the universe, diverging only at $z > 1$, beyond which the N–body trees underestimate the amount of star formation. They also found that the results obtained with N–body trees can be reproduced if two adjustments were made to the Monte–Carlo trees. Firstly, they set the resolution of the Monte–Carlo trees to match the minimum halo mass available in the N–body trees. Secondly, they applied an empirical correction to the distribution of progenitor masses expected in extend Press–Schechter model, in order to boost the number of massive halo progenitors.

1.3.2 Gas cooling

As we have stressed before, gas cooling is the heart of SAMs of galaxy formation. We will see in detail in the following chapters how the recipes for gas cooling are generally very simple and make very strong and restrictive assumptions. It is therefore essential to test the accuracy of the cooling model against the result of gas dynamics simulations, which treats the problem under less restrictive conditions. Particularly, semi–analytic cooling models can be tested by designing a numerical simulation in which the less understood phenomena, namely star formation and feedback, are simply omitted. Once numerical simulators, using different codes and algorithm, seem to agree upon the radiative cooling of the gas, it is wise calibrating in this way the simple cooling recipes implemented in SAMs. In this spirit, Benson et al. (2001) compared the cold mass functions in a SPH simulation with radiative

cooling and a "stripped–down" SAMs using Monte–Carlo merger trees, finding similar properties of the corresponding galaxy populations. Similar conclusions were also reached by Helly et al. (2003) and Cattaneo et al. (2006), who used hydrodynamical simulations within cosmological boxed at improved resolution. Yoshida et al. (2002) also performed a similar comparison, but for a simulation of a single galaxy cluster. Also in this case, their claim is that, once the SAM codes are "downstripped" to treat only the effect gas cooling, the two methods provide comparable galaxy populations, at least within the model uncertainties. The level of agreement found by these studies is reassuring. Despite the encouraging results, there has been much debate in the literature regarding the validity of the cooling recipes used in SAMs. While the general agreement between the two methods represent a quite good step, still all the above analyses generally concentrate on comparing the statistical properties of the galaxy populations. Furthermore, if one wants to test the reliability of the cooling model implemented in the SAMs, the cleanest approach would be that of turning–off the complications associated to the hierarchical merging of halos, thereby allowing gas to cool in isolated halos. The purpose of this Thesis is exactly that of presenting a detailed comparison between the predictions of cooling models, as implemented in SAMs, and results of hydrodynamical simulations in which gas is allowed to cool inside isolated halos. In chapter 6 we will describe how such comparison has been done.

Chapter 2

DM halos: gas and DM profiles

We have already discussed in Chapter 1 that the formation of structure in the universe can be divided into two stages: the collisionless collapse of DM halos and the condensation of baryon inside the DM potential wells. Furthermore we have discussed how, in order to follow properly the formation of a galaxy, one of the fundamental things that must be known is the structure of the DM halo. In this chapter we will study this point, and particularly we will try to address to following questions: What is the shape of DM halos ? How does the gas sit in the DM halos after their formation ?

2.1 Dark matter density profile

Gunn & Gott (1972), Fillmore & Goldreich (1984) tried to answer the question about the shape of DM halos from a theoretical point of view. They investigated self–similar collapse solutions assuming a defined symmetry for the system (planar, cylindrical, spherical) and finally derived analytical models for spherical collapse of cold, collisionless matter in a perturbed EdS universe. Building of this work, Hoffman & Shaham (1985) extended the analysis by considering open universe and by modeling as scale–free spherical perturbations the objects that form by hierarchical clustering from power–law initial density spectra $P(k) \propto k^n$. They proposed that virialized DM halos should have a power–low radial profile $\rho(r) \propto r^{-\alpha}$, where α is related to the logarithmic slope n of the power spectrum on the scale of interest. For $n < -1$, the slope relevant on galaxy scale, the prediction is $\alpha = 2$, corresponding to flat rotational curves such as those observed for the baryonic component of galaxies. For $n > -1$ the profiles steepen to $\alpha = (9 + 3n)/(4 + n)$, corresponding to falling rotation curves. This prediction have been supported by many N–Body simulations(e.g.Quinn et al. (1986), Zurek et al. (1988), Warren et al. (1992), Crone et al. (1994), Zaroubi et al. (1996)). However, high resolution simulations (e.g. Frenk et al. (1988)) showed a steepening of the density profile with radius. Navarro et al. (1995) and Navarro et al. (1996) found that a good fit for the DM density profile is given by:

$$\rho(r) = \rho_{crit}\frac{\delta_c}{(r/r_s)(1 + r/r_s)^2} \tag{2.1}$$

where r_s is a scale radius, δ_c is a characteristic (dimensionless) density, and $\rho_{crit} = 3H^2/8\pi G$ is the critical density for closure. This profile is commonly called *Navarro–Frenk–White profile* (NFW hereafter). This profile is singular (although the potential and mass converge near the center) and has a well–defined scale in which the profile changes shape, the scale radius r_s. In figure 2.1 we plot the profile described in equation 2.1 varying the so called "concentration parameter" (dimensionless) defined as:

$$c = \frac{r_{200}}{r_s} \tag{2.2}$$

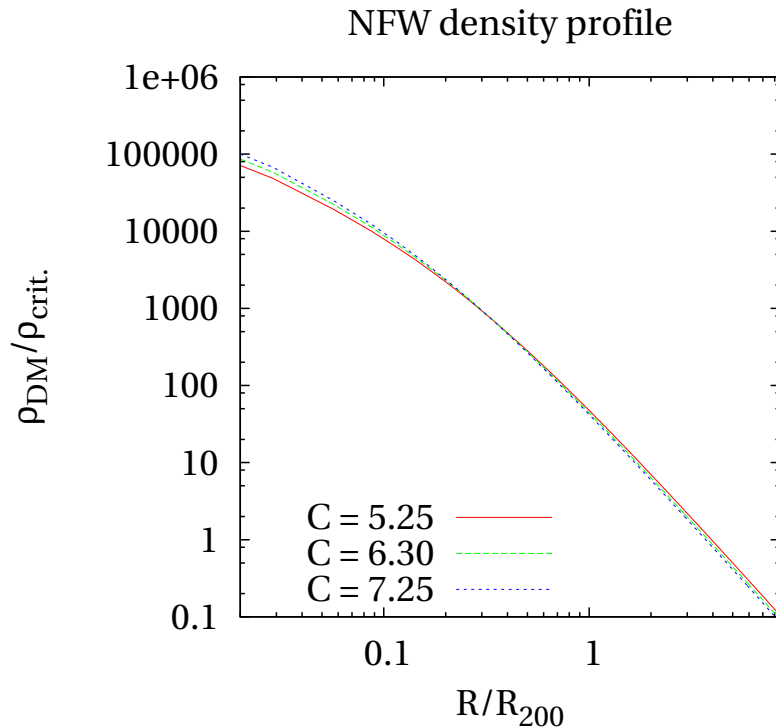where r_{200} is the radius that encompasses an over-density 200 times the critical cosmic density.

Figure 2.1: NFW dark matter density profile for an halo of $M = 10^{13}M_\odot$ varying the concentration parameter c.

The most surprising result was that this profiles is universal for all hierarchical clustering models, regardless of the halo mass, the initial power spectrum, or cosmological parameters.

2.2   Gas density profile

In this section we will show how it is possible, under some assumption, to derive an analytic expression for the gas density profile when it is assumed to be embedded in a DM halo described by eq. 2.1. Before starting, we write the NFW profile in a more compact manner that will be useful in the following calculations:

$$\rho_{\text{DM}}(r) = \rho_s y_{\text{DM}}(r/r_s) \tag{2.3}$$

where ρ_s is a normalization factor with units of mass density, while $y_{DM}(x)$ is a dimensionless function representing the profile:

$$y_{\text{DM}}(x) = \frac{1}{x(1+x)^2} \tag{2.4}$$

where $x = r/r_s$.

From equation 2.3 we can obtain an expression for the mass inside a certain radius r :

$$M(\leq r) = 4\pi\rho_s r_s^3 m(r/r_s) \tag{2.5}$$

where $m(x)$ is a dimensionless mass profile given by

$$m(x) = \int_0^x du u^2 y_{\text{DM}}(u) \tag{2.6}$$

Note that $y_{\text{DM}}(u)$ must be shallower than u^{-3} in the central region for the mass to converge. This is the case of NFW profile.

We define the total DM mass, M_{200}, as the mass within r_{200}, i.e, $M_{200} = M(\leq c)$, where c is the concentration parameter defined in equation 2.1.

By evaluating equation 2.5 at r_{200}, we fix the normalization factor as:

$$\rho_s = c^3 \frac{M_{200}}{4\pi r_{200}^3 m(c)} \tag{2.7}$$

We calculate the virial radius with the spherical collapse model (Peebles (1980))

$$r_{vir} = \left(\frac{M_{vir}}{(4\pi/3)\Delta_c(z)\rho_c(z)} \right) \tag{2.8}$$

Here $\Delta_c(z)$ is a spherical over-density of the virialized halo within r_{200} at redshift z, in units of the critical density of the universe $\rho_c(z)$. Lacey & Cole (1993) and Nakamura & Suto (1997) provide the expression of $\Delta_c(z)$ for arbitrary cosmological models.

Using equation 2.4 it easy to give an explicit expression for the mass :

$$m(x) = \int_0^x du u^2 y_{DM}(u) = \ln(1+x) - \frac{x}{1+x} \tag{2.9}$$

As it is suggested by Komatsu & Seljak (2001), since the DM density is assumed to be self similar, a gas density profile $\rho_{gas}(r)$, would also be self–similar, if no additional scale is introduced. Hence we have:

$$\rho_{gas}(r) = \rho_{gas}(0)y_{gas}(r/r_s) \tag{2.10}$$

The different parameterization in eq. 2.3 and 2.10 is due to the fact that, in contrast to DM density profile, a flat gas core near the center of the halo is well observed, and is expected if the gas temperature is not a strong function of radius.

Our goal is to find an analytical expression for $y_{gas}(r/r_s)$ that satisfies the self–similarity requirement. Makino et al. (1998) and Suto et al. (1998) showed that this is possible assuming hydrostatic equilibrium between the gas pressure and the self–similar DM potential. In the original paper of Makino et al. this computation was done assuming that the gas distribution was isothermal. However, X-ray observations of clusters (Markevitch et al. (1998), De Grandi & Molendi (2002), Vikhlinin et al. (2005)) show that the temperature profiles of clusters are not isothermal and can be approximately described by a polytrope at least outside the regions of the cool core.

To take into account phenomenologically the effect of the gas temperature gradient which is found both in observations and in hydrodynamical simulations, Suto et al. (1998) parameterized the gas pressure in a polytropic form $P_{gas} \propto \rho_{gas}T_{gas} \propto \rho_{gas}^{\gamma}$. γ is the so called "effective polytropic index" of the gas. Please note that this is not the polytropic index of the gas, that in our case in 5/3, as for an ideal gas. This parameterization gives a self-similar temperature profile,

$$T_{gas}(r/r_s) = T_{gas}(0)y_{gas}^{\gamma-1}(r/r_s) \tag{2.11}$$

Then the hydrostatic equilibrium equation,

$$\rho_{gas}^{-1}\frac{dP_{gas}}{dr} = -G\frac{M(\leq r)}{r^2} \tag{2.12}$$

gives the differential equation for the gas profile $y_{gas}(x)$,

$$\frac{dy_{gas}^{-1}(r/r_s)}{dr} = -\left(\frac{\gamma-1}{\gamma}\right)\frac{G\mu m_p M_{200}}{k_B T_{gas}(0)r^2}\left(\frac{m(r/r_s)}{m(c)}\right) \tag{2.13}$$

Here μ is the mean molecular weigh, m_p is the proton mass, k_B is the Boltzmann constant, and $m(x)$ is the dimensionless mass profile given by equation 2.6.

Since $y_{gas}(0) = 1$ (see equation 2.10) equation 2.13 is formally solved as (Suto et al. (1998)):

$$y_{gas}^{\gamma-1} = 1 - 3\eta^{-1}(0)\left(\frac{\gamma-1}{\gamma}\right)\left(\frac{c}{m(c)}\right)\int_0^x du\frac{m(u)}{u^2} \tag{2.14}$$

where

$$\eta^{-1}(x) = \frac{T_{vir}}{T_{gas}(x)} = \frac{G\mu m_p M_{200}}{3r_{200}k_B T_{gas}(x)} \tag{2.15}$$
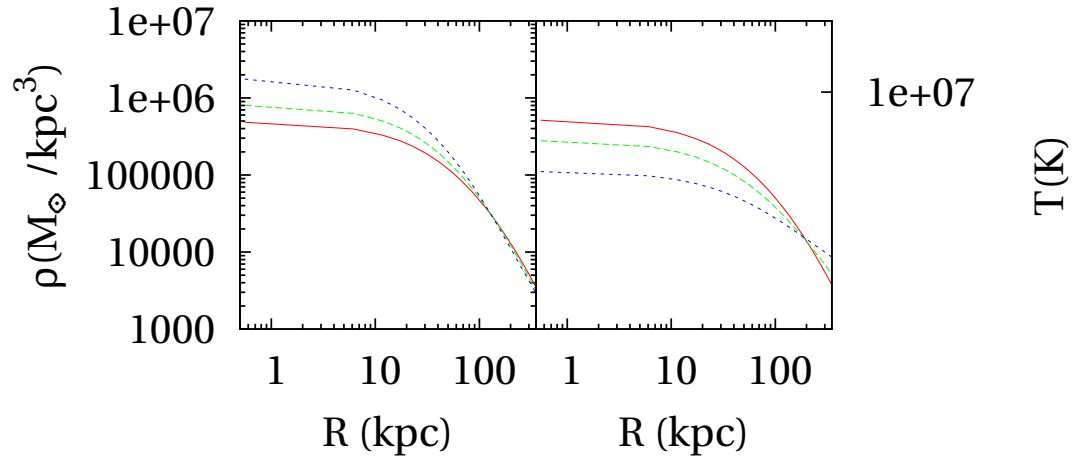
Figure 2.2: The gas density profile (*left*) and the gas temperature profile (*right*) for different effective polytropic indexes γ. In particular red line is for $\gamma = 1.25$, green line for $\gamma = 1.18$ and blue line for $\gamma = 1.10$. The analytical expressions for the two profiles are the one reported respectively in eq. 2.17 and 2.19.

is the normalization factor which relates T_{gas} to M_{vir}.

Now, the integral in equation 2.14 is easily evaluated using for $m(u)$ the expression given in equation 2.9 :

$$\int_0^x du \frac{m(u)}{u^2} = 1 - \frac{\ln(1+x)}{x} \tag{2.16}$$

We are ready to give now an explicit expression for the gas temperature, density and pressure profile as calculated from hydrostatic equilibrium:

$$\rho_g(r) = \rho_{g0} \left(1 - a \left(1 - \frac{\ln(1+cx)}{cx} \right) \right)^{1/(\gamma-1)} \tag{2.17}$$

$$P_g(r) = P_{g0} \left(1 - a \left(1 - \frac{\ln(1+cx)}{cx} \right) \right)^{\gamma/(\gamma-1)} \tag{2.18}$$

$$T_g(r) = T_{g0} \left(1 - a \left(1 - \frac{\ln(1+cx)}{cx} \right) \right) \tag{2.19}$$

where:

$$a = \frac{\gamma - 1}{\gamma} \frac{3}{\eta_0} \frac{c(1+c)}{(1+c)\ln(1+c) - c} \tag{2.20}$$

and η_0 is the extrapolation of $\eta(r)$ at $r = 0$. The gas profiles we have obtained have basically two free parameters: the effective polytropic index γ and the normalization

factor $\eta(0)$. In figure 2.2 we plot the density and temperature profile of the gas, as defined in equations 2.17 and 2.19, for different effective polytropic index. In the next section we will show under which hypothesis it is possible to determine these two parameters.

2.3 Gas and DM outside the core

In this section we will show how it is possible to link the gas and the DM density profile in order to fix the free parameters γ and $\eta(0)$. Many hydrodynamical simulations have observed the gas density profile tracing the DM profile outside the core, $r \geq r_{200}/2$ (Navarro et al. (1995), Bryan & Norman (1998), Eke et al. (1998)...). From an analytical point of view we can require the gas density profile, $y_{gas}(x)$, to match the DM density profile, $y_{DM}(x)$, at a certain matching point x_m. This means requiring the slopes of the two profiles to be the same at x_m:

$$s_m = \left.\frac{d \ln y_{dm}(x)}{d \ln x}\right|_{x=x_m} = \left.\frac{d \ln y_{gas}(x)}{d \ln x}\right|_{x=x_m} \tag{2.21}$$

where s_m is an effective slope of the DM density profile at x_m. Using equation 2.3 we have:

$$s_m = -\frac{1}{1+x_m}(1+3x_m) \tag{2.22}$$

Using the expression derived for y_{gas} (equation 2.14) in eq. 2.21 we obtain a solution for the mass–temperature normalization factor at the center $\eta(0)$:

$$\left.\frac{d \ln y_{gas}(x)}{d \ln x}\right|_{x=x_m} = s_m \tag{2.23}$$

$$\frac{x_m}{\gamma-1}\left[1 - \frac{3}{\eta(0)}\frac{\gamma-1}{\gamma}\frac{c}{m(c)}\int_0^{x_m} du\,\frac{m(u)}{u^2}\right]^{-1}\left[\frac{-3}{\eta(0)}\frac{\gamma-1}{\gamma}\frac{c}{m(c)}\frac{m(x_m)}{x_m^2}\right] = s_m \tag{2.24}$$

$$\eta(0) = \frac{1}{\gamma}\left[\left(\frac{-3}{s_m}\right)\frac{c\cdot m(x_m)}{x_m\cdot m(c)} + 3(\gamma-1)\frac{c}{m(c)}\int_0^{x_m} du\,\frac{m(u)}{u^2}\right] \tag{2.25}$$

We have obtained this expression requiring the DM and gas density profiles to have the same slope at r_m. According to the simulation the two slopes should agree not only at $x = x_m$ but also everywhere in the outer region of halos, so within a factor 2 above and below r_{200} ($c/2 < x < 2c$). This requirement will not be satisfied in general; however we still have one free parameter left, the effective polytropic index γ. We fix it by requiring that the solution for $\eta(0)$ does not depend on x_m. The idea is to calculate the gas temperature at an arbitrary radial point using the solution for $\eta(0)$ given above and look for the values of γ that satisfy the requirement that $\eta(0)$ is independent of x_m (see for details Komatsu & Seljak (2001)). The range found is $\gamma = 1.1 - 1.2$. Our model then no longer contains any free parameters.

Chapter 3

Cooling in DM halos: physics

In the previous chapters we have mentioned gas cooling as the process causing "loss of energy due to radiative emission" without any further considerations. In this chapter we want to discuss more in detail this statement. From a physical point of view the gas in the DM halos can be considered as an optically thin plasma. The composition of this plasma is in general very complex: in fact in real case the gas is metal enriched and therefore the plasma is composed not only by electrons and protons (as in the case of hydrogen plasma) but also by a number of different ions. In principle, if we are interested in the computation of radiative losses of this plasma, we have to take into account all the different atomic processes that can take place within it. In order to do that, we have to know the exact composition of the plasma (for example what is the ionization fraction for each species), which is a function of the temperature (at high temperature the gas will be fully ionized while at lower temperature it will be present some ions). Giving a detailed treatment of all the possible atomic processes that take place in a plasma, is quite complex and out of the scope of this thesis. We will concentrate on the most important processes using also several approximations to simplify the discussion. We will show in the last sections of this chapter how it is possible to collect together all the information coming from atomic processes to calculate a so–called "cooling function" for the plasma. The most general expression for the cooling function is:

$$\Lambda(T, A) = \Lambda_{lines} + \Lambda_{cont} \pm \Lambda_{rec} - \Lambda_{photo} + \Lambda_{coll} \pm \Lambda_{Compton} \qquad (3.1)$$

where T is the plasma temperature, A is the plasma composition, Λ_{lines} is the collisional line radiation term, Λ_{cont} takes into account the free-free and two photons continuum, Λ_{rec} is the contribution due to recombination processes, Λ_{photo} is the contribution from photoionization heating, Λ_{coll} arises from the collisional ionization and $\Lambda_{Compton}$ takes into account Compton heating/cooling. In order to simplify the situation we can assume *Collisional Ionization Equilibrium* (CIE thereafter). This means that the system is optically thin, low–density, dust–free and in steady state or quasi–steady state. Under these conditions the effects of any radiation field can be ignored, density effects are insignificant, three-body collisions are unimportant, and the ionization balance of the gas is time-independent. Moreover electron collisional ionization processes are balanced precisely by recombination processes (we

will discuss later this statemet). In this approximation there are three important conditions that specify the thermodynamic state of the free electrons, ions and photons in the plasma:

1. Photons are assumed to be free and do not interact with either electrons or the ions after they are emitted. Consequently photo–ionization processes (ionizing atoms by photons) and photo–excitation processes (raising an electron bound to atom to an excited level) are far less frequent than electron collisional ionization and excitation processes;

2. The atoms can be treated as if their electrons are all in their ground state rather than having a Boltzmann distribution as is common in local thermo-dynamic equilibrium gases;

3. The plasma is locally relaxed to a Maxwellian distribution around a common electron temperature, T; the free electrons and ions are assumed to have a common temperature.

In this case the only significant processes that must be taken into account are line radiation (bound–bound transition), recombination heating (bound–free transition) and continuum radiation (free-free transition). The cooling function calculated in CIE approximation is the one used in all the calculation we have done during this Thesis work. In the following sections we will give a short description of these processes.

3.1 Bound-Bound transitions

One of the most common process that take place in a plasma is the emission or the absorption of a photon due to transition of an electron from a bound state to another bound state. The outcome of this phenomenon are the spectral lines that allow to have important informations about the physical properties of the medium. Moreover, if the continuum is not very strong, emission lines can dominate the radiative transfer (e.g. $T \leq 0.5 keV$). The emission due to a transition for a bound state m to a bound state n (where in CIE approximation m is the ground state) can be described by the Einstein coefficient A_{mn}. The emitted power per unit volume is:

$$\frac{dW}{dV} = N_m h\nu_{mn} A_{mn} \tag{3.2}$$

where N_m is the number density of atoms at level m. In order to demonstrate how it is possible to evaluate A_{mn} without complicated calculations, we will use in the following a semi–classical approach instead of the correct quantistic approach. During the transition we can assume that the electron behaves as an harmonic oscillator with frequency ν_{mn}.

In the semi–classical approximation, for an harmonic oscillator, the electron dipole moment reads as:

$$d(t) = ex(t) = ex_0 \cos(2\pi\nu_{mn}t) \tag{3.3}$$

The emitted power can be calculated with the Larmor formula:

$$W = \frac{2q^2 \langle |\ddot{d}(t)|^2 \rangle}{3c^3} \tag{3.4}$$

where q denotes a generic charge and $\langle \rangle$ a time–average. We can now calculate the power emission for each oscillator:

$$W_{osc} = \frac{64\pi^4 \nu_{mn}^4}{3c^3} \left(\frac{ex_0}{2} \right)^2 \tag{3.5}$$

Moreover it is:

$$\frac{dW}{dV} = W_{osc} \cdot N_m \tag{3.6}$$

Then from equations 3.2 and 3.6 we get:

$$A_{mn} = \frac{64\pi^4 \nu_{mn}^3}{3hc^3} \left(\frac{ex_0}{2} \right)^2 \tag{3.7}$$

where x_0 is the classical radius of the electron in the ground state.

The quantistic calculation gives an analogous expression:

$$A_{mn} = \frac{64\pi^4 \nu_{mn}^3}{3hc^3} \left(\frac{ex_0}{2} \right)^2 |\mu_{mn}|^2 \tag{3.8}$$

where μ_{mn} is the so–called "electric dipole matrix":

$$\mu_{mn}^2 = e^2 < \psi_n |r| \psi_m > \tag{3.9}$$

and $\psi_{n,m}$ are the wave functions of the two atomic states.

The emission changes the kinetic energy of the harmonic oscillator:

$$E(t) = \frac{m_e \dot{x}^2}{2} = 2\pi^2 m_e \nu_{mn}^2 x_0^2 \cos^2(2\pi \nu_{mn} t) \tag{3.10}$$

Since :

$$\ddot{d}(t) = \frac{8\pi^2 \nu_{mn} e^2}{m_e} E^2(t) \tag{3.11}$$

using the Larmor formula:

$$\frac{dE}{dt} = -W_{osc} = -\frac{8\pi^2 e^2 \nu_{mn}^2}{3m_e c^3} E(t) \tag{3.12}$$

we have, by definition :

$$A_{mn} = -\frac{8\pi^2 e^2 \nu_{mn}^2}{3m_e c^3} \tag{3.13}$$

The quantistic calculations gives:

$$A_{mn} = -\frac{8\pi^2 e^2 \nu_{mn}^2}{m_e c^3} f_{mn} \tag{3.14}$$

where f_{mn} is the so–called "oscillator strength" and takes into account the effective number of electrons per atom. It is possible to calculate this value using quantum mechanics. In order to calculate now the number density of atoms at level m, N_m, we can use the statistical equilibrium equation:

$$\sum_{l<m} N_e N_l C_{lm} + \sum_{i>m} A_{im} N_i = N_m \sum_{l<m} A_{ml} \tag{3.15}$$

where N_e is the electron density and C_{lm} is the collisional excitation coefficient of the transition $l \rightarrow m$. Under the CIE approximation (low density limit) the population of an excited level is very small compared with that of the ground level, so that the second term is negligible and allow us to write:

$$W_{mn} = N_g N_e C_{gm} B_{mn} h\nu \tag{3.16}$$

where C_{gm} is the collisional excitation coefficient from the ground state to the upper level m,

$$B_{mn} = \frac{A_{mn}}{\sum_{l<m} A_{ml}} \tag{3.17}$$

is the radiative branching ratio, and N_g is the ground state density of the ion species Z. The collisional excitation coefficient are obtained by integrating the cross section over a Maxwellian distribution (see Kato (1976)). With some calculations one can derive the following expression:

$$W_{mn} = 8.63 \cdot 10^{-6} N_g N_e h\nu \frac{\exp(h\nu/kT)}{T^{1/2}} \frac{8\pi}{\sqrt{3}} f_{mn} g \tag{3.18}$$

where g is the so–called "Gaunt factor" that corrects for quantum mechanical effects and for the effect of distant collisions.

3.2 Bound-Free transition

We define "bound-free" or "free-bound" transitions all the transitions in which a bound state is formed (*recombination*) from a free configuration, or when a free state is formed (*ionization*) from a bound situation. For a schematic picture of the possible phenomena see fig. 3.1.

In the absence of strong UV fluxes that give radiative ionization, impact ionization is the dominant mechanism for plasma production. We will discuss now in a quantitative way collisional recombination and photoionization for Hydrogen atom. In this case recombination is basically electron–proton collision and can be expressed as:

$$e + H^+ \rightarrow H^0 + h\nu \tag{3.19}$$
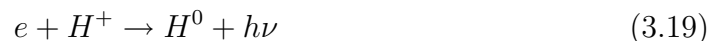
Once we have assumed CIE, we are able to ignore photo–ionization, due to the assumption that the photons do not interact with electrons after they are created and three–body recombination, due to the assumption that the plasma is low–density.
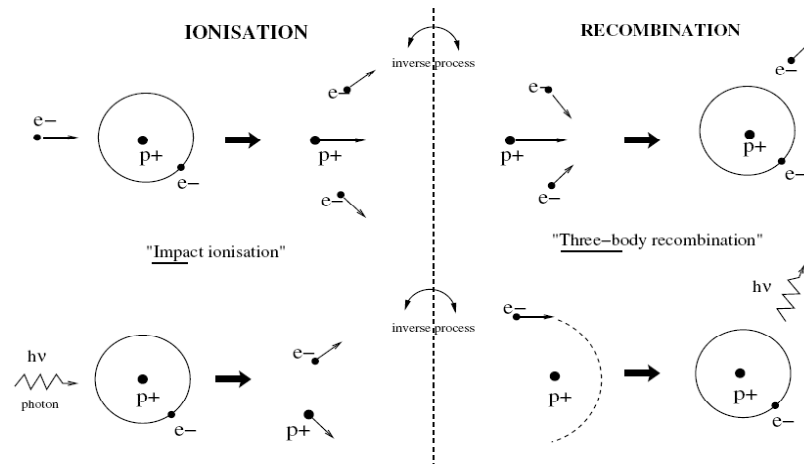
Figure 3.1: Main ionization and recombination processes (from lecture of prof. A.Fasoli, EPFL, 2006/2007)).

3.2.1   Collisional ionization equilibrium

As we have already said, in the absence of any significant radiation field the ionization balance can be calculated using only the recombination and collisional ionization. We will now discuss in a quantitative way collisional recombination and photoionization for an Hydrogen atom. The argument can be generalized for a plasma in which there are other elements.

The probability per time unit that an H^+ is involved in 3.19 is:

$$P_{21} = n_e \sigma_r(v) v \tag{3.20}$$

where v is the electron's velocity. When we integrate over a thermal distribution, we get:

$$P_{21} = n_e \alpha \tag{3.21}$$

where α is the *recombination coefficient*, which is a function of temperature. The reverse reaction of reaction 3.19 is the photoionization of the atom. In local thermodynamical equilibrium (LTE hereafter), the rates of two processes must be equal by the principle of detailed balance. This means that one can derive the recombination rate α if the photoionization cross section is known. The details of this derivation are in Rybicki & Lightman (1986). The derivation involves the following important points: first of all we set up the equation of *statistical equilibrium* between the two states (neutral and ionized). According to detailed balance, the total recombination rate equals the total ionization rate, where these total rates include spontaneous transitions and induced transition:

$$R(v \rightarrow v + dv) = (1 - e^{-h\nu/k_B T}) I(\nu \rightarrow \nu + d\nu) \tag{3.22}$$

where (R, I) are the recombination and photoionization rates, respectively. In terms of collisional cross section, photoionization cross section, and photon number density

expressed in terms of the black–body spectrum $B_\nu(T)$ we have:

$$n_e n_{H^0} \sigma_r(v) v f(v) dv = (1 - e^{-h\nu/k_B T}) n_{H^+} \left(\frac{4\pi B_\nu(T)}{h\nu} \right) \sigma_{ph}(\nu) d\nu \qquad (3.23)$$

where σ_{ph} is the photoionization cross section. In recombination, energy conservation means that the kinetic energy of the incoming electron is equal to the sum of the ionization energy and the energy $(h\nu_{ie})$ of the emitted photons:

$$\frac{m_e v^2}{2} = h\nu_{ie} + h\nu \qquad (3.24)$$

Next, assuming a Maxwellian distribution for the electrons, we write the equation of *thermodynamical equilibrium* between the two states (neutral and ionized). This is the Saha equation:

$$\frac{n_e n_{H^+}}{n_{H^0}} = \frac{2g_+}{g_0} \left(\frac{2\pi m_e k_B T}{h^2} \right)^{3/2} e^{-h\nu_{ie}/k_B T} \qquad (3.25)$$

where (g_+, g_0) are the statistical weights of the ionized and neutral state; recall that $g_0 = 2n^2$ (sum of l–levels in a given n, times two for the spin) and $g_+ = 1$ (it's a bare proton). Equations 3.23 and 3.25 involve the same quantities, so we can derive the desired relationship between the recombination and photoionization cross sections:

$$\sigma_r(v) = 2n^2 \left(\frac{h\nu}{m_e c v} \right)^2 \sigma_{ph}(\nu) = \frac{h\nu_{ie}}{me^2} \frac{h\nu_{ie}}{m_e v^2/2} \frac{\nu_{ie}}{\nu} \frac{\sigma_{ph}}{n^3} \qquad (3.26)$$

where σ_{ph} is the photoionization cross–section at the ionization threshold.

As we have performed this computation for hydrogen it is possible to compute collisional ionization equilibrium balance for the other elements of the plasma (see as example Sutherland & Dopita (1993)).

3.2.2 Recombination heating

Radiative recombination is the process by which an ion in a state i binds an electron from the electron sea to produce state $i-1$ with the subsequent radiation of photons. This process may be a heating or cooling effect, depending on the electron energy distribution that the recombining electrons are being removed from. As we saw in the previous section, the recombination cross sections are a strong function of energy and moreover they are largest near the threshold. If the energy distribution peak is higher than the threshold, then it is possible to demonstrate that cold electron will be preferentially removed from the electron sea. In this way the kinetic energy per remaining electron increases and the result is a net heating.

3.3 Free-free transition

When a high speed electron encounters the Coulomb field of another charge, it emits *bremsstrahlung* radiation, also known as free–free emission. The word bremsstrahlung means braking radiation because the electron rapidly decelerates when the other charge is a massive ion. As we have done for the bound–bound transition we will present the fundamental equations that permit to derive the bremsstrahlung emission. The derivation can be done classically using the dipole approximation for non–relativistic particle, with quantum correction added as "Gaunt factors" to the classical formulas.

Let's consider an electron moving with velocity $\bar{v}$ past an ion of charge Ze with impact parameter b. We will assume small–angle scattering so there is negligible deviation in the electron's trajectory from a straight line. The dipole moment is $\bar{d} = -e\bar{R}$, and its second derivative is:

$$\ddot{\bar{d}} = -e\dot{\bar{v}} \tag{3.27}$$

Taking the Fourier transform of this equation, we have the result:

$$-\omega^2 \bar{d}(\omega) = -\frac{e}{2\pi} \int_{-\infty}^{+\infty} \dot{v} e^{i\omega t} dt \tag{3.28}$$

By defining a *collision–time* as $\tau = b/v$ we can easily obtain:

$$\bar{d}(\omega) \begin{cases} \frac{e}{2\pi\omega^2}\Delta\bar{v} & \text{if } \omega\tau << 1 \\ 0 & \text{if } \omega\tau >> 1 \end{cases}$$

where $\Delta\bar{v}$ is the change of velocity during the collision. Since the path is almost linear, the change in velocity is predominantly normal to the path. Thus we integrate that component of the acceleration normal to the path:

$$\Delta v = \frac{Ze^2}{m} \int_{-\infty}^{+\infty} \frac{bdt}{(b^2 + v^2t^2)^{3/2}} = \frac{2Ze^2}{mbv} \tag{3.29}$$

In the dipole approximation the emission is:

$$\frac{dW}{d\omega} = \frac{8\pi\omega^4}{3c^3}|\bar{d}(\omega)|^2 \tag{3.30}$$

Thus the emission for a single collision is:

$$\frac{dW(b)}{d\omega} = \begin{cases} \frac{8Z^2e^6}{3\pi c^3 m^2 v^2 b^2} & \text{if } b \ll v/\omega \\ 0 & \text{if } b \gg v/\omega \end{cases}$$

This is the spectrum for small–angle scattering by a single electron off a single ion. Next we want to generalize this to the case of a realistic plasma in which we have many electrons interacting with many ions. Let the ion and electron number density in the plasma be n_i and n_e. Then the flux of electrons incident on an ion is $n_e v$ for

a fixed electron speed v. The element of area about an ion over which an electron encounter occurs is $2\pi b db$. So the emission per unit time, per unit volume, per unit frequency range is:

$$\frac{dW}{d\omega dV dt} = n_e n_i 2\pi v \int_{b_{min}}^{b_{max}} \frac{dW(b)}{d\omega} b db \qquad (3.31)$$

where b_{min} is a minimum impact parameter to be chosen and $b_{max} \sim v/\omega$ is some value beyond which the $b << v/\omega$ limit no longer applies and the contribution to the integral becomes negligible. It is:

$$\frac{dW}{d\omega dV dt} = \frac{16 e^6 n_e n_i Z^2}{3 c^3 m_e^2 v} \ln\left(\frac{b_{max}}{b_{min}}\right) \qquad (3.32)$$

The exact expression for the radiation spectrum can be obtained with a full quantum treatment. For convenience, a quantum correction is added to the classical formula. This correction term is known as the *Gaunt factor*:

$$g_{ff}(v, \omega) = \frac{\sqrt{3}}{\pi} \ln\left(\frac{b_{max}}{b_{min}}\right) \qquad (3.33)$$

giving:

$$\frac{dW}{d\omega dV dt} = \frac{16 \pi e^6 n_e n_i Z^2}{3^{3/2} c^3 m_e^2 v} g_{ff} \qquad (3.34)$$

This is now the bremsstrahlung radiation emitted per unit time per unit volume per unit frequency by single–speed electrons interacting with many ions. Next we compute the volume emissivity for a thermal distribution of electron speeds.

In a thermal plasma, the velocity distribution of the electrons (and ions) is Maxwellian. This distribution is isotropic and therefore the number of thermal particles with velocity $\bar{v}$ in the range $d^3 v$ is:

$$f(\bar{v}) d^3 v = f(v) 4\pi v^2 dv \propto \exp\left(-\frac{mv^2}{2 k_B T}\right) v^2 dv \qquad (3.35)$$

We need to average our single–speed radiation spectrum over this distribution function for all electron speeds satisfying $\frac{1}{2} m_e v^2 \geq h\omega/2\pi$. i.e.

$$\frac{dW(T, \omega)}{d\omega dV dt} = \frac{\int_{v_{min}}^{\infty} \frac{dW(v, \omega)}{d\omega dV dt} v^2 \exp(-\frac{mv^2}{2 k_B T})}{\int_0^{\infty} v^2 \exp(-\frac{mv^2}{2 k_B T})} \qquad (3.36)$$

Using $d\omega = 2\pi d\nu$, the final result is the expression for the free-free volume emissivity:

$$j_\nu^{ff} = \frac{dW}{dV dt d\nu} = \frac{32 \pi e^6}{3 m_e^{3/2} c^3} \left(\frac{2\pi}{3 k_B T}\right)^{1/2} Z^2 n_e n_i \exp\left(-\frac{h\nu}{k_B T}\right) \bar{g_{ff}} \qquad (3.37)$$

where $\bar{g_{ff}}$ is the velocity averaged Gaunt factor. Its value is typically of order unity.

3.4 Sutherland & Dopita Cooling function

We are now ready to discuss how it is possible to calculate the so–called "cooling function" using the informations we got from the previous section. We will follow Sutherland & Dopita (1993). They calculated cooling function for a plasma under equilibrium and non equilibrium conditions, over a range of $10^4 - 10^{8.5} K$ and for a range of abundances. So far the so–called "Sutherland & Dopita cooling function" is the most used in literature, due to the large amount of atomic processes implemented and due to large range covered in temperature and abundances. Of course it is not possible to do analytically the computation of the amount of energy lost by the plasma due to the different processes. They used a code, called *MAPPING II*, in which they take in account the behavior of 16 atoms (H, He, C, N, O, Ne, Na, Mg, Al, Si, S, Cl, Ar, Ca, Fe, Ni) and all stages of ionization. The main point is the calculation of ionization balance of the plasma which in general is determined by its temperature, ionization history and the atomic processes operating in the plasma (that we have described in the previous sections). Of course the computation must be done for all the 16 atoms. The computational details are reported in the paper of Sutherland & Dopita (1993). In figure 3.2 the contribution to the cooling function due to different atomic processes is shown in details.

Then, for each temperature, it is possible to calculate the contribution to the global cooling function due to the different processes (see eq. 3.1). In figure 3.3 it is shown the cooling function calculated for a primordial–composition gas. At high temperature the dominant mechanism is the free-free bremsstrahlung ($\log(T) > 6.5$), while at lower temperature the dominant process is the emission due to Helium and Hydrogen. The same behavior is shown for non–zero metallicity cooling function. We denote the cooling function calculated in this way as Λ_{net}. It is useful to define sometimes a "normalized cooling rate" as:

$$\Lambda_N = \frac{\Lambda_{net}}{n_i n_e} \tag{3.38}$$

3.5 Cooling time scale

In this last section of the chapter we will see how it is possible to define a "cooling time scale" for the gas that will be a crucial quantity in following of the thesis.

For an ideal gas, the pressure is:

$$P = \frac{N k_B T}{V} \tag{3.39}$$

and the internal thermal energy

$$U = \frac{3}{2} N k_B T \tag{3.40}$$

where T is the gas temperature, V is the total volume, N is the total number of particles in the system and k_B is the Boltzmann constant. Now, if we make
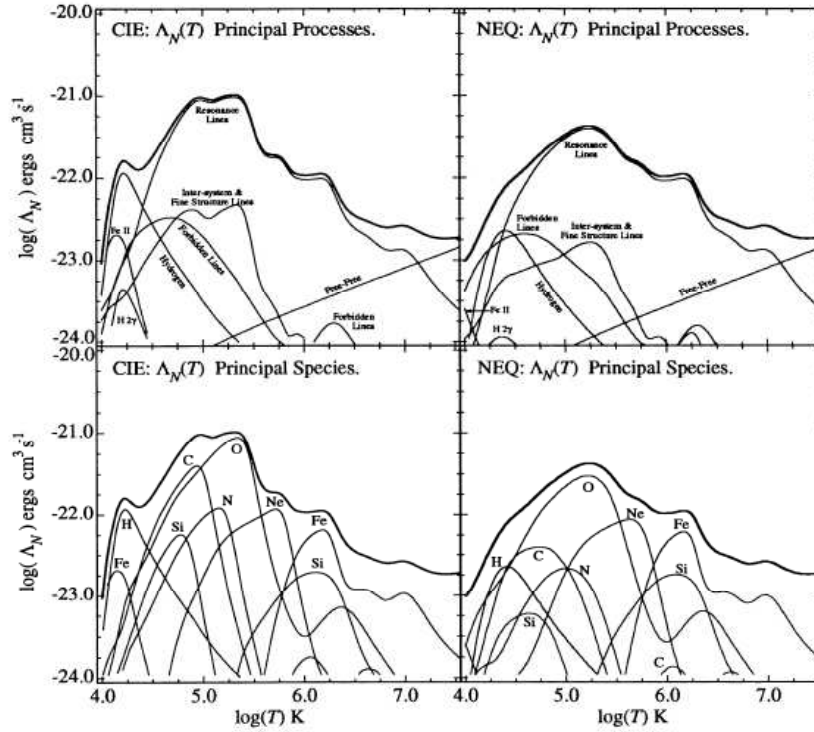
Figure 3.2: Cooling function contribution. The upper panels show the contribution to the cooling function by the different atomic processes in the case of Collisional Ionitation Equilibrium (CIE) and in the case of Non Equilibrium (NEQ). The lower panels show, for the same two cases, the emission by species, selecting only the dominant species for clarity. (Sutherland & Dopita, 1993)
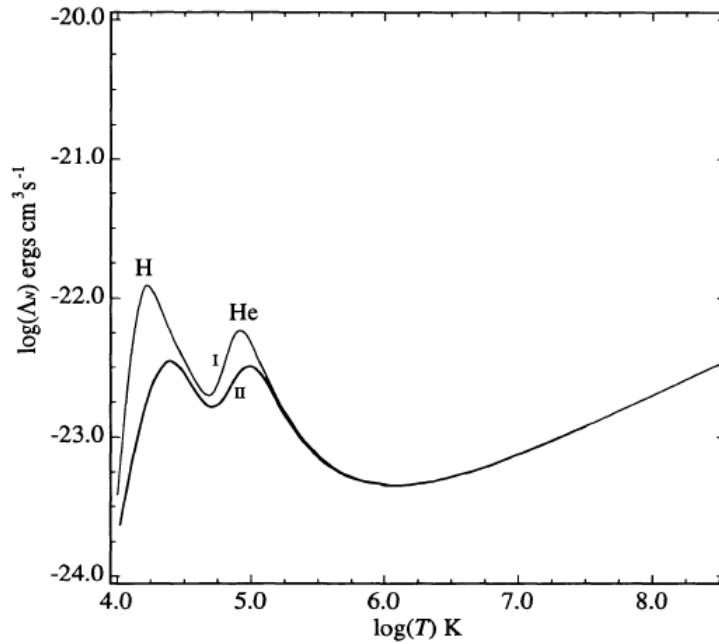
Figure 3.3: Primordial cooling function (zero metallicity) for CIE and NEQ cases. In both models the free-free cooling dominates down to below log(T) = 6.5. The upper curve (I) is the CIE model, the lower (II) represents the NEQ case. The two peaks are due to the Hydrogen and Helium emission (Sutherland & Dopita (1993).

the hypothesis that the gas pressure is constant, according to the first principle of thermodynamic the amount of heat lost by the thermal electrons is:

$$dQ = dU + PdV = \frac{3}{2}(Nk_BdT + k_BTdN) \tag{3.41}$$

For pure radiative cooling, with no heating, we have:

$$dQ = -n_e n_H \Lambda_N(T, x_i, Z)V dt \tag{3.42}$$

where $\Lambda_N(T, x_i, Z)$ is the normalized cooling rate which depends on the gas temperature, the ionization state, and the total abundances of the heavy elements specified by the metallicity Z.

We can define the *time scale of the cooling* as :

$$t_{cool} := \left| \frac{d \ln T_{gas}}{dt} \right|^{-1} \tag{3.43}$$

From equations 3.41 and 3.42 we get:

$$t_{cool} := \left| \frac{1}{T} \frac{1}{Nk_B} \left[-\frac{2}{3} n_e n_H \Lambda_N V - k_B T \frac{dN}{dt} \right] \right|^{-1} \tag{3.44}$$

The term dN/dt reflects the relative change in the total number of particles in the system. At temperature higher than 10^4 where hydrogen and helium remain

ionized, the number of particles remains approximately constant and this term can be neglected. Thus:

$$t_{cool} = \frac{3k_B T n}{2 n_e n_H \Lambda_N} \tag{3.45}$$

where we have defined $n = N/V = n_e + n_H$, the total particle number density. Since $n_e \sim n_H$, $n_e \cdot n_H \sim n_H^2$ and $n_e + n_H \sim 2n_H$ we have:

$$t_{cool} = \frac{3k_B T}{2n} \frac{4}{\Lambda_N} \tag{3.46}$$

Now, being $n = \rho/\mu_{hot} m_p$, the gas density and defining :

$$\Lambda_{cool} = \Lambda_N/4 \tag{3.47}$$

we can finally re-write equation 3.44 as:

$$t_{cool} := \frac{3k_B T \mu_{hot} m_p}{2\rho \Lambda_{cool}} \tag{3.48}$$

where μ_{hot} is the mean molecular weight and all the quantities are referred to the hot gas. In the following for our computations we will use the cooling function Λ_N tabulated by Sutherland and Dopita (2003). Then we will have Λ_{cool} through eq. 3.47.

Chapter 4

Modeling cooling in SAMs

As we have already stressed in the first chapter, the central process of galaxy forma-
tion is cooling, because it sets the rate at which the raw material becomes available
to star formation (Blumenthal et al. (1984)). Therefore one of the crucial points in
SAMs is its description. In the following we will present two different recipes for
cooling implemented in the SAMs currently present in literature. The first one, that
we called "Classical cooling model", was proposed for the first time by White &
Frenk (1991) and is implemented in most of SAMs, while the second one, referred
to as "MORGANA cooling model", was proposed more recently by Monaco et al.
(2007).

4.1   The classical cooling model

The "Classical cooling model" (CM thereafter) for the gas cooling inside DM halos
was set out in details by White & Frenk (1991). They based their framework on the
arguments about gas cooling set in Rees & Ostriker (1977). The gas initially has
the same spatial distribution as the DM. As fluctuations in the DM separate from
the Hubble expansion, turn around and collapse, the gas is assumed to be heated
by shocks as it falls into the gravitational potential well of the DM halo, producing
a hot gas halo that is supported against further collapse by the pressure of the gas.
The gas attains the virial temperature of the halo, which depends upon the mass
of the halo:

$$T_{vir} = \frac{\mu m_p}{3k_B} V_c^2 \qquad (4.1)$$

where V_c is the circular velocity of the halo:

$$V_c = \sqrt{\frac{GM_{vir}}{r_{vir}}} \qquad (4.2)$$

The crucial point is now to define a "cooling rate", i.e. how fast the gas cools
down. Of course the cooling rate depends on the cooling time that, as we saw in
the last chapter, depends on the inverse of the gas density, and to a less extent
on the gas temperature. In particular the dependence on the temperature is given

by the cooling function. If the gas is very hot ($log(T) > 6.5$) the cooling function is dominated by bremsstrahlung emission (that scales as $T^{1/2}$) and therefore the cooling time depends on $T^{1/2}$. For the sake of completeness let us write again the expression for cooling time:

$$t_{cool}(r) := \left| \frac{d \ln T_{gas}(r)}{dt} \right|^{-1} = \frac{3 k_B T(r) \mu m_p}{2 \rho(r) \Lambda_{cool}(T(r))} \tag{4.3}$$

where $T(r)$ is the temperature profile of the gas, k_B is the Boltzmann constant, $\rho(r)$ is the gas density profile, μ is the mean molecular weight of the hot phase, m_p is the proton mass and Λ_{cool} is the cooling function as defined in equation 3.47. It is important to remember that this expression for cooling time is valid in the hypothesis of *isobaric cooling*. The crucial relevance of this hypothesis will be discuss later in more details. Now, starting from this definition of cooling time we can define a *cooling radius* as follow:

$$r_{cool,C}(t_\star) := \{ r | t_{cool} = t_\star \} \tag{4.4}$$

In words: the cooling radius at a certain time $t_\star$ is the radius at which the cooling time is equal $t_\star$. In cosmological context $t_\star$ could be identified as the time for which the halo has been cooling quasi-statically, i.e. $t_\star = R_{vir}/V_{vir}$ (Yoshida et al. (2002)), as the time passed from the halo's formation (Benson et al. (2001)), as the Hubble time (White & Frenk (1991)), as the time interval since last major merger (Somerville & Primack (1999)). We call the cooling radius calculated in this way as $r_{cool,C}$ where C denotes the fact that this is the cooling radius in the CM. To simplify the notation we will refer in the following to this radius simply as r_C.

The gas density and temperature profiles are well defined, once the hypothesis of hydrostatic equilibrium has been made and the pressure of gas has been parameterized in a polytropic form (see equations 2.17, 2.19). Assuming that these profiles do not change with time, it is possible to calculate the cooling radius (as defined in eq. 4.4) just inverting the function $t_{cool}(r)$. In figure 4.1 we plot the cooling time and the cooling radius for three halos with M_{200} respectively $M = 10^{12} M_\odot$ (red line), $M = 10^{13} M_\odot$ (green line) and $M = 10^{14} M_\odot$ (blue line) and effective polytropic index $\gamma = 1.18$.

The last step is the definition of a *cooling mass*:

$$M_{cool}(t) := \{ M(\leq r_C(t)) \} \tag{4.5}$$

In words: the cooled mass at a certain time $t_\star$ is the mass inside the cooling radius evaluated at $t_\star$. This means:

$$M_{cool}(t_\star) := 4\pi \int_0^{r_{C(t_\star)}} \rho(r) r^2 dr \tag{4.6}$$

We are now ready to define for the classical cooling model a *cooling rate*:

$$\dot{M}_{cool} := 4\pi \frac{dr_C}{dt} \frac{d}{dr_C} \int_0^{r_C} \rho(r) r^2 dr = 4\pi \rho(r_C) r_C^2 \frac{dr_C}{dt} \tag{4.7}$$
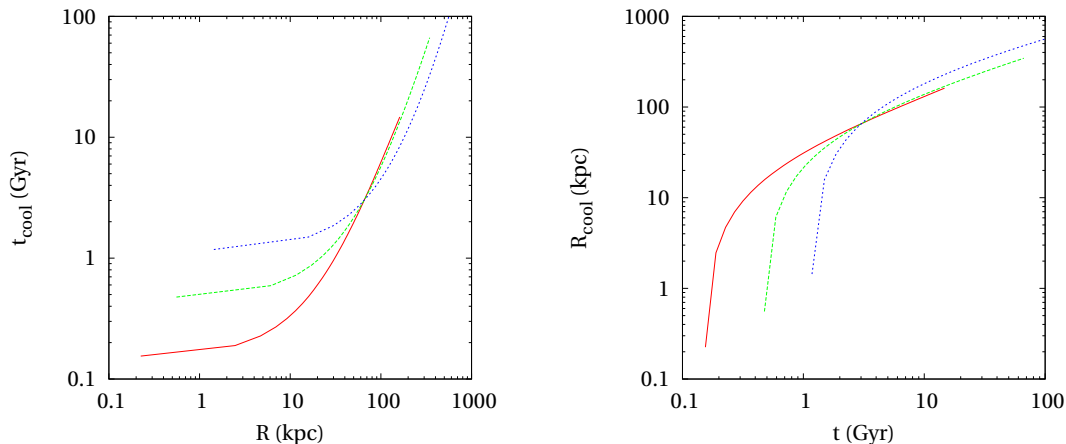
Figure 4.1: *Left*: Variation of cooling time with radius for three different masses: $M = 10^{12} M_\odot$ (red), $M = 10^{13} M_\odot$ (green) and $M = 10^{14} M_\odot$ (blue). The computation is done on initial temperature and density profile up to r_{200}. *Right*: Variation of cooling radius with time for the same masses. The curves are obtained inverting the ones plotted in the left pannel.

4.2 The Unclosed MORGANA cooling model

Let us describe another model. This model has been implemented in the paper by Monaco et al. (2007) and we will referred to it as the "Unclosed MORGANA cooling model" (MM thereafter). The starting point is the same: the definition of the cooling time (see equation 4.3). Then, instead of starting from the definition of a cooling radius, we define a "cooling rate of a shell" of gas of width Δr at a radius r in this way:

$$\Delta \dot{M}_{cool} = \frac{4\pi \rho(r) r^2 \Delta r}{t_{cool}(r)} \tag{4.8}$$

where the numerator represents the shell mass (of hot gas) and the denominator the cooling time. Assuming a NFW profile for DM component and hydrostatic equilibrium, we can calculate the cooling rate for all the gas mass by integrating equation 4.8. As before, the cooling time depends on density and temperature, but the density dependence is by far stronger, both intrinsically and because the temperature profile is much shallower than the density profile. For this reason, it is a good approximation to perform the integral in dr by assuming $T(r) \simeq T(r_{cool})$. We have:

$$\dot{M}_{cool} = \int_{r_{cool,M}}^{r_H} dr \frac{4\pi \rho(r) r^2}{t_{cool}(r)} \tag{4.9}$$

The lower limit for the integral $r_{cool,\mathrm{M}}$ is the cooling radius in the Unclosed MORGANA model (we will show here below how it is possible to calculate it). It is

important to note that the time dependence of the integral is through $r_{cool,M}$. In the following we will refer to it simply as r_M. As in the CM, the hot gas is assumed to lie in the region comprised between the cooling radius and r_{200}. Now, using the expression for $\rho(r)$ obtained before (see equation 2.17), equation 4.9 can be re-cast in the form:

$$\dot{M}_{cool} = \frac{4\pi r_s^3}{t_{cool}(0)}\rho(0) \int_{r_M/r_s}^{c_{NFW}} du\, u^2 \left[1 - a\left(1 - \frac{\ln(1+u)}{u}\right)\right]^{\frac{2}{\gamma-1}} \tag{4.10}$$

In this equation the cooling time at the center, $t_{cool}(0)$, is computed using the central density $\rho(0)$ and $T(r_M)$ for the temperature, as explained above. As in the CM we assume that the density profile does not change with time. Equation 4.10 is valid starting from the cooling time at $r = 0$, because nothing cools before that time. The rate of thermal energy loss by cooling is then computed as:

$$\dot{E}_{cool} = \frac{3kT(r_M)}{2\mu m_p}\frac{4\pi r_s^3\rho(0)}{t_{cool}(0)} \int_{r_M/r_s}^{c_{NFW}} du\, u^2 \left[1 - a\left(1 - \frac{\ln(1+u)}{u}\right)\right]^{\frac{2}{\gamma-1}} \tag{4.11}$$

We need then an equation that describes the evolution of the cooling radius. We can estimate it by assuming that the cold mass in a time interval dt is equal to the mass contained in a shell dr such that:

$$\frac{dr_M}{dt} = \frac{dM_{cool}}{dt}\frac{1}{4\pi\rho(r_M)r_M^2} \tag{4.12}$$

The evolution of the system is then followed by iterative numerical integration of equations 4.10, 4.11 and 4.12, starting after a time equal to the cooling time at $r = 0$. The integration is performed with a simple Runge–Kutta integrator (see Monaco et al. (2007) for all details) and the profile of the hot gas is re–computed at each time step. Clearly, as long as the mass and the thermal energy of each cold shell is removed from the profile, the rest of the gas is left unperturbed, so its profile does not change in time (as in CM). The situation is clarified in figure 4.2. Here we plot the initial density profile (black line) and the region (colored in red) where cold gas is present. In the following we will refer to this region as the "cooling hole". We would like to stress that the density profile of the hot gas outside the cooling hole is left unperturbed with respect to the initial one.

Now, step by step, we first evaluate equation 4.9 and then equation 4.10 in an iterative way. At each integration time, we have in this way two predictions, one about the amount of cooled mass and one about the cooling radius.

Summing up, the two main assumptions at the base of the Unclosed MORGANA model are: (i) cooling proceeds through an equation (4.8) of the kind $\dot{M}_{cool} = M_{hot}/t_{cool}$, (ii) there is a sharp transition from the hot to the cold phase which guarantees a sharp border of the hot gas. While the validity of assumption (ii) is supported bu the results of the simulations (see chapter 7), assumption (i) requires some discussion. While being deterministic, equation 4.8 takes the form of a typical decaying law, where the phase transition from hot to cold is assigned a probabilistic
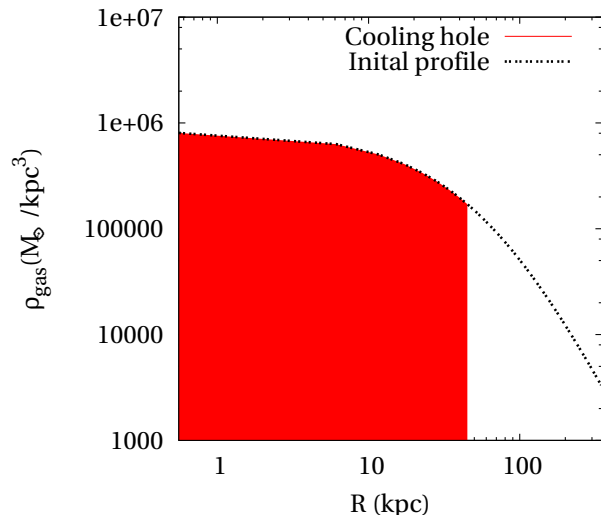
Figure 4.2: Theoretical gas density profile at $t = 0$ (*red line*), and at $t = 2t_{dyn}$ as truncated by the MORGANA model. The region before the truncation is the so–called "cooling hole".

time-scale t_{cool}. This may be seen at odds with the fact that cooling is described here as a deterministic process. Besides, particles in the simulated gas show values of their thermodynamical variables which scatter around their mean values (see chapter 6). We are convinced that this feature is one of the keys of success of this model; this point will be considered later.

4.3 Comparing the two models: a critical discussion

The aim of this section is to focus on the differences between the two cooling models, trying to underline the assumptions on which they are based. The main difference between the two models is the following: while CM attempts to provide a direct prediction of the cooling radius, which amounts to assuming that each shell cools exactly after one cooling time, MM computes the rate of mass and of energy loss by integrating the contribution of all mass shells. In doing so, it assumes that a sharp boundary between cold and hot gas phases is anyhow preserved and uses this to compute the evolution of the cooling radius.

Clearly, we expect that the predictions of the two models are different. Both models assumes that for $t < t_{cool}(0)$ it is $M_{cool} = 0$.

Let us consider the first integration time–step at time $t = t_{cool}(0)$. According to CM the cooling radius at this time is zero and consequently the cooled mass is zero. On the contrary, MM calculates the cooled mass by evaluating the integral in equation 4.9 from 0 to the r_{200}. In equation 4.9 each shell is weighted by its own cooling time. This means that the closer is the shell cooling time to the time at
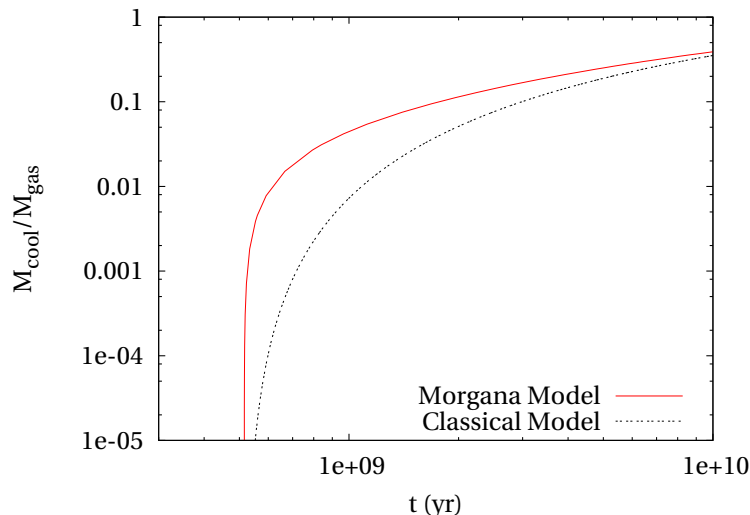
Figure 4.3: Evolution with time of the cooled mass fraction as predicted by the classical model and by the MORGANA model.

which the cooling radius (the lower limit of the integral) is calculated, the larger is the contribution from that shell to the cooled mass. Since the cooling time depends basically on the inverse of the density and due to the fact the density profile is almost flat for small radii, MM will predict more cool mass at the beginning (see figure 4.3). This fact implies, according to equation 4.12, that MM predicts a more rapid evolution of the cooling radius at the beginning (see figure 4.4). Consequently, in MM the cooling radius reaches quite soon the value at which the density profile becomes steeper and then after the initial fast increase of the cooled mass, M_{cool} will increase more gently, converging towards the value predicted by the CM at large times.

4.3.1 Interpretation of the cooling time

We have already shown in section 3.5 that the cooling time is obtained as $t_{\rm cool} = |d\ln T/dt|^{-1}$, where the dT is computed for an isobaric transformation. So the validity of the cooling time refers to the case of cooling at fixed pressure. In fact, the evolution of a parcel of gas undergoing cooling is more complicated than this, because density and temperature clearly evolve with time. We have verified, by numerically integrating the thermodynamical equations of a parcel of hot gas, that the time needed to cool from a relatively high temperature ($T \sim 10^6 - 10^8$ K) to 10^4 K is within a few per cent equal to the cooling time computed using the initial temperature and density, and this is true only in the simplest case in which pressure is constant. We can then say that the classical cooling model, which predicts that a shell of gas will be cooled after one cooling time (computed on the initial configuration), can give a good approximation as long as gas pressure remains roughly constant during the evolution.
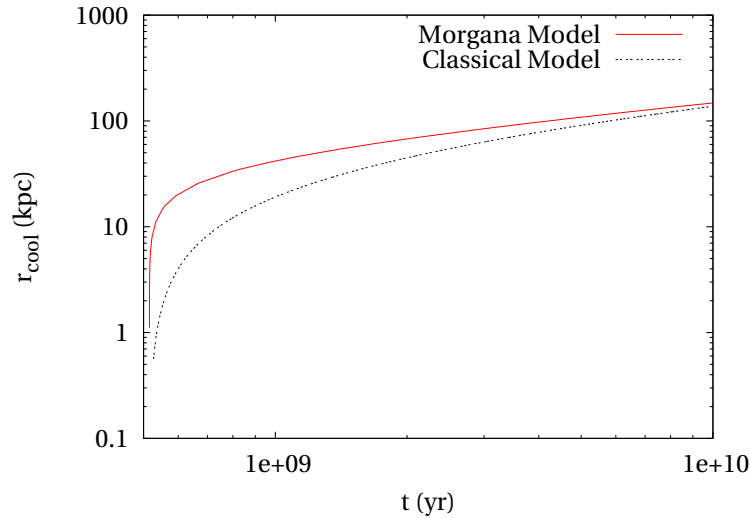
Figure 4.4: Evolution with time of the cooling radius as it is predicted by classical model and by MORGANA model.

4.4 The Closed MORGANA cooling model

In the previous sections we presented two different models in which cooling can be described and we focused on the hypothesis on which the two models are based on. In this section we will present a variation of the MORGANA model. Both the classical model and the MORGANA model assume that pressure is balanced at the cooling radius. The question is: Is this hypothesis realistic ? The answer in general is negative (we will come back on this point in chapter 7). In particular, as long as the time derivative of the cooling radius is much larger than the gas sound speed, the boundary of the cooled region propagates so quickly that any gas motion can be neglected. This holds only at very low $r_{\rm M}$. The late evolution of cooling is better represented by letting the "cooling hole" to close at the sound of speed. We then define a further cooling radius $r_{\rm M,ch}$, corresponding to a model where its evolution is given by the equations:

$$\frac{dr_{\rm M,ch}}{dt} = \frac{dr_{\rm M}}{dt} - c_s \qquad (4.13)$$

where :

$$c_s = \left(\frac{\partial p}{\partial \rho}\right)^{1/2} \qquad (4.14)$$

is the sound speed evaluated at the cooling radius. This simple change makes the predictions of the cooling model remarkably different, as the behavior of the cooling radius turns out to be remarkably different, so the mass is distributed over a different volume. We will refer to this Model as the "Closed MORGANA Model" (CMM thereafter). The implicit assumption here is that the gas has time to settle

into a new hydrostatic equilibrium configuration. Moving the cooling radius towards the center (see eq. 4.13) has the effect of tilting the density profiles that becomes steeper (higher in the inner regions and lower in the outer regions) as it is shown in figure 4.5. Obviously the hot mass is conserved (see figure 4.6). Increasing the density profile in the inner regions has the net effect of shortening the cooling time of the inner shells and consequently to increase the cooling mass. Eventually this leads to a catastrophic cooling of all the gas. A very simple and effective way to obtain an acceptable behavior is to suppress the sound speed term in equation 4.13 when the specific thermal energy of the hot gas becomes smaller than the specific virial energy ($-0.5U_H/M_H$, where U_H is the binding energy of DM halo).
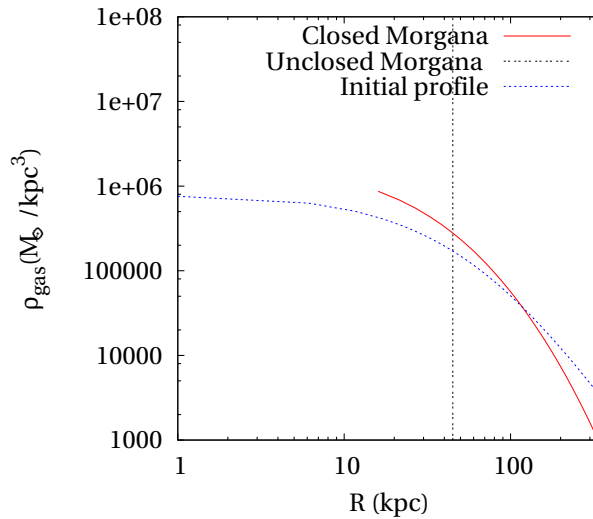

Figure 4.5: *Blue line*: Initial density profile of the gas. *Black line*: Cooling radius (eq.4.12), predicted by MM, at a time $t_\star$. The cooled mass is calculated at $t_\star$ performing the integration of the initial density profile from this radius to the r_{200}. *Red line*: Density profile calculated by CMM. The radius at which the profile is truncated is calculated using equation 4.13. In CMM at $t_\star$ the cooled mass is calculated performing the integration of this profile.

The closure of the cooling hole is easily implemented in the model, but corresponds to a rather drastic change in the interpretation of the cooling radius: while both the CM and MM try to predict, starting from the initial conditions, which part of the gas is going to cool, so that their predicted cooling radius should be interpreted as a Lagrangian quantity, the CMM attempts to follow the physical evolution of the system in a more detailed way. Its cooling radius $r_{M,ch}$ should then be interpreted as an Eulerian quantity.
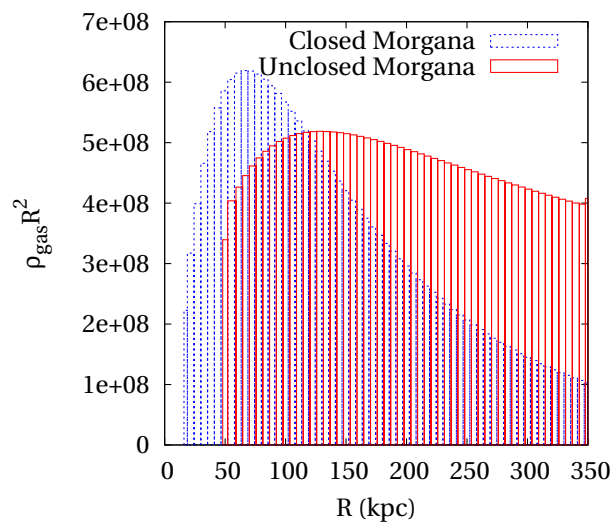
Figure 4.6: *Red line*: Hot gas mass as evaluated integrating the initial density profile up to the cooling radius at $t_\star$.*Blue line*: Hot gas mass calculated from the CMM density profile. The cooling radius is here evaluated at $t_\star$ using equation 4.13. The two masses are by definition the same.

Chapter 5

Numerical simulations

At the end of the XIX century the French mathematician Henri Poincaré demonstrated that it is not possible to predict (analytically) the evolution of a system composed by a number N of collisionless point masses that move under the influence of their mutual gravitational forces, if N is greater than 2. This means for example that it is not possible to calculate analytically the evolution of the system Earth-Moon-Sun and even more so it is not possible to solve a lot of physicals problems without extra-hypothesis such as high symmetry or an approximated treatment of inherently non linear problems. The rapid growth of computer performance and the implementation of more sophisticated algorithms allow, since the seventies, to face N-Body problems from a numerical point of view without the need to do approximations. The first "numerical simulations" (Holmberg (1941), Peebles (1970), Press & Schechter (1974); White (1976)...) largely employed the direct summation method for the gravitational N-Body problem (i.e. estimate the force acting on each particles summing the contributions of all the other particles), which remains useful in collisional stellar dynamical system, but it is inefficient for large N due to the rapid increase of its computational cost with N. In this chapter we will see how this problem has been solved by new methods and new algorithms developed in the last forty years. Moreover during the last ten years, collisionless dynamics has also been coupled to gas dynamics, allowing a more direct link to observable quantities. New algorithms for collisionless systems and the implementation of the gas dynamics into the simulation codes allow immense progress in the studies of the non-linear gravitational clustering of dark matter, the formation of galaxies and clusters of galaxies, the interactions of isolated galaxies, the evolution of the intergalactic gas, etc. The obvious advantage of this method, with respect to SAMs, is that galaxy formation can be described by following in detail the evolution of the cosmic baryons during the shaping of large–scale cosmic structure. However, its limitation lies in its high computational cost, which makes it impossible to explore in detail the space of the parameter describing the process of galaxy formation and evolution. For this reason, following galaxy formation with full "hydrodynamical simulations" (simulations of collisional system described by the hydrodynamic equations) in a cosmological environment of several tens of Mpc is a challenging task for simulations of the present generation (e.g., Nagai & Kravtsov, 2005; Romeo et al.,

2005; Saro et al., 2006).

This chapter is divided in two parts: a first part in which we will describe from a general point of view in which way is it possible to treat a system composed by collisionless and collisional particles, which equations have to be solved and what are the main problems from a computational point of view. In the second part we will present the `GADGET-2` code (Springel et al. (2005), http://www.mpa-garching.mpg.de/gadget/), which is the one we used to perform our simulations.

5.1   N-Body methods

Let us consider a system composed by a number N of bodies of mass m_i. At the beginning (t=0) the position of each body is $\bar{x}_i(0)$ and the velocity is $\bar{v}_i(0)$. The equations that we have to solve in order to study the dynamics of the system are:

$$\frac{d\bar{x}_i}{dt} = \bar{v}_i \tag{5.1}$$

$$\frac{d\bar{v}_i}{dt} = \frac{\bar{F}_i}{m_i} \tag{5.2}$$

$$\nabla^2 \Phi = 4\pi G \rho(\bar{x}, t) \tag{5.3}$$

The first one is the velocity definition, the second one is the acceleration definition, and the third one is the Poisson equation. The numerical approach to these equations consists into solving the total derivatives in equations 5.1 and 5.3 using the finite methods differences. For example we replace the velocity analytical expression:

$$\bar{v}_i = \frac{d\bar{x}_i}{dt} = \lim_{\Delta t \to 0} \frac{\bar{x}_i(t + \Delta t) - \bar{x}_i(t)}{\Delta t} \tag{5.4}$$

with:

$$\bar{v}_i := \frac{\bar{x}_i(t + \Delta t) - \bar{x}_i(t)}{\Delta t} \tag{5.5}$$

We can summarize the N-body methods as follow:

1. Divide the time interval that you are going to study into segments of length Δt. The smaller are the segments, the more accurate will be the integration of the orbits.

2. Calculate the gravitational force that acts on each particle, from the Newton law:

$$\frac{\bar{F}_i}{m_i} = \sum_{j=1}^{N} \frac{G m_j}{|\bar{r}_{ij}|^3} \bar{r}_{ij} \tag{5.6}$$

where r_{ij} is the vector joining particle i and particle j ($j \neq i$).

3. Calculate for each particle the new position and velocity according to:

$$\bar{x}_{i,N} = \bar{x}_i(t + \Delta t) = \bar{x}_i(t) + \bar{v}_i(t)\Delta t \tag{5.7}$$

$$\bar{v}_{i,N} = \bar{v}_i(t + \Delta t) = \bar{v}_i(t) + \frac{\bar{F_i}(t)}{m_i}\Delta t \tag{5.8}$$

The operation that costs more in terms of time calculation is the second one (in particular the computing time grows as N^2). In fact, as it can be seen from 5.6, it is necessary to compute all the distances r_{ij} between the $N(N-1)/2$ possible pairs of particles. The different algorithms that we are going to illustrate in the following differ from one another for the methods used in order to calculate the gravitational force.

5.2 The Particle-Particle method

The Particle-Particle method, or shortly $PP - method$, is the most obvious one. It estimates the force acting on each particle by simply summing the contributions of all the particles in the simulation. It uses basically Newton equation, slightly modified in order to avoid the divergence of the force for distances approaching zero:

$$\frac{\bar{F}_i}{m_i} = \sum_{j=1}^{N} \frac{Gm_j}{(|\bar{r}_{ij}| + \epsilon)^3}\bar{r}_{ij} \tag{5.9}$$

ϵ is called *softening parameter* and assigns to each particle a characterist dimension. Moreover it defines a characteristic scale for the simulation. The simulation will be reliable on scale greater than ϵ.

   In this way one can estimate carefully the gravitational force but spend a lot of time. This is the reason why it is not possible to use PP method in simulations with a huge number of particles.

5.3 The Particle-Mesh methods

The Particle-Mesh (PM) method consists into solving the problem in a mean field approximation. The idea is to build a mesh and to assign at each point on the mesh a certain value of the density and potential. In this way it is possible to reduce significantly the number of computations that must be done. However introduction of a mesh causes a loss of spatial resolution, in the sense that it is not possible to resolve structures below the the dimension of the mesh. We can represent the space as a cubic volume os size L. Inside this cube we put the N particles and we build a mesh inserting M points, called the mesh nodes. The separation between the nodes is L/M and the volume of the M^3 cells is clearly $(L/M)^3$. For simplicity in the following we put $L = 1$. The PM computation can be divided in five steps:

1. Calculate the density within each cell : the mass of each particle is distributed on the mesh point according to this formula:

$$\rho(\bar{q}) = m_p M^3 \sum_{l=1}^{N} W(\bar{x}_i - \bar{q}) \tag{5.10}$$

where $\bar{q}$ is the the center of mesh point, $\bar{x}_i$ is the coordinate of particle i, and W is a function, called kernel, that interpolates the density field on the mesh, and it is normalized in order to preserve the total mass.

2. Solve Poisson equation (5.3) using FFT (Fast Fourier Transform). We get:

$$\Phi(\bar{q}) = \frac{1}{M^3} \sum_{\bar{q}} G(\bar{q} - \bar{q}')\rho(\bar{q}') \tag{5.11}$$

where $G(\bar{q})$ is the Green function of the Laplacian and it is proportional to $-1/q^2$

3. Calculate the force on each mesh point in the Fourier space:

$$\bar{F}(\bar{k}) = -i\bar{k}\Phi(\bar{k}) \tag{5.12}$$

and perform the anti-transformation in order to have $\bar{F}(\bar{q})$.

4. Calculate the force acting on each particle with the same interpolation scheme used for the density:

$$\bar{F}(\bar{x}_i) = \sum_{\bar{q}} W(\bar{x}_i - \bar{q})\bar{F}(\bar{q}) \tag{5.13}$$

This method is faster than the direct summation due to the fact the number of steps in the computation in FFT is on the order of $NlogN$.

5.4   The P^3M method

This method comes from the necessity to join the precision of PP method and the speed of PM. The idea is to divide the force acting on each particle in two contributions: a short one, $\bar{F}_i^{PP}$, treated with Particle-Particle method, and a long one, $\bar{F}_i^{PM}$, evaluated by particle-mesh method:

$$\bar{F}_i = \bar{F}_i^{PP} + \bar{F}_i^{PM} \tag{5.14}$$

Clearly it is necessary to introduce a critical distance, s_{cr}, that allows to discriminate between the two contributions. The choice depends on the compromise that one wants to have between the accuracy and the speed of the calculation: increasing the critical distance means enlarging the space region around each particle analyzed by PP method. The simulation is consequently more accurate but the execution time will be larger.

Some P^3M codes use adaptive meshes: this means that the spacing between two nodes can be increased or decreased due to the density of the region. In this way one can increase the resolution in the higher density regions (that are the most important for the final result) concentrating there most part of the calculation.

5.5   The Tree codes

The $TREE-CODE$ method is an algorithm that allows to increase the resolution in the forces computation, preserving roughly the speed of computation. This algorithm, originally proposed by Barnes & Hut (1986), is based on a hierarchical subdivision of space in regular cubic cells. At each time , before evaluating the force, a tree structure must be identified in order to fix the hierarchy. The rules to follow in order to build the tree can be summarize as follow:

1. Make a partition of the original box (computational domain) into a sequence of cubes. These cubes form the *principal nodes* of the tree structure;

2. Make a partition of each principal node into a certain number (that must be fixed at the beginning) of small cubes. These small cubes form the *secondary nodes* of the tree structure;

3. Perform the partition until each cube contains exactly one particle. In this case the cube is called the *leaves* of the tree structure;

4. Do not store the empty cubes.

A schematic illustration of Tree-Code in 2-D is given in picture 5.1 During the building of the tree structure one has to calculate and to assign at each cube the mass, the center coordinates and the quadrupole moments. The force is computed then walking the tree and summing up appropriate force contributions from the tree nodes. In the standard Barnes & Hutt tree walk, the multipole expansion of a node of lenght l is used only if:

$$r > \frac{l}{\theta} \tag{5.15}$$

where r is the distance of the point of reference to the center of mass of the cell and θ is an accuracy parameter that determines the execution speed.

If a node fulfills the criterion in equation 5.15, the tree walk along this branch can be terminated, otherwise it is opened and the walk is continued. A particular delicate issue is the force resulting from an almost homogeneous mass distribution; in this case single contributions tends to cancel each other and a relative small error can end up in a significant relative error in the final results. The criterion shown above does not guarantee a sufficient accuracy, so that other conditions must be fulfilled (see Springel et al., 2001 or Springel 2004).
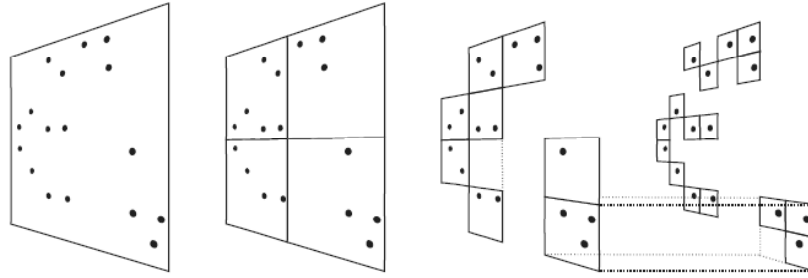
Figure 5.1: Schematic illustration of TREE-CODE in 2-D. The particles on left are enclosed in a square (root node).This square is then iteratively subdivided in four squares oh half size, until exactly one particle is left in each final square (leaves of the tree). Note that empty squares need not to be stored. (Springel, Yoshida & White 2001)

5.6 Hydrodynamics methods

In order to have a reliable representation of the matter distribution on large scale it is sufficient to use collisionless particles (N–body methods). However it is not possible to base a numerical analysis of the luminous matter in the universe only onto collisionless N-Body methods. In-fact the baryonic matter follows physical laws more complicated than the gravitational interaction. Consequently we have to think about some algorithm that are able to model gas behavior, particularly we have to describe the gas thermodynamics, the gas radiative and absorption properties and the influence of star formation. In order to implement these processes in numerical simulations it is necessary that the gas physics treatment is naturally complementary to the gravitational treatment. We will call that kind of simulations "hydrodynamical" due to the fact the gas particles can be described as hydrodynamical particle, as invented by Lucy (1977) and Gingold & Monaghan (1977).

5.6.1 Collisionless dynamics and gravity

Let start to discuss another formalism (Binney & Tremaine, 1987) to describe from a mathematical point of view a collisionless fluid that, as we already mentioned, is a good modelization of DM particles. It is useful to introduce it because it is easily expandable to the treatment of gas collisional particles. Let's consider a large number of particles moving under the influence of a smooth potential $\Phi(\bar{v}, t)$. At a certain time t , a full description of the state of any collisionless system is given by specifying the number of particles $f(\bar{x}, \bar{v}, t)$ having positions in the small volume d^3x centered on $\bar{x}$ and velocities in the small range d^3v centered on $\bar{v}$. The quantity $f(\bar{x}, \bar{v}, t)$ is called *distribution function* of the system. Clearly $f \geq 0$ everywhere in phase space. If we know the initial coordinates and velocities of every particles, Newton's law enable us to evaluate their positions and velocities at any later time. This means: given $f(\bar{x}, \bar{v}, t_0)$ it is possible to calculate $f(\bar{x}, \bar{v}, t)$ for any t using only

the informations that is contained in $f(\bar{x}, \bar{v}, t_0)$. In order to have a more compact notation we can define the coordinates in phase space as follows:

$$(\bar{x}, \bar{v}) := \bar{w} := (w_1, ..., w_6) \tag{5.16}$$

so the velocity of this flow may be written :

$$(\dot{\bar{x}}, \dot{\bar{v}}) := \dot{\bar{w}} = (\bar{v}, -\nabla\Phi) \tag{5.17}$$

A characteristic of the flow described by $\dot{\bar{w}}$ is that it conserves particles: in absence of encounters particles do not jump from one point in phase space to another, but rather drift smoothly through space. Then, the density of particles $f(\bar{w}, t)$ satisfies a continuity equation :

$$\frac{\partial f}{\partial t} + \sum_{\alpha=1}^{6} \frac{\partial(f\dot{w}_\alpha)}{\partial w_\alpha} = 0 \tag{5.18}$$

The flow described by $\dot{\bar{w}}$ has the property that:

$$\sum_{\alpha=1}^{6} \frac{\partial \dot{w}_\alpha}{\partial w_\alpha} = \sum_{i=1}^{3} \left(\frac{\partial v_i}{\partial x_i} + \frac{\partial \dot{v}_i}{\partial v_i} \right) = \sum_{i=1}^{3} -\frac{\partial}{\partial v_i} \left(\frac{\partial \Phi}{\partial x_i} \right) = 0 \tag{5.19}$$

Here $(\partial v_i/\partial x_i) = 0$ because v_i and x_i are independent coordinates of phase space, and the last step in equation 5.19 follows because $\nabla\Phi$ does not depend on the velocities. If we use equation 5.19 to simplify equation 5.18, we obtain the *collisionless Boltzmann equation*:

$$\frac{\partial f}{\partial t} + \bar{v} \cdot \nabla f - \nabla\Phi \cdot \frac{\partial f}{\partial \bar{v}} = 0 \tag{5.20}$$

where the gravitational potential Φ is defined through the Poisson equation:

$$\nabla^2\Phi(\bar{x}, t) = 4\pi G \int f(\bar{x}, \bar{v}, t)d\bar{v} \tag{5.21}$$

It is very difficult to solve this coupled system of equations (eq. 5.20 and 5.21) directly with finite difference methods. Instead, the common N–body approach is followed, where the phase fluid is represented by N particles which are integrated along the characterist curves of the collisionless Boltzmann equation. In essence, this is a Monte-Carlo approach whose accuracy depends crucially on a sufficiently high number of particles.

5.6.2 Collisional system: gas

Gas can be thought of as an ensemble of classical point-like ballistic particles which collide with each other. We can take into account the collisional behavior of the gas introducing one extra term in the Boltzmann equation:

$$\frac{df}{dt} = \left(\frac{\partial}{\partial t} + \dot{x}\nabla x + \dot{v}\nabla v \right) f = \left(\frac{\partial f}{\partial t} \right)_{coll} \tag{5.22}$$

The term on the right side of equation 5.22 takes into account the scattering of particles in and out of a phase–space region.

Defining the velocity average of some function F as :

$$\langle F \rangle = \frac{\int d^3v f F}{\int d^3v f} = \frac{1}{n} \int d^3v f F \qquad (5.23)$$

the conservation of F during collisions gives:

$$\int d^3v F(\bar{v}) \left(\frac{\partial f}{\partial t} \right)_{coll} = 0 \qquad (5.24)$$

and results in :

$$\frac{\partial n \langle F \rangle}{\partial t} + \frac{\partial n \langle F \bar{v} \rangle}{\partial \bar{x}} + n \frac{\partial \Phi}{\partial \bar{x}} \left\langle \frac{dF}{d\bar{v}} \right\rangle = 0. \qquad (5.25)$$

where Φ is the gravitational potential. Using the previous equation we can derive the conservation of mass, momentum and energy.

Setting $F = m$ in equation 5.25 we obtain:

$$\frac{\partial \rho}{\partial t} + \nabla \cdot (\rho \bar{u}) = 0 \qquad (5.26)$$

where $\rho = nm$ and

$$\bar{u} = \frac{\int d^3v f \bar{v}}{\int d^3v f} \qquad (5.27)$$

is the bulk velocity. Equation 5.27 is known as the *continuity equation* and tells us that the mass variation within a volume must be equal to the mass flux across the surface defining the same volume. If the observer is moving along with the stream, it will observe

$$\frac{D\rho}{Dt} = -\rho \nabla \cdot \bar{u} \qquad (5.28)$$

being $D/Dt = \partial/\partial t + \bar{u} \cdot \nabla$ the *Lagrangian derivative*.

If $F = m$ equation 5.25 yields to:

$$\frac{\partial \rho u_i}{\partial t} + \frac{\partial \rho \langle v_i v_k \rangle}{\partial x_k} + \rho \frac{\partial \Phi}{\partial x_i} = 0 \qquad (5.29)$$

Writing the velocity $\bar{v}$ as $\bar{v} = \bar{u} + \bar{w}$ where $\bar{w}$ is the velocity of 'random' motions with respect to the mean velocity $\bar{u}$ and having $\rho < v_i v_k >= P\delta_{ik} - \pi_{ik}$ with the gas pressure

$$P = \rho \langle |\bar{w}|^2 \rangle / 3 \qquad (5.30)$$

and the viscous stress tensor

$$\pi_{ik} = \rho \langle |\bar{w}|^2 \delta_{ik}/3 - w_i w_k \rangle \qquad (5.31)$$

equation 5.25 now reads

$$\frac{\partial \rho u_i}{\partial t} + \frac{\partial}{\partial x_k}(\rho u_i u_k + P\delta_{ik} - \pi_{ik}) = -\rho \frac{\partial \Phi}{\partial x_k} \quad (5.32)$$

Using equation 5.26 we obtain *Force equation*

$$\rho \frac{D\bar{u}}{Dt} = -\rho \nabla \Phi - \nabla P + \nabla \cdot \bar{\pi} \quad (5.33)$$

being $(\nabla \cdot \pi)_i = \partial \pi_{ik}/\partial x_k$.

Equation 5.25 becomes the law of energy conservation if $F = mv^2/2 = mu^2/2 + mw^2/2 + m\bar{w} \cdot \bar{u}$. To derive it, let us define the *specific internal energy* as:

$$\rho\epsilon = \rho\langle w^2/2\rangle = 3P/2 \quad (5.34)$$

and the *heat conduction flux* $\bar{F}$ as

$$F_k = \frac{1}{2}\rho\langle w_k w^2\rangle \quad (5.35)$$

so that we obtain the *total energy conservation law*

$$\frac{\partial}{\partial t}\left(\frac{1}{2}\rho u^2 + \rho\epsilon\right) + \frac{\partial}{\partial x_k}\left(\frac{1}{2}\rho u_k u^2 + u_i(P\delta_{ik} - \pi_{ik}) + \rho\epsilon u_k + F_k\right) = -\rho u_k \frac{\partial \Phi}{\partial x_k} \quad (5.36)$$

which can be rewritten as the following *internal energy* equation

$$\frac{\partial \rho\epsilon}{\partial t} + \frac{\rho\epsilon u_k}{\partial x_k} = -P\frac{\partial u_k}{\partial x_k} - \frac{\partial F_k}{\partial x_k} + \Psi \quad (5.37)$$

where the *rate of viscous dissipation* Ψ is defined as:

$$\Psi = \pi_{ik}\frac{\partial u_i}{\partial x_k} = \frac{1}{2}\pi_{ik}\left(\frac{\partial u_i}{\partial x_k} + \frac{\partial u_k}{\partial x_i}\right) \quad (5.38)$$

Using the continuity equation we have finally:

$$\rho\frac{D\epsilon}{Dt} = P\nabla \cdot \bar{u} - \nabla \cdot \bar{F} + \Psi \quad (5.39)$$

Collecting together the continuity equation, the force equation and the internal energy equation that represent the moments of the Boltzmann' transport equation, we can have all the *Navier-Stokes equations*:

$$\left(\frac{\partial}{\partial t} + \bar{u} \cdot \nabla\right)\rho = -\rho\nabla \cdot \bar{u} \quad (5.40)$$

$$\rho\left(\frac{\partial}{\partial t} + \bar{u} \cdot \nabla\right)\bar{u} = -\rho\nabla\Phi - \nabla P + \nabla \cdot \bar{\pi} \quad (5.41)$$

$$\rho\left(\frac{\partial}{\partial t} + \bar{u} \cdot \nabla\right)\epsilon = -P\nabla \cdot \bar{u} - \nabla \cdot \bar{F} + \Psi \quad (5.42)$$

being

$$\rho = m \int d^3v f(\bar{x}, \bar{v}, t) \tag{5.43}$$

$$\bar{u} = <\bar{v}> \tag{5.44}$$

$$\epsilon = \frac{3}{2}\frac{P}{\rho} = \frac{1}{2} < w^2 > \tag{5.45}$$

$$\pi_{ik} = \rho < |\bar{w}|^2 \delta_{ik}/3 - w_i w_k > \tag{5.46}$$

$$F_k = \frac{1}{2}\rho < w_k w^2 > \tag{5.47}$$

$$\Psi = \pi_{ik}\frac{\partial u_i}{\partial x_k} \tag{5.48}$$

Note that the previous equations have been written in their *non conservative form*, i.e. from the point of view of a particle moving in the fluid, which is the Lagrangian approach used in simulations. It is also worthwhile to note that $\nabla\Phi$ should be substituted by a more general term $\bar{f}$, which stands for a general external force per unit mass exerted on a gas volume, when accounting for some other fields than gravitation, e.g. magnetic field (Dolag et al. 2002). So far we have written three equations: the continuity equation, the Euler equation and the energy equation. To close the system we also need a fourth relation, namely the *equation of state* which relates the thermodynamical variables with each others. This is:

$$P = (\gamma - 1)\rho u \tag{5.49}$$

where $\gamma = 5/3$ is the adiabatic exponent for a mono-atomic ideal gas and ϵ is the energy per unit mass.

The form we use in numerical simulation we run is different from Navier-Stokes equations because, as it is usual in cosmological simulations, we ignore the viscous stress tensor and thermal flux terms, then considering the collisional component as a perfect gas. Then the governing equations are:

$$\left(\frac{\partial}{\partial t} + \bar{u} \cdot \nabla\right)\rho = -\rho\nabla \cdot \bar{u} \tag{5.50}$$

$$\left(\frac{\partial}{\partial t} + \bar{u} \cdot \nabla\right)\bar{u} = -\nabla\Phi - \frac{\nabla P}{\rho} \tag{5.51}$$

$$\left(\frac{\partial}{\partial t} + \bar{u} \cdot \nabla\right)\epsilon = -\frac{P}{\rho}\nabla \cdot \bar{u} - \frac{L(\epsilon, \rho)}{\rho} \tag{5.52}$$

neglecting other terms than gravity as for the external forces and accounting for non-hydrodynamical heating and cooling through the L function.

5.7 Eulerian and Lagrangian approach to computational fluid dynamics

Considering the continuity equation (5.27) one can infer the existence of two different approach to describe the motion of fluids, namely the *Eulerian* and the *Lagrangian*. As for the former, the fluid is studied considering the properties of a fixed volume in space and studying their variations with space and time. This is what the left hand in equation 5.28 refers to. In the second approach, the fundamental object of our analysis is a volume of fluid whose properties are studied along its trajectories: then, the derivative in the left hand side of mentioned equation 5.28 will be for density:

$$\frac{d\rho(x,y,z,t)}{dt} = \frac{\partial\rho}{\partial t} + \frac{\partial\rho}{\partial x}\frac{dx}{dt} + \frac{\partial\rho}{\partial y}\frac{dy}{dt} + \frac{\partial\rho}{\partial z}\frac{dz}{dt} \tag{5.53}$$

leading to the right hand side of equation 5.28. Less formally, we can say that the first term $\partial/\partial t$ of the Lagrangian derivative carries informations about the "local" or "intrinsic" variation whereas the second one ($\bar{v} \cdot \nabla$, the convective derivative) describes the variation due to the surrounding environment. Both Eulerian and Lagrangian methods present advantages and disadvantages. In particular Eulerian approaches are best suited as shock-capturing methods and resolve better the under-dense regions and arbitrarily large gradients, while Lagrangian codes are not locked to a pre-defined geometry and can adapt the resolution to the local needs allowing for wide spatial and dynamical ranges. Depending on the problem one is dealing with, one choice or another is preferable: for a while Lagrangian methods have been the ones used for the bulk of works in computational cosmology since they are free of fixed geometries and the ability in managing the huge dynamical ranges that a typical problem in this field present, e.g. with three or more order of magnitude as for the density contrast. As a final, quite obvious, note, it is worth to mention that Eulerian codes are better suited to calculate fluxes and quantity exchanges. e.g. mass fluxes (and then diffusion equations), radiative transport etc, while a particle description is useful when dealing with well-separated phase, e.g. in studying the star formations.

5.8 SPH Code

Real fluids consist of an infinite number of infinitesimal-extended elements which move obeying the Newtonian equations under the influence of pressure gradients and other, if any, external forces like gravity, magnetic field, inertial forces from rotating system etc. For obvious reasons it is definitely impractical to model such real fluids in the computational realm, so that the standard approach is to select a set of N finite elements, representing them by particles, and assume that their mass density is proportional to the mass density of the fluid so that the latter can be inferred given the former if the system is evolving following the laws of

thermodynamics. In recovering the density ρ of the fluid from the distribution of particles we are basically recovering a probability distribution from a sample. To do this we have to smear out the local statistical fluctuations due to the finite number of used elements. In the SPH technique, this task is accomplished using the smoothing kernel methods as first presented by Lucy (1977) and Gingold and Monaghan (1977). Following the original discussion of Gingold and Monaghan, the heart of the SPH technique is the evaluation of a smoothed scalar or vector field $A(\bar{r})$

$$A_s(\bar{r}) = \int W(\bar{r} - \bar{r}', h) A(\bar{r}') d\bar{r}' \tag{5.54}$$

by a Monte-Carlo method from a set of N points at coordinates $\bar{r}_1, ... \bar{r}_N$:

$$A_N(\bar{r}) := \sum_{j=1}^{N} \frac{A(r_j)}{n_j} W(\bar{r} - \bar{r}', h) \tag{5.55}$$

$W(\bar{r} - \bar{r}', h)$ is the so called *interpolant kernel*, n_j is the local number density of particles at the point $\bar{r}_j$ and h is a sort of resolution in the sense that every properties with length scale $l \ll h$ is strongly smoothed. The kernel W must satisfy the condition:

$$\int W(\bar{r}) d\bar{r} = 1 \tag{5.56}$$

where the integration is over all space. Intuitively it seems reasonable to expect that $W(\bar{r})$ can be made more like $\delta(\bar{r})$ as N becomes larger. If this is the case then

$$A_s(\bar{r}) \to A(\bar{r}) \quad as \quad N \to \infty \tag{5.57}$$

To make the result more precise it is convenient to write $W(\bar{r})$ in the form

$$W(\bar{r}) = \frac{1}{h^3} K(\bar{r}/h) \tag{5.58}$$

By an easy generalization of a theorem due to Parzen (1962) we find that if $h \to 0$ as $N \to \infty$ and if $K(\bar{u})$ is a Borel function satisfying

$$\int K(\bar{u}) d\bar{u} = 1, \quad |\bar{u}^2 K(\bar{u})| \to 0 \quad as \quad |\bar{u}| \to \infty, \quad \int |K(\bar{u})| d\bar{u} < \infty \tag{5.59}$$

then our request 5.57 is satisfied. It is worth to mention that the error in using equation 5.55 instead of equation 5.54 depends on the disorder of the particles and is normally $O(h^2)$ or better ((Monaghan & Lattanzio, 1985), (Monaghan, 1992)). By using a differentiable kernel, our estimates are also differentiable and the derivatives of the interpolant are constructed just using derivatives of Kernel, so that:

$$\nabla A_s(\bar{r}) = \int W(\bar{r} - \bar{r}', h) \nabla A(\bar{r}') d\bar{r}' \tag{5.60}$$

becomes, after integrating by part,

$$\nabla A_s(\bar{r}) = \int A(\bar{r}')\nabla W(\bar{r} - \bar{r}', h)d\bar{r}' \tag{5.61}$$

as long as we can ignore surface terms, which we are allowed to if $AW \to 0$ on the boundary. This hypothesis is satisfied because generally the kernel vanishes rapidly for $|\bar{r} - \bar{r}'| \to \infty$. In the discrete approximation the previous equation become:

$$\nabla A_s(\bar{r}) = \sum_{j=1}^{N} \frac{A(r_j)}{n_j}\nabla W(\bar{r} - \bar{r}', h)d\bar{r}' \tag{5.62}$$

in other words, W must be differentiable up to the same order as that of terms present in the equations to be integrated: for instance, ∇W must exist for non-pressureless medium and ∇^2 must exists if we introduce the diffusion equation (e.g. to calculate heat conduction or describe diffusive phenomena).

5.9 Fundamental equations of Hydrodynamics in SPH

In this section we will give the expression of the fundamental equations of hydrodynamics in SPH without writing all the details. Fundamentally all the equations can be derived by the general treatment given in previous section. To have more details we refer to Hernquist & Katz (1989). From equation 5.55 one can estimate the mass density $\rho(\bar{r})$ with $n_j = \rho_j/m_j$:

$$\rho_s(\bar{r}) = \sum_{j=1}^{N} m_j W(\bar{r} - \bar{r}', h) \tag{5.63}$$

Using this equation and equation 5.62 we can translate the continuity equation in SPH language as follow:

$$\frac{d\rho_i}{dt} = \sum_{j=1}^{N} m_j(\bar{v}_i - \bar{v}_j)\nabla_i W_{ij} \tag{5.64}$$

where ∇_i stands for the gradient taken with respect to coordinates of particle i and $W_{ij} = W(\bar{r} - \bar{r}', h)$. In a similar way we can derive the momentum equation:

$$\frac{d\bar{v}_i}{dt} = -\sum_{j=1}^{N} m_j\left(\frac{P_j}{\rho_j^2} + \frac{P_i}{\rho_i^2}\right)\nabla_i W_{ij} \tag{5.65}$$

and the energy equation:

$$\frac{du_i}{dt} = \frac{1}{2}\sum_{j=1}^{N} m_j\left(\frac{P_j}{\rho_j^2} + \frac{P_i}{\rho_i^2}\right)\bar{v}_{ij}\nabla_i W_{ij} \tag{5.66}$$

5.10 The kernel choice

Under the general request given in the previous sections, many kernels are found to work in SPH. Although a Gaussian kernel $1/(h^2\pi)^{3/2}e^{-r_{ij}^2/h^2}$ would provide the easiest interpretation of the physical meaning of equations, it has the disadvantage of a slow fall off with the r_{ij}/h ratio, so that virtually all particles will contribute to the properties of each one. This is a disadvantages for two reasons. Firstly, it involves an higher computational effort, secondly the local nature of the physical properties will be also smoothed while it would be better to retain them as local as possible. To avoid this drawbacks, other kernels have been proposed, mainly based on spline functions with compact support as they ensure continuity of derivatives and good interpolation properties. A wide used kernel is the B-spline based kernel:

$$W(\bar{r}, h) = \frac{3}{4\pi h^2} \begin{cases} \frac{10}{3} - 7u^2 + 4u^3 & \text{if } 0 \leq u \leq 1 \\ (2-u)^2(\frac{5-4u}{3}) & \text{if } 1 \leq u \leq 2 \\ 0 & \text{if } u \geq 2 \end{cases}$$

The smoothing length is chosen according to the required precision for the simulation. For an optimized resolution it is necessary to have $30-50$ nearby particles. If h is assumed to be constant the computation in low–density region is not accurate: due to this region in modern SPH code the smoothing length varies for each particles. In this way the particle's resolution is a function of the local thermodynamic conditions.

5.11 Artificial viscosity

Due to the intrinsic limitation in spatial resolution, every numerical methods will lead to some piling of high frequency waves up to the extreme numerical mode. This could result in more or less severe numerical instability where high wave numbers are intrinsically present as in case of discontinuities, for instance when a shock occurs. Furthermore, as for the classical SPH derivation, a method is needed to prevent particles interpenetration, which would make the fluid properties multivalued. Besides this genuinely numerical issue, one also has to mimic the true physical viscosity that is neglected in the ideal gas approach.

To this purpose, the Von Neumann-Richtmeyer approach of adding an *Artificial Viscosity* is commonly followed. Many forms of artificial viscosity have been proposed so far but the symmetrized form for the classical artificial viscosity suggested by Monagan (1992) has probably been the most widely used:

$$\Pi_{ij} = \frac{-\alpha\mu_{ij}c_{ij} + b\mu_{ij}}{\rho_{ij}} \qquad (5.67)$$

where α and β are constant, $c_{ij} = (c_i - c_j)/2$ (c is the sound speed), and

$$\mu_{ij} = \begin{cases} \frac{\bar{v}_{ij}\bar{r}_{ij}}{h_{ij}(|\bar{r}_i-\bar{r}_j|^2/h_{ij}^2+\eta^2)} & \text{if } \bar{v}_{ij}\dot{\bar{r}}_{ij} < 0 \\ 0 & \text{if } \bar{v}_{ij}\dot{\bar{r}}_{ij} \geq 0 \end{cases}$$

having, as before, $\bar{v}_{ij} = \bar{v}_i - \bar{v}_j$ and $\bar{r}_{ij} = \bar{r}_i - \bar{r}_j$. This is a combination of a bulk viscosity and the Von Neumann-Richtmeyer viscosity, respectively linear and quadratic in μ_{ij}. This form is very effective in preventing particles' interpenetration in strong compression regions due to its dependence on pairwise produces $\bar{v}_{ij}\dot{\bar{r}}_{ij}$. For the same reason, when this terms are non-null but the particles are not getting a head-head collision (as in shear flows), the resulting viscosity does not vanish, becoming a shear viscosity in a side-effect.

5.12 GADGET-2

GADGET-2 (*GAlaxies with Dark matter and Gas intEracT*) is a freely available code for cosmological N-body/SPH simulations on massively parallel computers with distributed memory. It computes gravitational forces with a hierarchical tree algorithm (optionally in combination with a particle-mesh scheme for long-range gravitational forces) and represents fluids by means of smoothed particle hydrodynamics (SPH). The code can be used for studies of isolated systems, or for simulations that include the cosmological expansion of space. In all these types of simulations, GADGET-2 follows the evolution of a self-gravitating collisionless N-body system. Besides gravitational and hydrodynamical treatment of the gas in an expanding background, the code also implements several physical processes: radiative cooling, ionizing effect of the UV background, star formation process for multi-phase gas, magnetic field, chemical enrichment, thermal conduction, cosmic rays, etc. A comprehensive review of its features is given in a number of article by its author Volker Springel (Springel et al. (2001), Springel et al. (2005)).

5.12.1 Integration scheme

Once all the equations have been written down, the integration scheme must be specified. One of the most common methods used to solve a system of differential equations is the ones developed at the beginning of the last century by Runge & Kutta. This methods is quite fast but it introduces some perturbations that strongly influence the final solution. Consequently in GADGET-2 a symplectic integrator is used that preserves the phase–space structure and allows to have a solution closer to the real one. Particularly the symplectic scheme used is the "leapfrog" developed by Quinn et al. (1997),Preto & Tremaine (1999). The name is due to the way in which the positions $\bar{r}$ and the velocities $\bar{v}$ are updated at each step n:

$$\bar{v}_{n+1/2} = \bar{v}_n + \frac{1}{2}\tau\bar{a}(\bar{r}_n)$$
$$\bar{r}_{n+1} = \bar{r}_n + \tau\bar{v}_{n+1/2}$$
$$\bar{v}_{n+1} = \bar{v}_{n+1/2} + \frac{1}{2}\tau\bar{a}(\bar{r}_{n+1}) \tag{5.68}$$

where $\bar{a}$ is the acceleration and τ the time interval. From a numerical point of view, a "symplectic integrator is an exact solution to a discrete Hamiltonian system that

is close to the continuum Hamiltonian of interest" (Quinn et al., 1997). Then, the integration will conserve an energy that is an approximation to the true energy of the system: if the difference is small, almost all the orbits that are stable in the real system will continue to be stable in the discrete representation.

We have now to specify the choice of the time step τ. It is useful to use an adaptive time–steppening, that allows to follow more in details the particles on which acts strong forces. Quinn et al. (1997) make use of a decomposition of the overall integration time in power of two subdivisions, then restricting the choice for the time step of the particle i at the step n to:

$$\tau_i^n = \frac{\tau_{total}}{2_{i,n}^k} \tag{5.69}$$

for some integer $k_{i,n} < K$ where $\tau_{total}/2^K$ is the minimum step allowed.

Chapter 6

Simulations of isolated halos

In this chapter we will present the details of the simulations that we have performed. We simulated isolated DM halos in which the gas sits in hydrostatic equilibrium and it is allowed to cool down radiatively. The statement "isolated halos" means that the halos are not formed through a hierarchical process in a cosmological context, as it's supposed to happen in the real world. This means that we neglect the merging history of each halo that affects the gas behavior in the DM potential wells. It is clear that our simulations are totally unrealistic, because any feedback mechanism are neglected, both and because we don't take into account the influence that the mergers have on the gas. However this controlled numerical experiment allow us to study in detail the effect of pure radiative cooling of the gas and therefore allow a more precise comparison with SAMs. We will discuss this point in the next chapter.

6.1   Initial conditions

As it is clear, one of the crucial points for a numerical simulation is the generation of initial conditions. Initial conditions for isolated halos have been created by placing gas in hydrostatic equilibrium within a DM halo, having a NFW density profile (see equation 2.1). In order to ensure hydrostatic equilibrium we followed the approach by Komatsu & Seljak (2001), described in chapter 2, who provide the expression for the gas density profile given by equation 2.17. In order to generate initial conditions, the analytical profiles (equations 2.1 and 2.17) must be discretized into individual particles and the initial particle positions, velocities and internal energy must be specified.

We stress here that the gas density analytical profile (eq. 2.17), has been obtained assuming the gas mass vanishing, that is not the case of the simulations. We will came back on this point in the following section.

Initial positions of DM and gas particles are generated by Monte-Carlo sampling the analytical profiles of equations 2.1 and 2.17. To create an equilibrium configuration for the DM halo, initial velocities of the particles are assigned according to a local Maxwellian approximation (Hernquist, 1993). On the other hand, since equations 2.17 and 2.18 are hydrostatic solution, gas particles are initially assigned

zero velocity. In the following we discuss only the main ideas and equations of this approach. We assume that the mass distribution is spherical, then the second order moment of the collisionless Boltzmann equation reads:

$$\frac{d(\rho \bar{v}_r^2)}{dr} + \frac{\rho}{r}[2\bar{v}_r^2 - (\bar{v}_\theta^2 + \bar{v}_\phi^2)] = -\rho \frac{d\Phi}{dr} \tag{6.1}$$

where $\bar{v}_r^2$, $\bar{v}_\theta^2$, $\bar{v}_\phi^2$ are the dispersions in spherical coordinates (e.g. Binney & Tremaine 1987). If the system is also isotropic we can integrate this equation to give:

$$\bar{v}_r^2 = \frac{1}{\rho(r)} \int_r^\infty \rho(r) \frac{d\Phi}{dr} dr \tag{6.2}$$

Here Φ includes not only the self-gravity of the halo but the contributions of the other components to the gravitational field as well. We can rewrite equation 6.2 in the form:

$$\bar{v}_r^2 = \frac{1}{\rho(r)} \int_r^\infty \rho(r) GM(r) r^2 dr \tag{6.3}$$

where $M(r)$ is the cumulative mass distribution :

$$M(r) = \int_0^r (u^2(\rho_{gas}(u) + \rho_{DM}(u)) du \tag{6.4}$$

We have now to select a function whose second order moment is v_r^2. An obvious choice is a Gaussian. In practice, it is convenient to select speeds of particles from

$$F(v, r) = 4\pi \left(\frac{1}{2\pi\sigma^2}\right)^{3/2} v^2 \exp(-v^2/2\bar{v}_r^2) \tag{6.5}$$

where $F(v, r)$ is normalized to 1. Once the speed of a halo particle has been chosen, the Cartesian velocity components are initialized from v, assuming isotropy.

Finally the internal energy for the gas particles is assigned according to the effective polytropic equation of state.

Each halo has been sampled with $6 \cdot 10^4$ DM particles inside R_{200} and an initially equal number of gas particles. The ratio between the mass of DM and gas particles is determined by the baryon fraction, that we assumed to be $f_{bar} = 0.19$. To ensure stability of the halos in the absence of cooling, density profiles have been sampled with particles out to about $8r_{200}$. This also ensure an adequate reservoir of external gas that can flow in while cooling removes support in the central halo regions.

6.2 Non–radiative simulations

Before performing radiative simulations (i.e. before turning the cooling on in the code) we did a set of simulations without cooling in order to check that the gas in DM halos is in hydrostatic equilibrium. We simulated 12 different halos spanning a range in mass from 10^{11} to $10^{15} M_\odot$ with effective polytropic index from 1.1 to 1.25. For each halo we calculated the concentration parameter following Navarro

et al. (1997). The characteristic of the simulated halos are summarized in Table 1. We note that in this table is also specified the redshift. Although redshift never explicitly enters in our simulations of isolated halos, it appears in a indirect way when we fix the value of critical density. Ultimately, increasing redshift amounts to take higher value of ρ_{crit} and , therefore, a higher halo density for a fixed value of M_{200}. In this way we expect that "high–redshift" halos will have a shorter cooling time. In the following we assume the relation between redshift and critical density holding for a cosmological model with $\Omega_m = 0.3$ and $\Omega_\Lambda = 0.7$. Our reference halo has a mass $M_{200} = 10^{13} M_\odot$ (halo no. 1 in Table 1), typical of a poor galaxy group, with a concentration of $C_{NFW} = 6.3$ and $r_{200} = 350 kpc$. Two other halos of the same mass have been also simulated, having different values of the concentration parameter, still lying within the scatter in the $M_{200} - C_{NFW}$ relation (halos no. 2 & 3). For the three halos we used the same value $\gamma = 1.18$ for the effective polytropic index. We simulated another halos (halos no. 5) with the same value of the concentration parameter of halo no. 1, but with different effective polytropic index ($\gamma = 1.25$). We have then simulated smaller and larger halos than the reference one, spanning a range in mass from $M = 10^{11} M_\odot$ to $M = 10^{15} M_\odot$, so as to sample more or less all the scales from elliptical galaxies to rich clusters (halos no. 4,6,7,8 & 9). We have finally considered two halos at $z = 1$ (halos no. 10 & 11) and one halo at $z = 2$ (halo no. 12). In table 1 we report for each halo the values of dynamical time-scale, which is defined as

$$t_{dyn} = \left(\frac{1}{4\pi G \rho} \right)^{1/2} \tag{6.6}$$

and that of the cooling time calculated at the center of the halo,

$$t_{cool} = \frac{3 k_B T_0 \mu m_p}{2 \rho_0 \Lambda(T_0)} \tag{6.7}$$

Moreover in Table 1 we specify for which simulation we have performed also the radiative runs.

In principle, our controlled numerical experiments could have been performed by using a static NFW potential, instead of sampling the halo with DM particles. Although this procedure would have allowed to save CPU time, it does not permit to account for any backreaction of cooling on the DM component. Indeed it is known from cosmological simulations that including gas cooling causes a small but sizeble change of the DM halos. As for the choice of the gravitational softening, it has been always chosen to be about three times larger than the lower limit recommended by Power et al. (2003), $\epsilon = 3 r_{200} / \sqrt{(N_{200})}$, where N_{200} is the number of particles within r_{200}. Only for the halo no. 1, we also generated initial conditions at higher resolution by using 10 times more particles, in order to check for numerical convergence for our final results (see fig. 6.2).

All the initial condition were first evolved for 10 dynamical times. This allowed us to check that temperature and density profiles are always stable, thus confirming that the initial conditions roughly correspond to configurations of hydrostatic

	$M_{200}(M_\odot)$	γ	C_{NFW}	$redshift$	$R_{200}(kpc)$	$t_{dyn}(Gyr)$	$t_{cool}(Gyr)$
1	$10^{13}(c)$	1.18	6.3	$z=0$	350	0.56	0.56
2	$10^{13}(c)$	1.18	7.25	$z=0$	350	0.56	0.4
3	$10^{13}(c)$	1.18	5.25	$z=0$	350	0.56	0.82
4	10^{14}	1.10	6.3	$z=0$	750	0.56	
5	10^{13}	1.25	6.3	$z=0$	350	0.56	
6	10^{11}	1.18	8.1	$z=0$	75	0.56	
7	$10^{12}(c)$	1.18	7.25	$z=0$	162	0.56	0.12
8	10^{14}	1.18	5.25	$z=0$	753	0.56	
9	$10^{15}(c)$	1.18	4.3	$z=0$	1623	0.56	6.67
10	$3\cdot10^{11}(c)$	1.18	6.53	$z=1$	75	0.32	0.04
11	$10^{13}(c)$	1.18	5.63	$z=1$	241	0.33	0.31
12	$10^{12}(c)$	1.18	5.92	$z=2$	79	0.19	0.04

Table 6.1: Scheme of performed simulations.In the first column we report the halo's mass, in the second the effective polytropic index γ, in the third the concentration parameter C_{NFW}, in the fourth the redshift z, in the fifth the value of R_{200} in the sixth the dynamical time t_{dyn} as defined in equation 6.6 and in the seventh the cooling time as defined in equation 6.7. Moreover we have also indicated the simulation for which we have performed the radiative runs. (c).
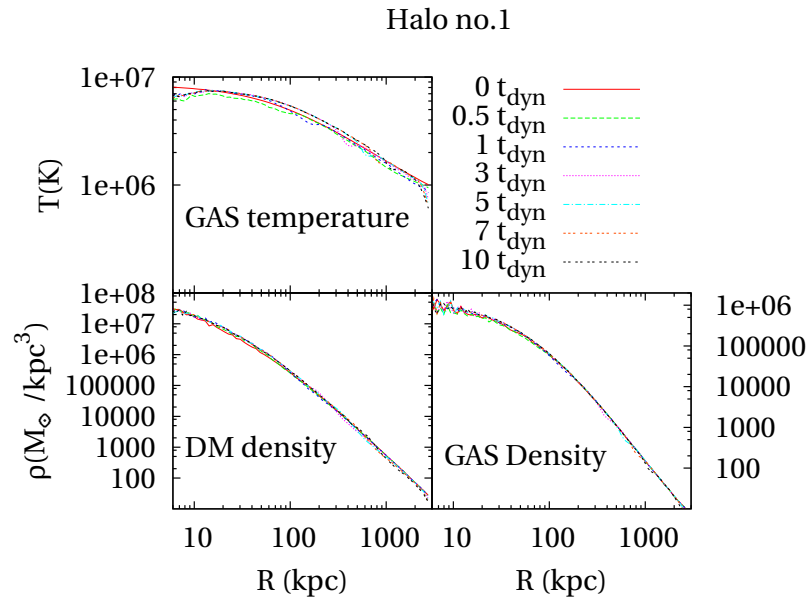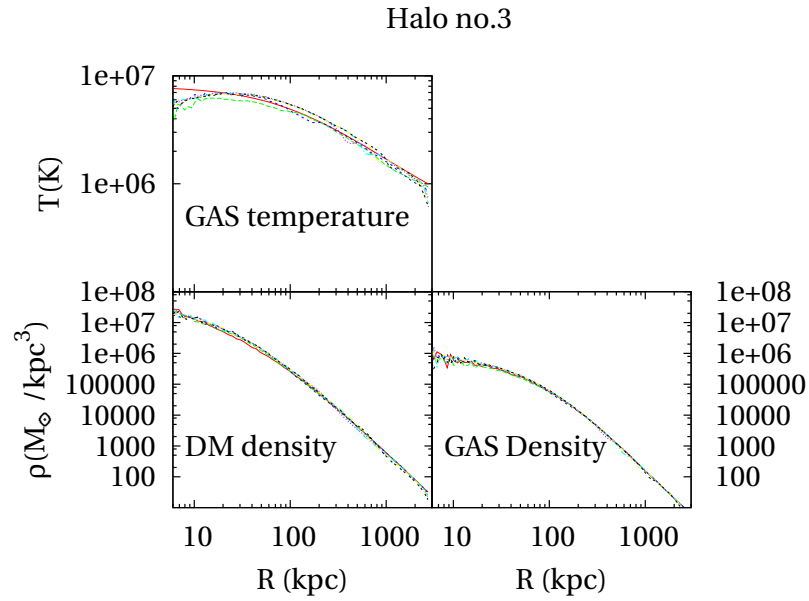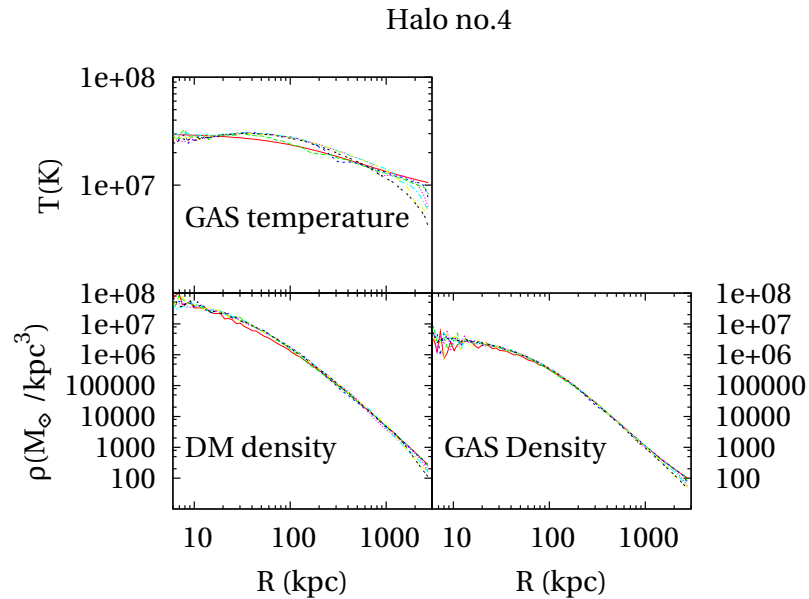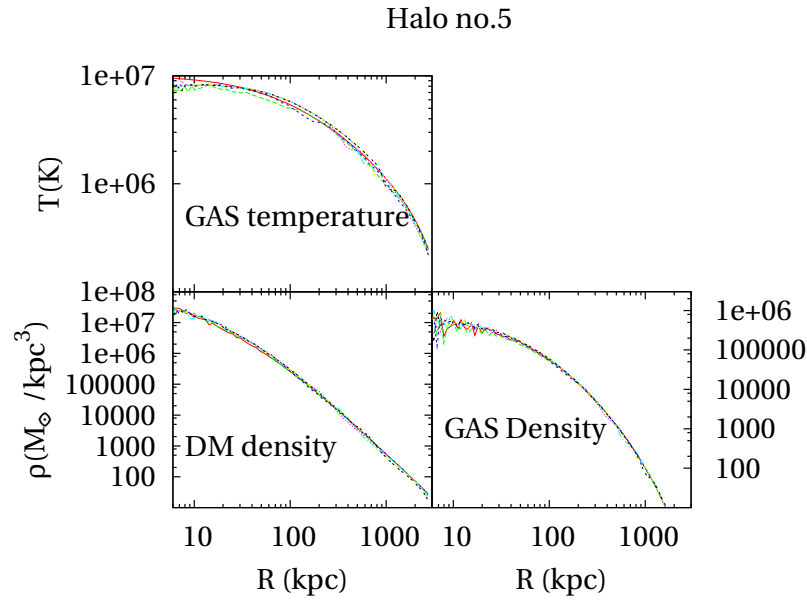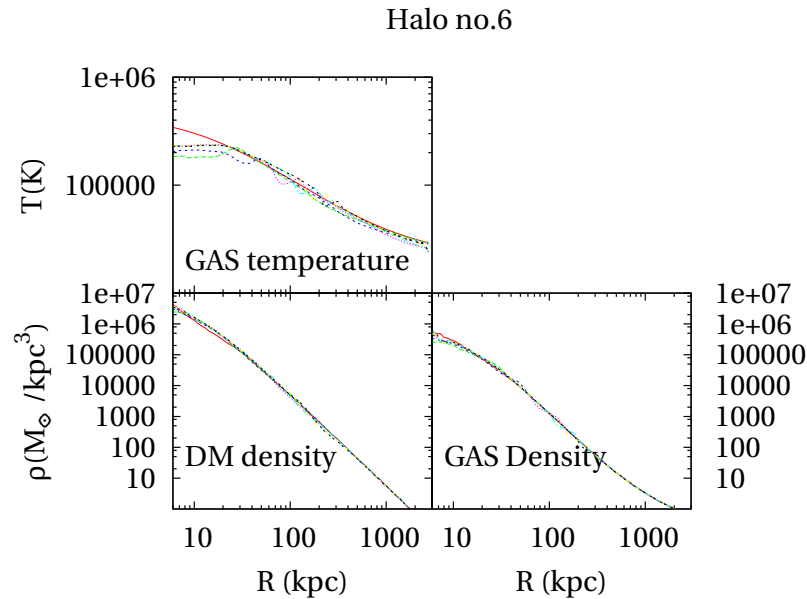

Figure 6.1: Gas temperature profile (*Top panel*), DM density profile *Bottom left panels*, GAS density profile *Bottom right panel* for simulation no.1 (with $6\cdot10^4$ particles) evaluated at 7 times in the interval $[0,10]t_{dyn}$.
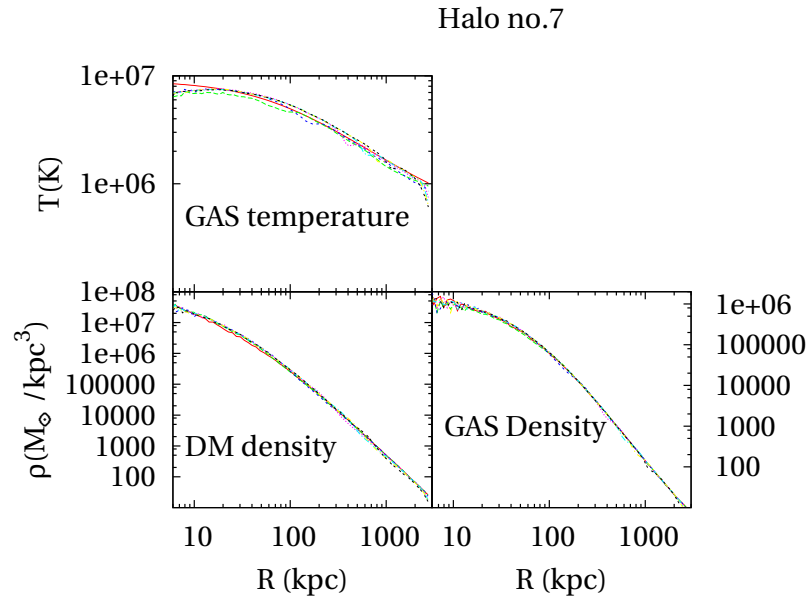
Halo no.1 (High Resolution)
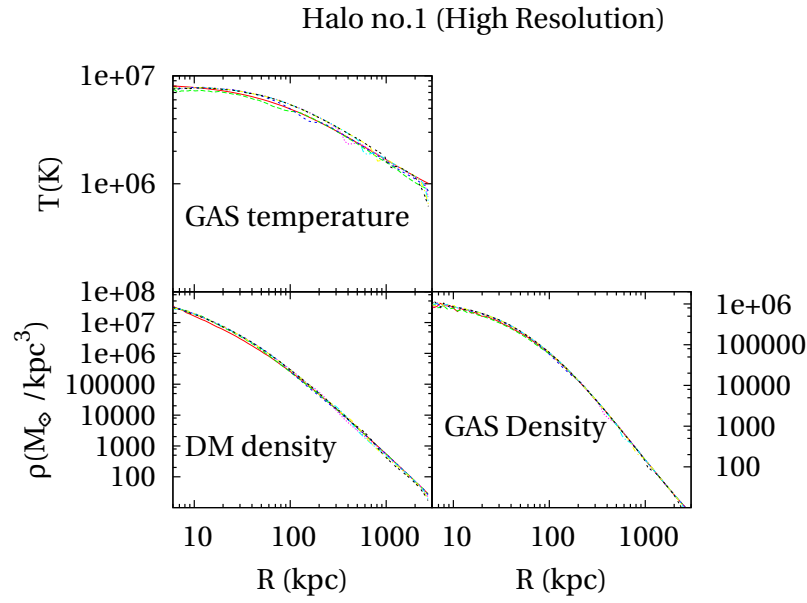
Figure 6.2: Gas temperature profile (*Top panel*), DM density profile *Bottom left panels*, GAS density profile *Bottom right panel* for simulation no.1 (with $6 \cdot 10^5$ particles) evaluated at 7 times in the interval $[0, 10]t_{dyn}$.

Halo no.2
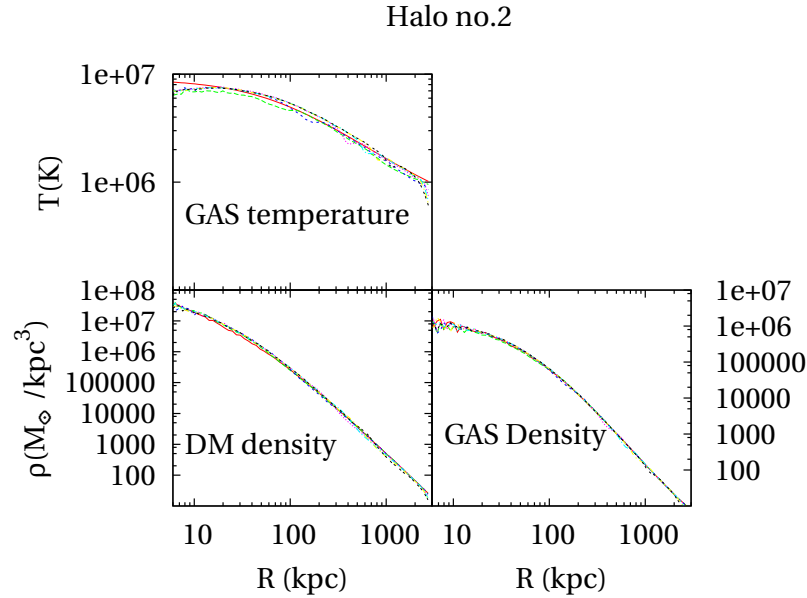
Figure 6.3: Gas temperature profile (*Top panel*), DM density profile *Bottom left panels*, GAS density profile *Bottom right panel* for simulation no.1 (with $6 \cdot 10^4$ particles) evaluated at 7 times in the interval $[0, 10]t_{dyn}$.
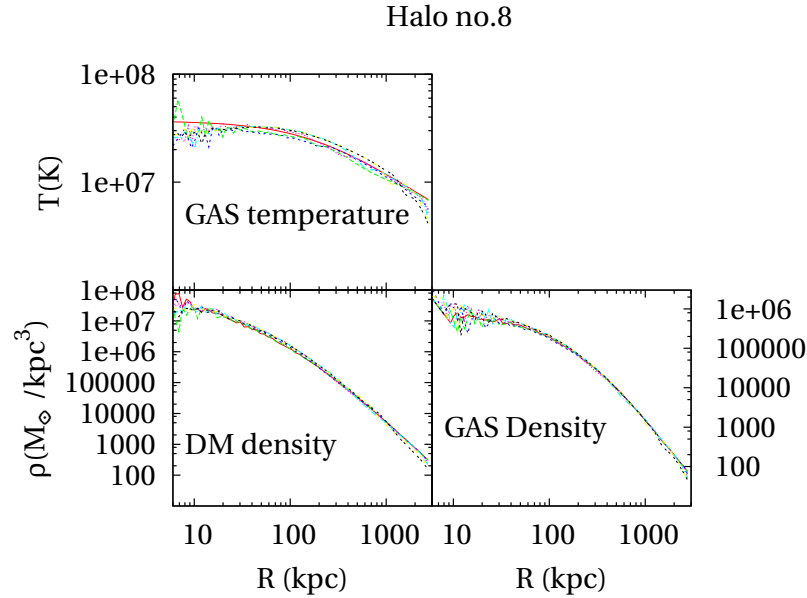
Halo no.3

Figure 6.4: Gas temperature profile (*Top panel*), DM density profile *Bottom left panels*, GAS density profile *Bottom right panel* for simulation no.1 (with $6 \cdot 10^4$ particles) evaluated at 7 times in the interval $[0, 10]t_{dyn}$.

Halo no.4

Figure 6.5: Gas temperature profile (*Top panel*), DM density profile *Bottom left panels*, GAS density profile *Bottom right panel* for simulation no.1 (with $6 \cdot 10^4$ particles) evaluated at 7 times in the interval $[0, 10]t_{dyn}$.
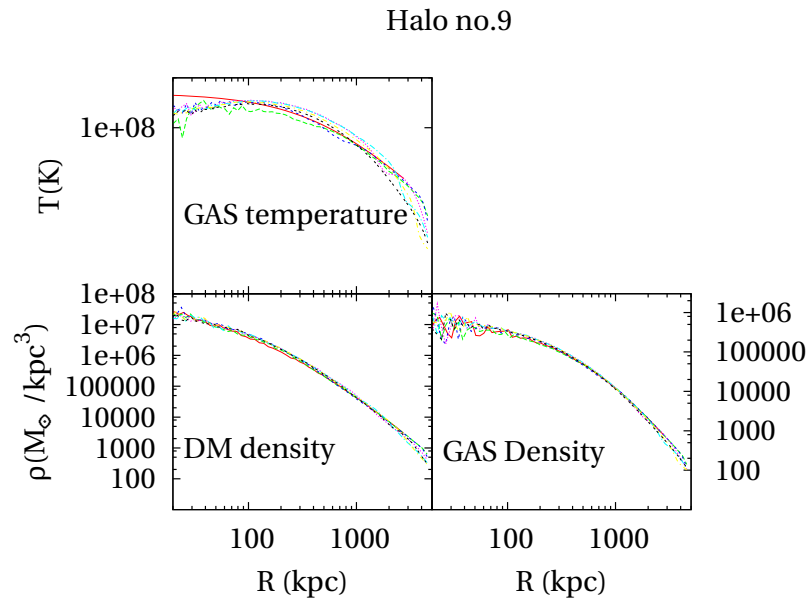
Figure 6.6: Gas temperature profile (*Top panel*), DM density profile *Bottom left panels*, GAS density profile *Bottom right panel* for simulation no.1 (with $6 \cdot 10^4$ particles) evaluated at 7 times in the interval $[0, 10]t_{dyn}$.
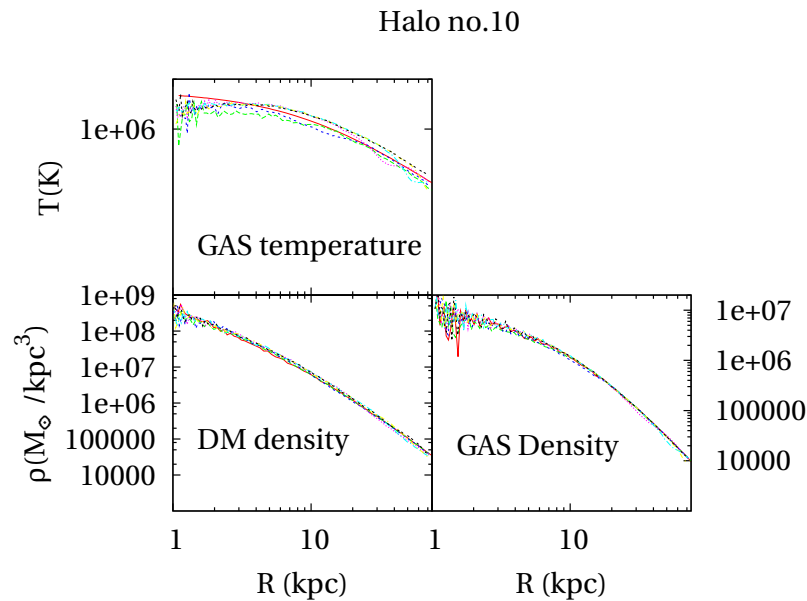

Figure 6.7: Gas temperature profile (*Top panel*), DM density profile *Bottom left panels*, GAS density profile *Bottom right panel* for simulation no.1 (with $6 \cdot 10^4$ particles) evaluated at 7 times in the interval $[0, 10]t_{dyn}$.

Halo no.7

Figure 6.8: Gas temperature profile (*Top panel*), DM density profile *Bottom left panels*, GAS density profile *Bottom right panel* for simulation no.1 (with $6 \cdot 10^4$ particles) evaluated at 7 times in the interval $[0, 10]t_{dyn}$.

Halo no.8

Figure 6.9: Gas temperature profile (*Top panel*), DM density profile *Bottom left panels*, GAS density profile *Bottom right panel* for simulation no.1 (with $6 \cdot 10^4$ particles) evaluated at 7 times in the interval $[0, 10]t_{dyn}$.

Figure 6.10: Gas temperature profile (*Top panel*), DM density profile *Bottom left panels*, GAS density profile *Bottom right panel* for simulation no.1 (with $6 \cdot 10^4$ particles) evaluated at 7 times in the interval $[0, 10]t_{dyn}$.

Figure 6.11: Gas temperature profile (*Top panel*), DM density profile *Bottom left panels*, GAS density profile *Bottom right panel* for simulation no.1 (with $6 \cdot 10^4$ particles) evaluated at 7 times in the interval $[0, 10]t_{dyn}$.

equilibrium. The DM and gas density profiles and the gas temperature profiles, evaluated in the interval $[0, 10]t_{dyn}$ for the halos in Table 1, are plotted in figures 6.1-6.11. Making a comparison between the different simulations we can make general statements :

1. Fixing the effective polytropic index γ and the value of M_{200} we note (see figures 6.1, 6.3, 6.4) that a lowering of the concentration parameter C_{NFW} is reflected in a flattening in the DM and gas profiles;

2. Increasing the effective polytropic index γ with fixed M_{200} and C_{NFW} (see figures 6.1, 6.6) lowers the gas density profile and increase temperature profile.

3. Fixing the effective polytropic index and increasing the value of M_{200} (see figures 6.1, 6.7, 6.8, 6.9, 6.10) we observe that the temperature profiles increase while the density profile starts decreasing at larger radii.

Before starting the description of the radiative simulations we would like to stress other two points. The first one concerns the oscillations in the density profiles for small value of r. They are present in all the twelve halos' profiles and they are due to Poissonian numerical noise. In fact, if we increase the number of particles inside r_{200} (see figure 6.2 and 6.1) we can see how the noise in the profiles tends to vanish. Second point: at the beginning of the evolution (this means more or less until $2.5t_{dyn}$) there is an initial small relaxation of the initial conditions towards a configuration of minimum energy. The particles are re-distributed on the density and temperature profiles until the minumum energy configuration is reached. In particular (see 6.12) a reduction of the spread in the gas density distribution and an increasing of the gas temperature's spread take place. This is due to the two facts: (i) in the initial condition the temperature of all particles is fixed in order to reproduce the profile describe by equation 2.19, while the density is assaigned through a Poissonian sampling of the profile. The code makes then a Poissian sampling of the density profiles (equation 2.17) that causes the spread seen in the first panel of figure 6.12. (ii) the gas mass is not negligible, while it is assumed to be vanishing in euqtaion 2.17.

We found that for all the halos a relaxed configuration is reached after more or less 2.5 dynamical times and therefore we prefer to use as initial conditions for the radiative runs the configuration attained by evolving the non–radiative runs for at least two dynamical times.

We want to stress here that even the relaxed configuration (right panels in figure 6.12) presents a scatter in density, amounting to five per cent and some scatter in temperature, amounting to fifteen per cent. The scatter in the realxed configuration is not simply numerical, as it does not decrease with increasing number of particles. The importance of this scatter will be discussed in the next chapter.
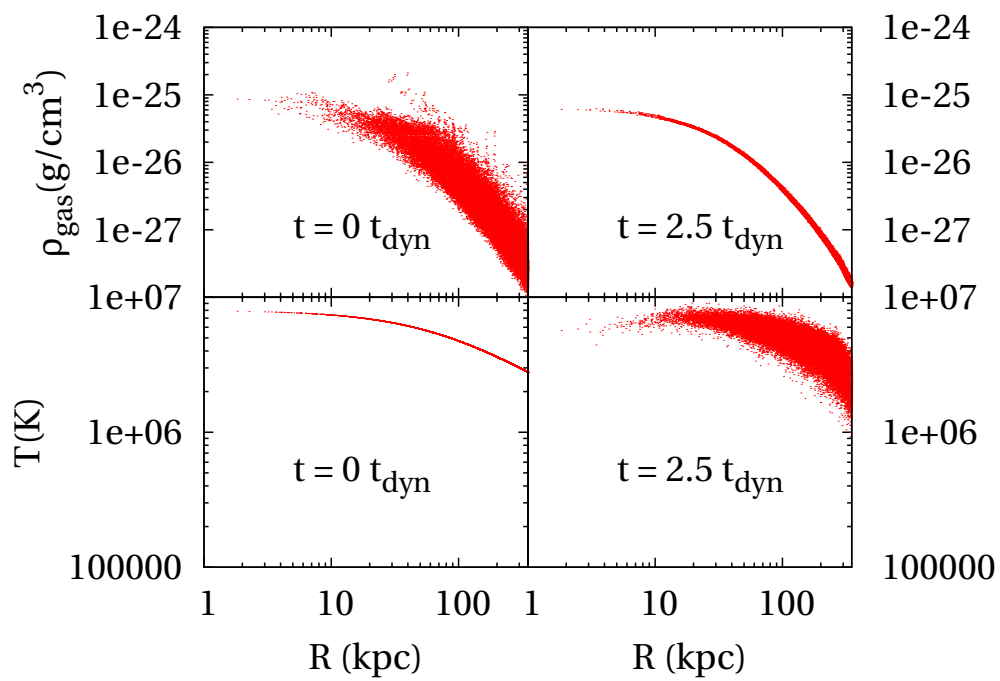
Figure 6.12: *Top panel*: Particles' density at $t = 0$ as assigned in the initial conditions and after $2t_{dyn}$. *Bottom pamels*: Particles' temperature at $t = 0$ as assigned in the initial conditions and after $2t_{dyn}$

6.3   Simulations with radiative cooling

As we mentioned at the beginning of this chapter our aim is to study what happens in the isolated halos if we turn on cooling. We selected eight significant halos from Table 1, five at redshift $z = 0$, the two at redshift $z = 1$ and the one at $z = 2$. We chose these halos because they are rappresentative of interesting astrophysical situations, such as elliptical galaxies, galaxy groups and galaxy clusters. As we stressed at the end of the previous section, the initial conditions for this new set of simulations are the configurations attained at two dynamical times by the non–radiative simulations. Once cooling is turned on, all the simulations are let evolving for 8 cooling time. This second set of simulations are very expensive in terms of computational time. In order to make the simulations faster we decided to introduce in the code also a very easy criterium for star formation: when a gas particle reaches a temperature below $3 \cdot 10^4 K$ it is converted into a collisionless star particle. In this way at each time step the SPH calculation has to be done over a smaller number of particles while the computation of the coldest and densest particles is switched off. We verified that the cold gas fraction in the simulations with star formation opened and closed (see figure 6.13) is exactly the same. Finally, in order to follow in details the trajectories of gas particles in the phase diagram, while they are undergoing cooling, we have implemented a conservative criterion of time–stepping, in which the maximum time–step allowed for a gas particle is one tenth of its cooling time.
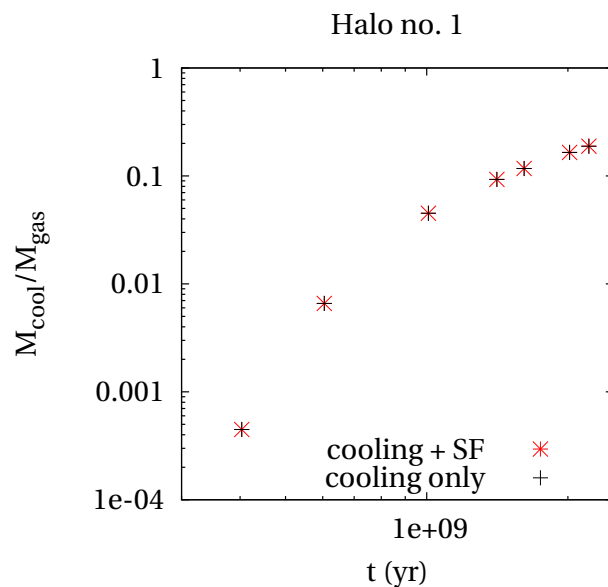

Figure 6.13: Cooling mass fraction calculated in simulation no.1 when star forrmation is turned off (red points) and when star formation is turned on (black point)
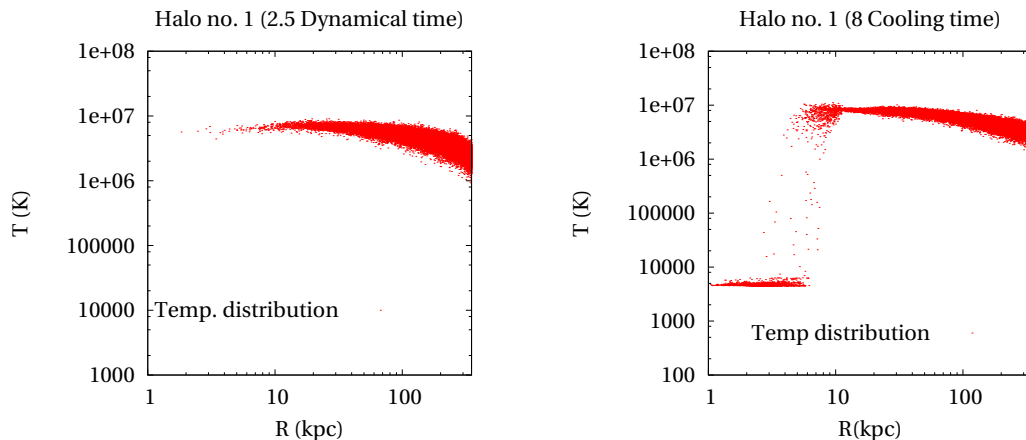
Figure 6.14: *First panel :* Particles' temperature at 2.5 t_{dyn}. This is the initial condition for the radiative simulation. *Second panel :* Particles' temperature at 8 t_{cool}.

6.4 Qualitative analysis of the radiative simulations

Up to now we have described only the characteristics and the main details of our radiative simulations. In this section we will give a phenomenological description of gas behaviour when radiative cooling is turned on. All the plots in the following will be refered to the reference halo (no. 1 in Table 1) where only radiative cooling is turned on (i.e no conversion of cold particles into stars).

Let us start by considering figure 6.14. In the left panel we plot the temperature initial condition for the radiative run (we recall that this situation corresponds to the configuration attained by evolving the non–radiative runs for 2.5 dynamical times). In the second panel we show the configuration achieved after 8 cooling times with the cooling turned on. At this point we are not interested in a quantitative analysis of the phenomena, while we are interested in a qualitative discussion of the gas behaviour. The first comment is that it is easy to identify two well separated phases: a cold one with temperature below $10^4 K$ and a hot one with temperature higher than $10^6 K$. The "warm" phase is essentially vanishing (there are only few particles with temperature between 10^4 and $10^6 K$, negligible in term of mass contribution). In the following we will refer to the particles with a temperature lower than $10^4 K$ as "cold mass". Due to this well defined separation between the two phases it is not difficult to define in the simulation a "cooling radius", or a "cooling region", as the region where there is the transition between the hot and the cold phase. This point will be crucial in the following.

Quite similar considerations can be done when considering figure 6.15, where instead of considering the particles' temperature we consider the density of the particles. Once again it is easy to find a criterium in density to separate the hot
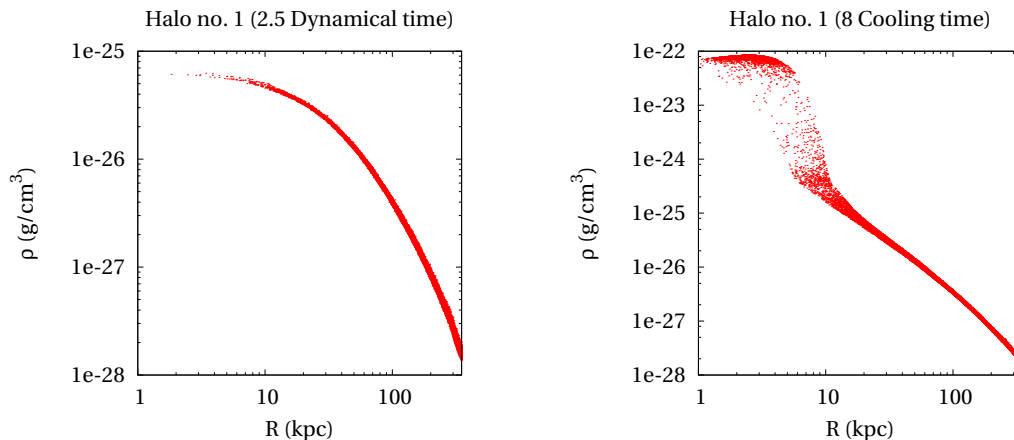
Figure 6.15: *First panel :* Particles' density at 2.5 t_{dyn}. This is the initial condition for the radiative simulation. *Second panel :* Particles' density at 8 t_{cool}.

and cold phase ($\rho < 10^{-24} g/cm^3$), and as in figure 6.14 it is easy to define a "cooling region". Moreover if we take into account a phase diagram of density vs temperature (figure 6.16) it is clear that in order to select the cold particles it is enough to put a limit in temperature: infact all the particles cooler than $10^4 K$ are the same particles denser than $10^{-24} g/cm^3$.

6.5 Tracing particle trajectories

In order to have a better comprehension of the simulations we study the evolution of thermodynamical properties of individual particles randomly selected in three distance intervals from the center (10-20 kpc, 30-40 kpc and 50-60 kpc) in the initial conditions. As before, we report the results obtained for the reference simulation (no. 1 in Table 1). For the other simulations analized we found similar behaviours for the thermodynamics properties of the gas.

In Figure 6.17 we plot the evolution of the temperature as a function of time (left panels) and radial coordinate (right panels) for five particles per distance bin. The vertical line in the right panels denotes the dimension of softening. The behaviour of the particles is very clear: each particle mantains its initial temperature for some time (that depends on its density and initial distance from the center) and then, in a very short time interval, it cools down to a temperature below $10^4 K$, where the cooling function drops. This means that the cooling takes place quite rapidly and therefore, as we have stressed in the previous section, a small number of "warm" particles ($10^4 < T < 10^6 K$) are present in the snapshots. As in figure 6.14 and 6.15 it is possible to identify a "cooling region" as the spherical shell where the drop in temperature takes place. It is interesting to note that this region is more or less the same for all the particles independently of their initial position. Once the particles have cooled down, they continue moving towards the center until they reach the
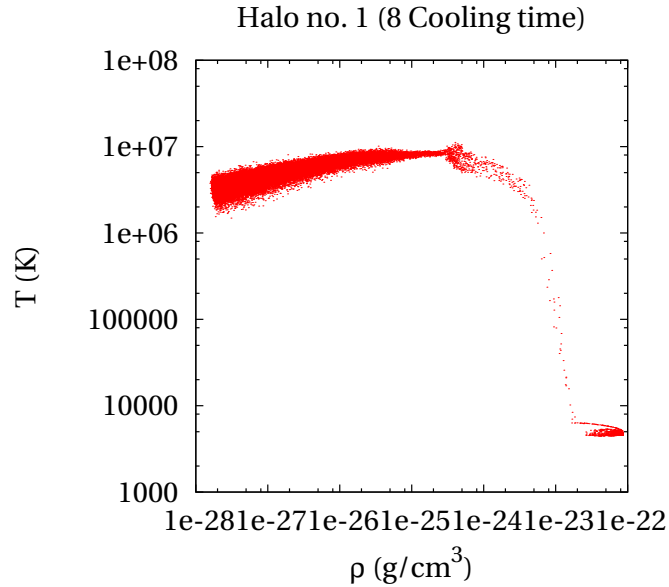
Figure 6.16: Phase diagram density vs temperature for all the particles at 8 cooling times.

softening scale (see figure 6.17, right panels). Then they start orbiting around the center at about the same scale. Similar conclusions are reached when density is considered in place of temperature.

However, as it is clear from figure 6.18, when a particle moves towards the center of the halo, before reaching the "cooling region" it increases its density by more than one order of magnitude (while its temperature remains almost constant).

We show finally the evolution of the cooling time (figure 6.19, left panels) and its variation as a function of radius (figure 6.19, right panels).

The cooling time is computed from the density and the temperature of the gas, consequently its behaviour is easly understandable once the behavior of temperature and density is known. In particular, we note how the variation of cooling time depends essentially on the variation of the density as it is expected from its definition.

The infall of cooled gas from the cooling region to the center of the halo, where star formation is supposed to take place, is not well resolved by our simulations. In any case it is worth to notice that the transport of the gas from its initial position to the center of the halo takes place mostly while the gas is still hot.
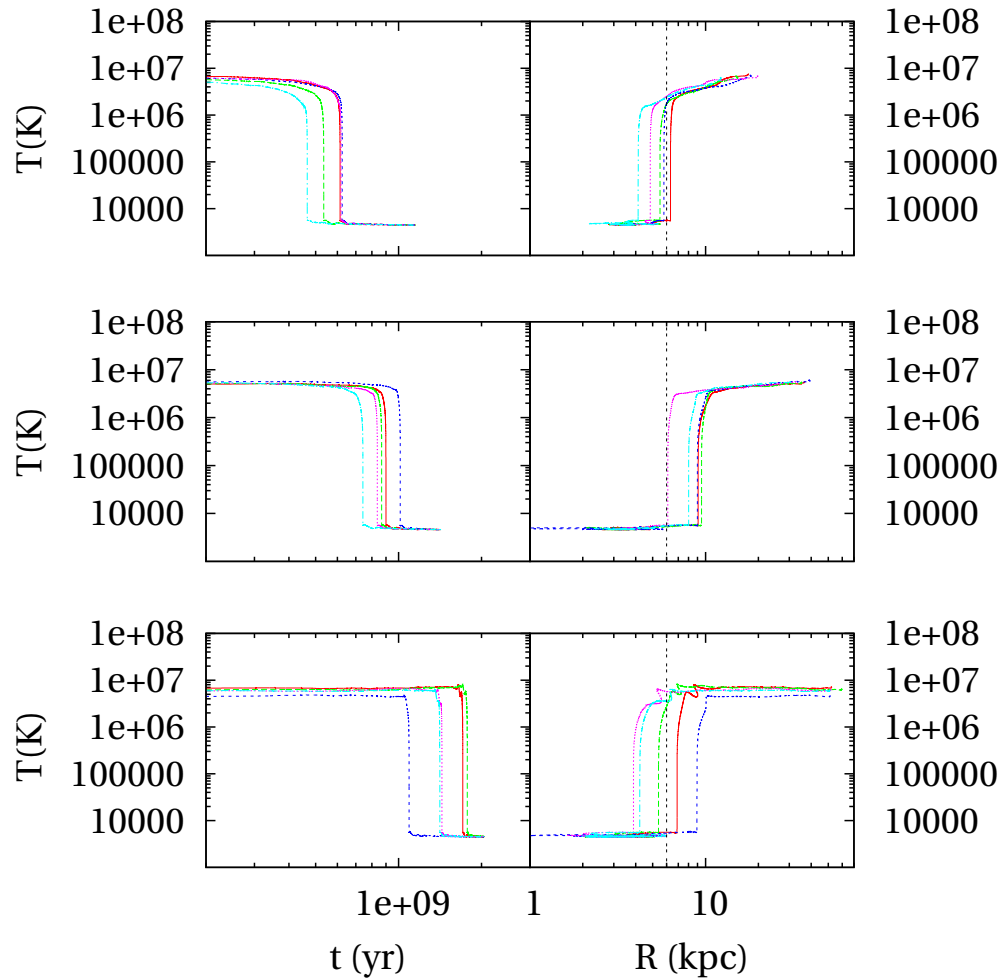
Figure 6.17: Temperature variation as funcion of time (left pannels) and as function of radius (right pannels) for five particles selected in three different shells. *First*: $(r_{min}, r_{max}) = (10, 20)$ kpc. *Second*:$(r_{min}, r_{max}) = (30, 40)$ kpc. *Third*: $(r_{min}, r_{max}) = (50, 60)$ kpc.
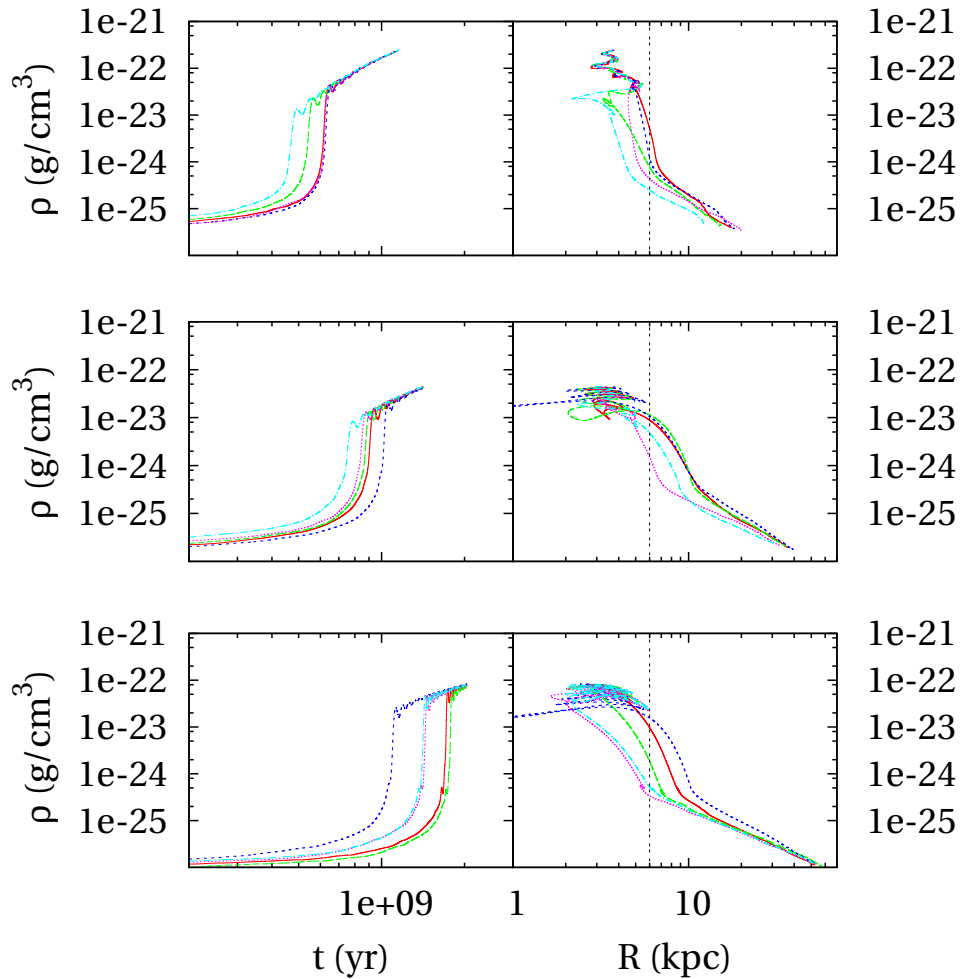
Figure 6.18: Density variation as funcion of time (left pannels) and as function of radius (right pannels) for five particles selected in three different shells. *First*: $(r_{min}, r_{max}) = (10, 20)$ kpc. *Second*:$(r_{min}, r_{max}) = (30, 40)$ kpc. *Third*: $(r_{min}, r_{max}) = (50, 60)$ kpc.
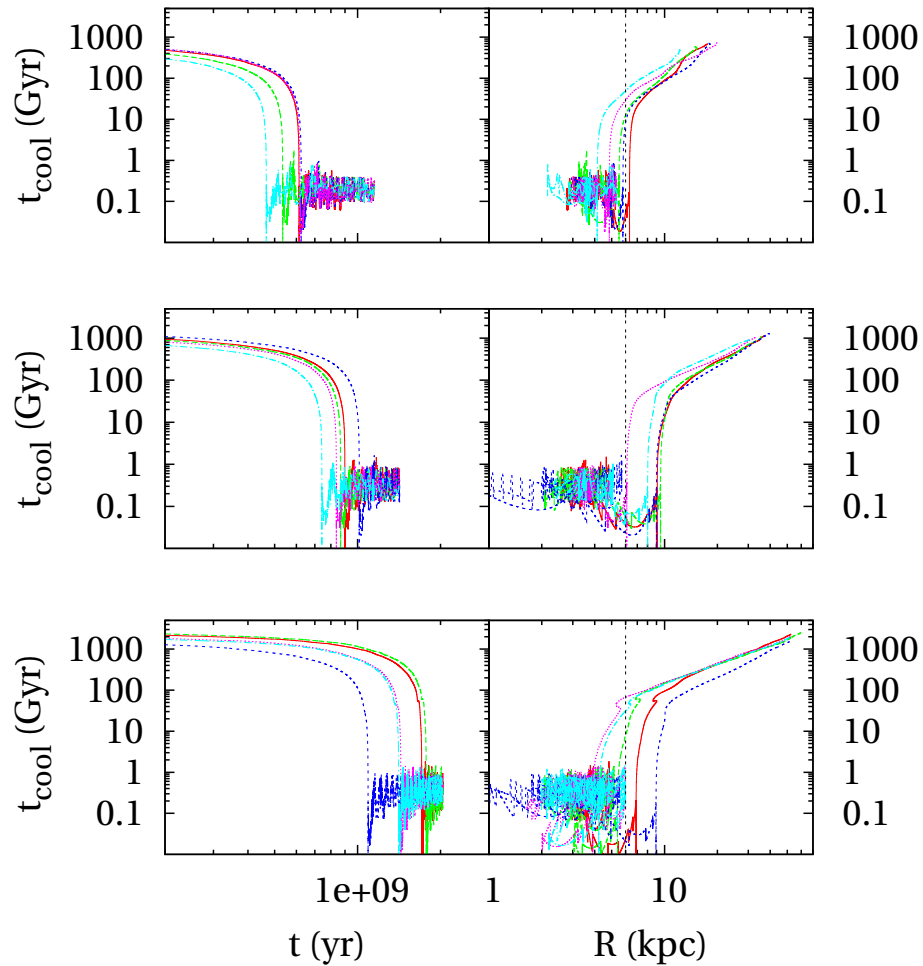
Figure 6.19: Cooling time variation as funcion of time (left pannels) and as function of radius (right pannels) for five particles selected in three different shells. *First*: $(r_{min}, r_{max}) = (10, 20)$ kpc. *Second*:$(r_{min}, r_{max}) = (30, 40)$ kpc. *Third*: $(r_{min}, r_{max}) = (50, 60)$ kpc.

Chapter 7

Cooling: SAMs and numerical simulations

In this chapter we will concentrate on the comparison between the results of the simulations and the predictions of the SAMs. Our goal is to understand radiative cooling of gas in DM halos and to point out which of the "cooling models" described in chapter 2 gives the most reliable representation of the phenomenon. We will discuss in detail simulation 1 of Table 1, the analysis of the other simulations confirms our findings.

7.1   Is cooling isobaric ?

As we discussed in chapter 4, the rigid interpretation of cooling time used by the CM (the gas shell cools in one cooling time) gives a good approximation of the time taken by a parcel of gas to cool down to 10^4 only if the pressure is constant during the evolution. In order to check the validity of this hypothesis we calculate the pressure profiles of the hot gas in the simulation at several epochs.

These are shown in figure 7.1, normalized to the pressure profile evaluated at $t = 0$. Clearly, in the inner parts of the halo pressure increases for a few dynamical times, to saturate later to values that are a factor of five higher just outside the cooling region. This is due to the fact that both the temperature and the density profiles of the hot gas change with time. In particular, as it is shown in figure 7.2, the density profile becomes higher (by about one order of magnitude more) in the inner part while the temperature profile becomes first lower in the inner part and then it tends to reach a shape similar to the initial one or a little bit higher.

Relatively to the initial profiles the largest variation takes place in the density profile.

We conclude that the effect of cooling is to induce a rearrangement of the hot gas. Particular, we have checked that the increase of pressure marks a violation of the hydrostatic equilibrium.

Since the cooling time is inversely proportional to the density, the net result of the increase of the density is a decrease of the cooling time (we will discuss in
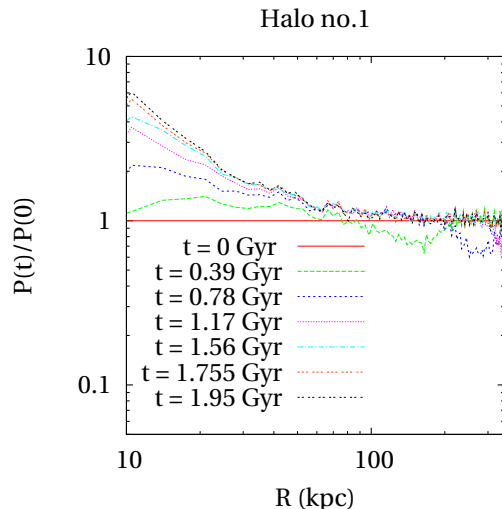
Figure 7.1: Pressure for the hot phase of the gas at different epochs normalized to the pressure at $t = 0$ for the radiative simulation no. 1.

details this point in the following section).

7.2 Simulation versus analytical models

In summary the simulations show that: (i) the drop in temperature from $\sim 10^6$ to $\sim 10^4$ K is quite rapid; (ii) this drop takes place in a spherical shell, the cooling region, which separates the inner and the outer regions respectively dominated by cold and hot particles; (iii) the radius of the cooling region is almost constant with time, (iv) gas evolution is not isobaric, (v) scatter in density and temperature is present.

Are the cooling recipes described in chapter 2 able to reproduce this behaviour?

7.2.1 Initial conditions: SAMs and simulations

In order to answer this question, we first address the tuning of the initial conditions. This is a crucial point because in order to make a reliable comparison between SAMs and numerical simulations we must be sure that the initial conditions are the same. The parameters that determine the density and temperature profiles for the gas are in both case the halo gas mass M_{200}, the effective polytropic index γ, and the central temperature of the gas (in unit of the virial one) η.

As we have seen in chapter 6, the gas in the simulations tends to rearrange itself, therefore it is not obvious in principle that the value of γ and η set in the initial conditions are the same as in the relaxed configuration, while the mass M_{200} is a much more stable quantity. In order to find the "real" value of γ and η in the simulations we have taken 900 choices for the pair of parameters (γ, η) varying both the effective polytropic index and the energy factor in the range $[1.1 : 1.4]$. We have
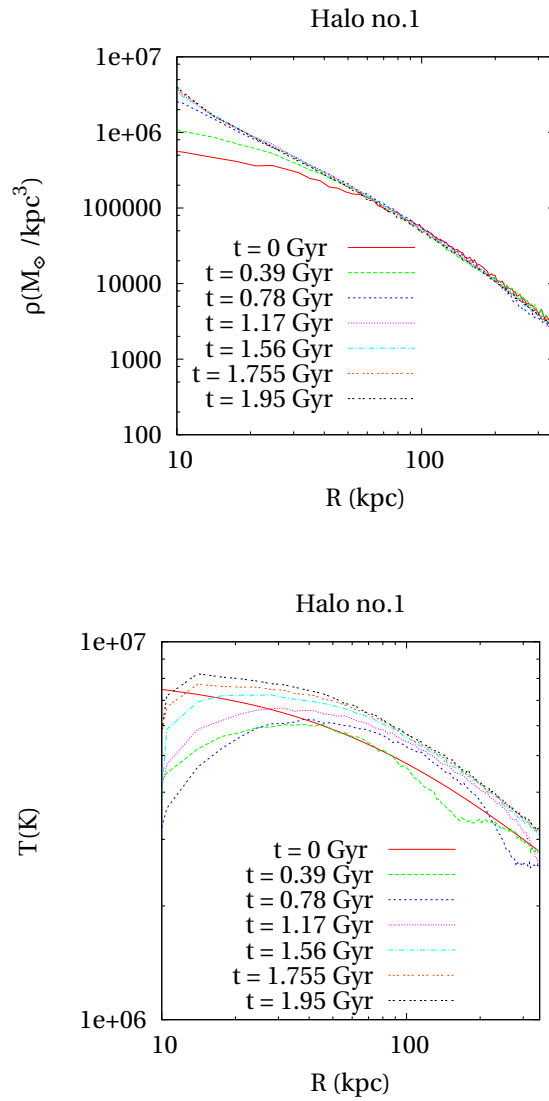
Figure 7.2: Gas density (*first panel*) and temperature (*second panel*) profiles at different times for the radiative simulation no. 1
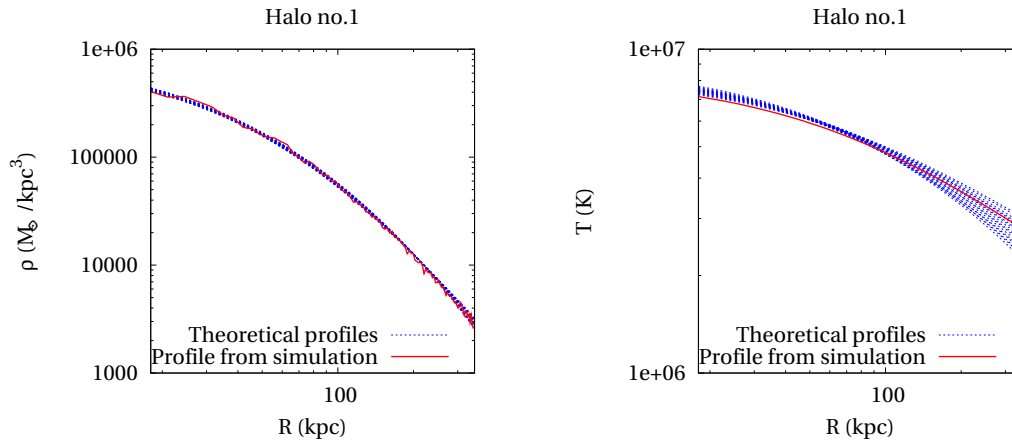
Figure 7.3: Initial gas density (*first panel*) and temperature (*second panel*) profile for simulation no. 1. The red line is the profile as calculated from the simulation, while the blue lines represents all the theoretical models that satisfy to the criterion described in the text.

calculated then for each pair the theoretical profiles (density and temperature, Π_{th} thereafter) and we compared them with the profiles from simulations (Π_{sim} thereafter). The criterium used to choose the pair of parameters that better reproduce Π_{sim} is quite simple. First of all we evaluated :

$$\Delta(r_{bin}) = |\Pi_{sim}(r_{bin}) - \Pi_{th}(r_{bin})| \tag{7.1}$$

where r_{bin} can assume values from 0 to r_{200}. The bins' number have been chosen in order to map well P_{sim}. We computed then $max(\Delta(r_{bin}))$ and we imposed that :

$$\max(\Delta(r_{bin})) = \Delta(r_{bin_\star}) < \frac{1}{10}\Pi_{sim}(r_{bin_\star}) \tag{7.2}$$

This means requiring that the maximum difference between Π_{sim} and Π_{th} will be smaller than the difference between Π_{th} and $\Pi_{th} \pm 10\%$.

We have performed this calculation both for the density and for the temperature profile. In this way, for each halo we obtained at the end two sets of theoretical models, one that reproduces quite well the density profile and one the temperature profile. In order to have the pairs of parameters that are able to reproduce both profiles we choose the intersection between the two sets. The results for the simulation no. 1 are shown in figure 7.3.

7.3   Results

Once we are sure that the initial conditions are the same, we perform two comparisons between analytical models and simulations. The first comparison concerns the

evolution of the cooled mass fraction, the second one the evolution of the cooling radius. In particular, reproducing the cooled mass fraction of simulations is clearly the critical test for the models. Since the cooling radii are defined differently in the classical, Unclosed and Closed MORGANA models, their ability to reproduce a stable cooling region allows us to shed further light on the hypothesis on which the models are based on, and thus to answer to the questions addressed in the previous section.

7.3.1   Cooled mass fraction

In figure 7.4 and 7.5 we plot the predicted cooled mass fraction for all the simulations. For each run we plot the simulated cooled mass with black triangles; the prediction of the three models (classical, Unclosed and Closed MORGANA) is denoted with a colored area (red, magenta and green respectively). The areas are calculated taking into account all the models that reproduce within 10% the initial conditions in the simulation according to the criteria described in the previous section.

We have checked that the result is stable versus the number of particles used to sample the initial profile and versus the gravitation softening used in the simulation. In particular in figure 7.6 we plot, for simulation no. 1, the cold mass fraction using $6 \cdot 10^4$ and $6 \cdot 10^5$ particles respectively inside R_{200}. It is clear that, apart from a small initial transient, the result is the same. In figure 7.7 we plot the cold mass fraction using for the gravitational softening the values of 6 and 3 kpc respectively. Also in this case the two simulations converge quite soon.

We draw the following conclusions :

1. The classical cooling model (red area in figure 7.4 and 7.5) underestimates systematically the fraction of cooled gas, especially at early times.

2. The unclosed MORGANA model (magenta area) follows in a much closer way the cooled mass at early times. The onset of cooling is by construction sharp. Therefore, much more gradual accumulation the first 10^{-3} fraction of cooled gas, which takes place over a time-scale shorter than the central cooling time (especially for halo no. 9), is not reproduced. At epochs ranging from 1 to a few central cooling times the fit is very good in most cases. Later, the simulated cooled mass is underestimated.

3. The closed MORGANA models behaves very similarly to the unclosed one for a few central cooling times, then gives a higher fraction of cooled mass that fits nicely the results of simulations.

The reason why the classical model underestimates the cooled gas fraction are the following.

1. As we have discussed in section 6.2, initial conditions of simulations show an intrinsic scatter in temperature and density.
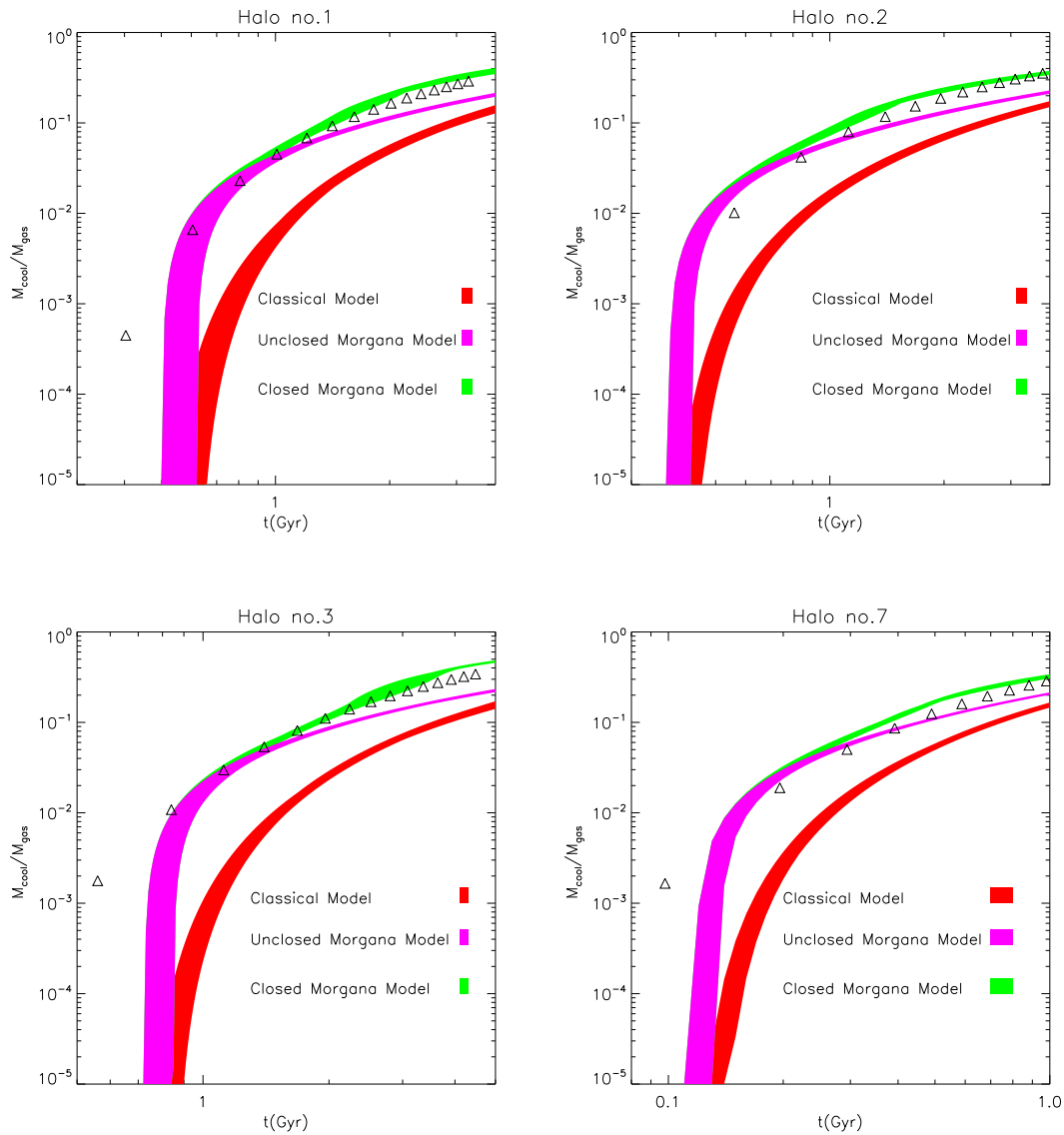
Figure 7.4: In the four panels we plot the cooled gas fraction for the simulations number 1, 2, 3, 7 until 8 t_{cool}. The dot black points are the simulations result while the colored lines are the predictions of the three different models. In particular red lines represent the MORGANA model (MM), blue lines the Closed MORGANA model (CMM) and the magenta lines the classical model (CM). We plot for each halo all the theoretical models (obtained by changing γ and η) that reproduce the initial conditions in the simulations according to the criteria described in section 7.2.1 .
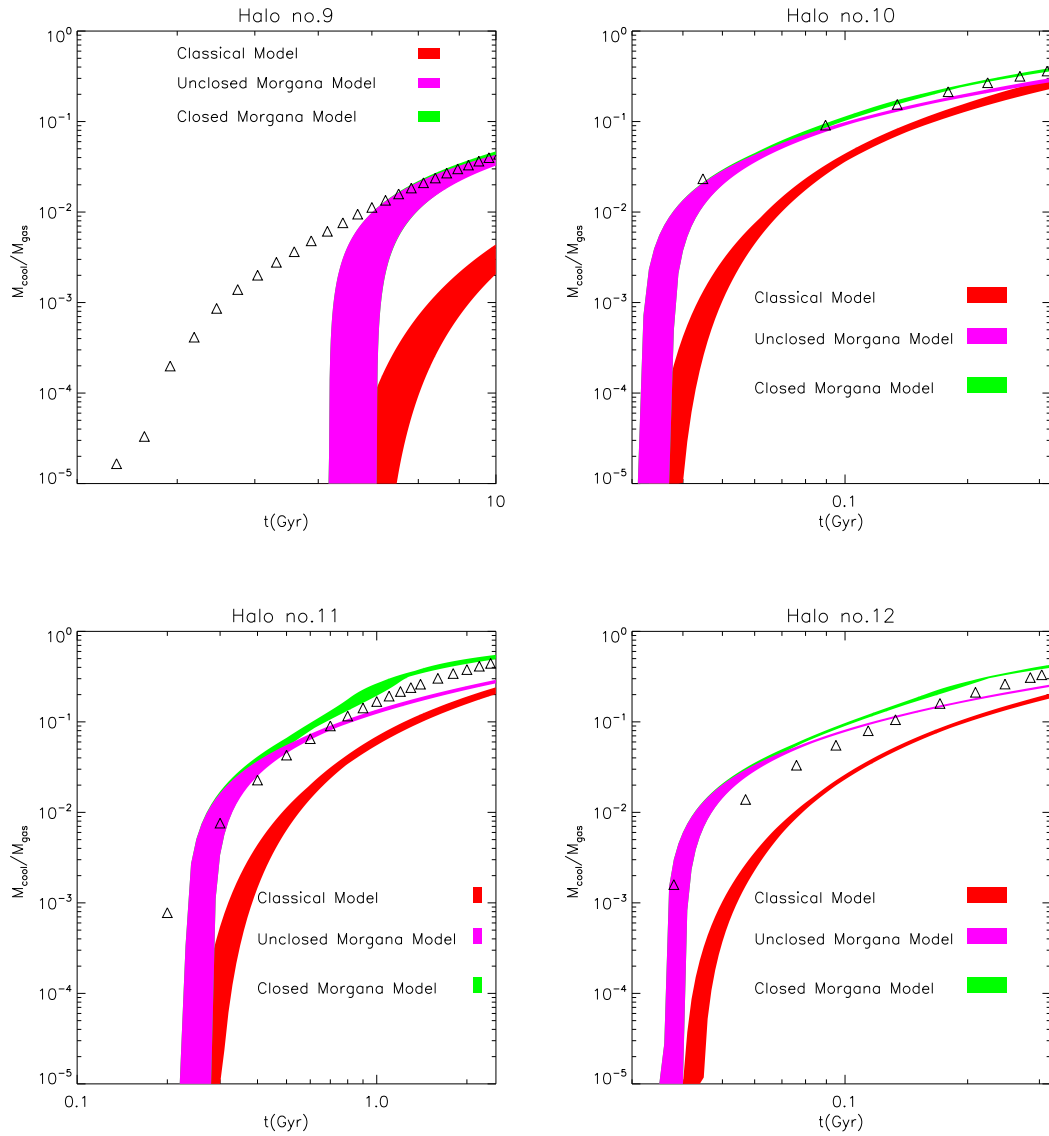
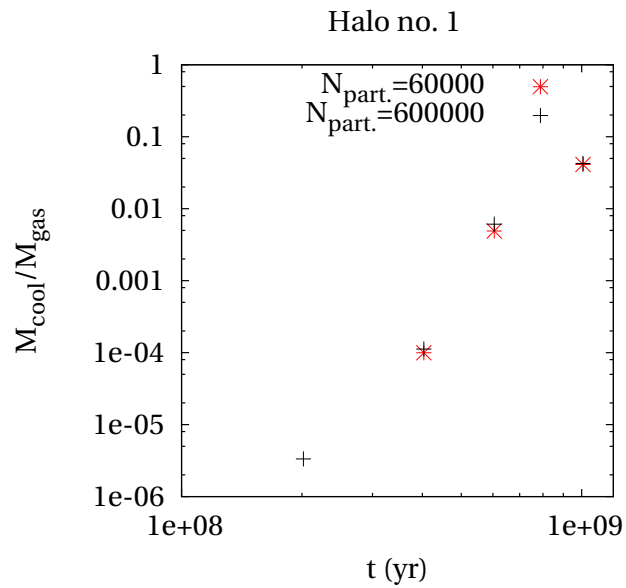Figure 7.5: As in figure 7.4, but for simulations number 9, 10, 11, 12.

Figure 7.6: Cooling mass fraction calculated in simulation no.1 using respectively $6 \cdot 10^4$ (red dots) and $6 \cdot 10^5$ (black dots) particles inside R_{200}. The plot shows the result up to the convergence between the two cases.
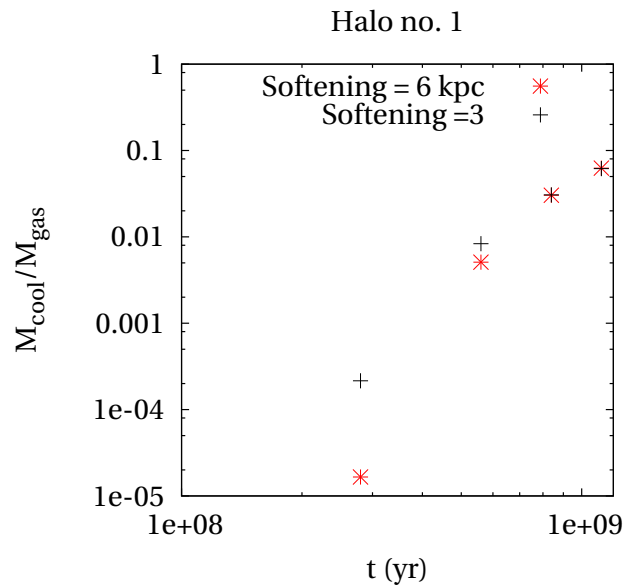

Figure 7.7: Cooling mass fraction calculated in simulation no.1 using as softening respectively 6 (red dots) and 3 (black dots) kpc. The plot shows the result up to the convergence between the two cases.
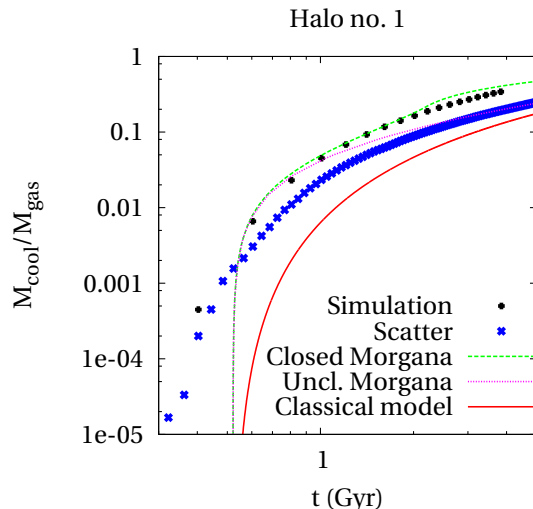
Halo no. 1

Figure 7.8: Evolution of the cold gas fraction as predicted by the three models. In particular red line represents the "classical model", magenta line the "Unclosed MORGANA model" and the green line the "Closed MORGANA model". We overplot with black dots the results of the simulation and with blue cross the fraction of cooled mass estimated by computing the number of particles of the (relaxed) initial conditions that have a cooling time shorter than the time considered.

Let us suppose that each particle cools down exactly after its initial cooling time (this is not true as we have stressed before). According to the classical model, at a time $t_\star$ all possible contributions to the cold phase come from the gas lying at $r < r_{cool}(t_\star)$. However, due to the scatter in the density distribution, there are some particles, lying at $r > r_{cool}(t_\star)$ and with a central cooling time smaller than $t_\star$, that contribute to the cold phase. Therefore, especially at the beginning, when the gas density profile is rather flat at the center, there is a large number of particles lying outside the cooling radius that contribute to the cooling flow and that are not considered by the classical model.

On the other hand, the MORGANA model, although it moves from the same definition of cooling time, assumes that the cooling rate of each mass shell is proportional to the mass of the hot gas in the shell divided by its cooling time, making no assumption on the time the shell takes to cool down. This allows, at a certain time $t_\star$, to take into account the contributions from the gas at $r > r_{cool}(t_\star)$. Clearly, this fact is important if we want to reproduce the simulations, especially at the beginning where, due to the flatness of the density profile, and the scatter in the density of particles, there are a lot of particles at $r > r_{cool}(t_\star)$ with a cooling time shorter than $t_\star$, that contribute at $t_\star$ to the cold mass.

The quantitative effect of the scatter is shown if figure 7.8, where the fraction
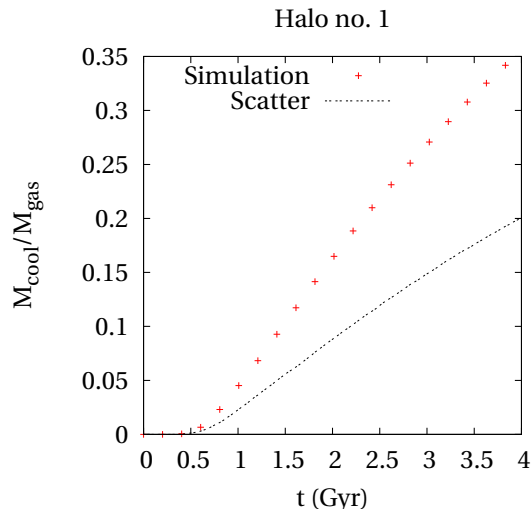
Figure 7.9: Cold gas fraction obtained from simulation (red dots) and estimated by computing the number of particles of the (relaxed) initial conditions that have a cooling time shorter than the time considered (black line). The scale here is not logarithmic.

of cooled mass was estimated by computing the number of particles of the relaxed initial conditions that have a cooling time shorter than the time considered. In other words we applied to the particles in the simulation the idea on which the classical model is based. By definition, if the scatter is negligible, we sholuld find exactly the same result of the classical model prediction. Instead we have found that the result is always above the classical model. In particular it coincides well with the cooled mass of the simulation at early time and falls below the results of the simulation later (see in particular figure 7.9). The reason of this behavior will soon be clear.

We conclude that the scatter in the actual thermodynamical variables of gas particles is especially important at early times, but it cannot fully explain the difference between the classical model and the simulations.

2. The rigid prediction of the classical model that each gas shell cools to 10^4 K in exactly one cooling time (computed on the initial conditions) is roughly valid only in the case of isobaric cooling, which clearly does not apply to our case as the hot gas falling toward the cooling region is subject to an increase in pressure. We have checked this point by verifying also that the cooling times of the particles in the simulation, calculated using their initial temperature and density, are always larger than the times need to reach $T = 10^4 K$. In more formal terms, while the evolution of the cooling radius r_C in the classical model is obtained by simply inverting the cooling time function, the equation for the minimal radius r_M of the MORGANA model is obtained by the weaker assumption that the cooling region is always sharp.

As we have already discussed, the increase in pressure is due to an increase in density, and an increase in density means a decrease in the cooling time. Consequently, not taking into account the increase in density, amounts to predict a slower cooling flow and a smaller amount of cold gas. The increase of gas pressure is the reason why in figure 7.8 the cold mass fraction, computed by applying to the initial condition of simulation the prescription of classical model, coincides with the cooled mass of simulation at early time (when the increase in pressure is negligible) and falls below later (when the increase in pressure is important).

We want to stress that both scatter and increase of pressure are not explicitly taken into account by the MORGANA model, and its success should be ascribed simply to the relaxation of the strongest assumptions of the classical model.

Finally, in the Closed MORGANA model the gas profile, which is recomputed at each time step (see section 4.4), changes with time as the gas flows toward the cooling region. The predicted density profiles are shown in figure 7.10 for simulation no.1 at 0.8 and 1.56 Gyr, together with the initial and simulated profiles. Consistently with the simulation, the density in the closed MORGANA model tends to increase at the border of the cooling region, but this agreement is only qualitative at the beginning, and the quantitative agreement present at 4 dynamical times is soon lost when the closing of the cooling hole is halted (see section 4.4). Nonetheless, this model correctly predicts a higher cooling flow in this range. The most significant difference comes from the different estimate of the cooling radius (visible in figure 7.10): since $r_{M,ch} < r_M$, even for a constant density profile, the density at the border of the cooling region, and thus the cooling flows, is always higher in the closed model, and this effect is more relevant than the increase in the density profile visible in figure 7.10.

7.3.2   Evolution of the cooling radius

So far we have only described the evolution of the cooling gas fraction. However the three models make also predictions about the evolution of the cooling radius. In particular, the improvements in the fit of cooled mass of the closed MORGANA models versus the classical model reflects in a better description of the dimension of the cooling region in Lagrangian space. In figures 7.11 and 7.12 we plot the temperature and the density of gas particles versus their initial position for three snapshots (at 0.58, 1.36 and 2.15 Gyr) of simulation no.1. Once more we notice that, while the temperature profile remains close to the initial one, density increases with time in the vicinity of the cooling region; this implies that the increase of pressure visible in figure 7.1 is mostly given by an increase in density. Secondly, the Lagrangian size of the cooling region is much better represented by r_M than by r_C. While this is an obvious consequence of the good agreement shown in figure 7.4 and 7.5 (the cooled mass is the integral of the initial profile up to the cooled region), these figures clearly show how the improvement is connected to the looser assumption made on the cooling radius.
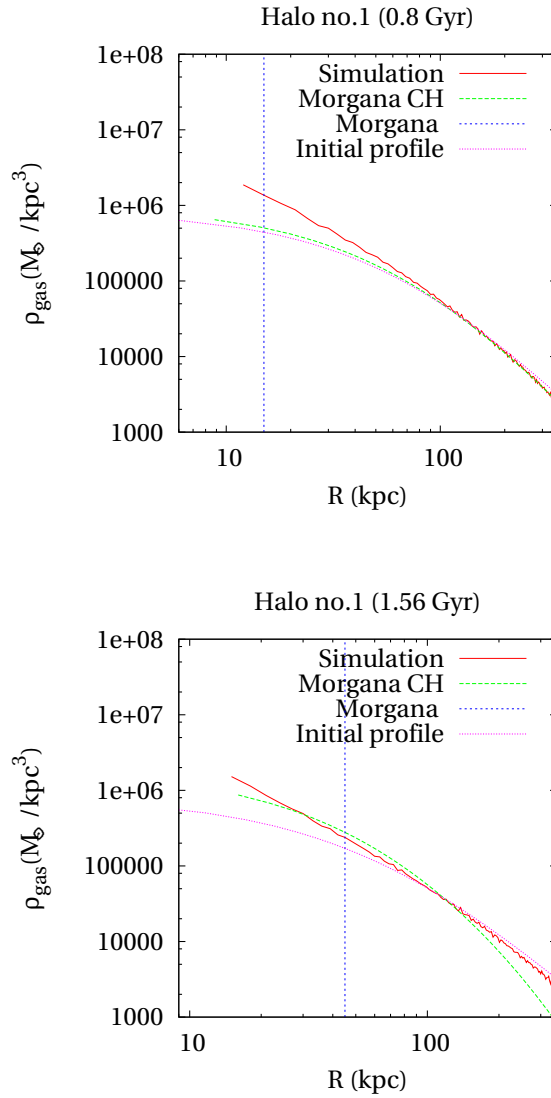
Figure 7.10: The density profile for the hot gas in the simulation number 1 at 2 t_{dyn} (*first panel*) and 4 t_{dyn} (*second panel*). We plot the profile obtained from simulation (red line), the initial theoretical profile (magenta line), the truncation of the theoretical profile at r_{cool} as calculated by MORGANA model (blue line) and the modified profile calculated by the Closed MORGANA Model (green line) truncated to r'_{cool}.
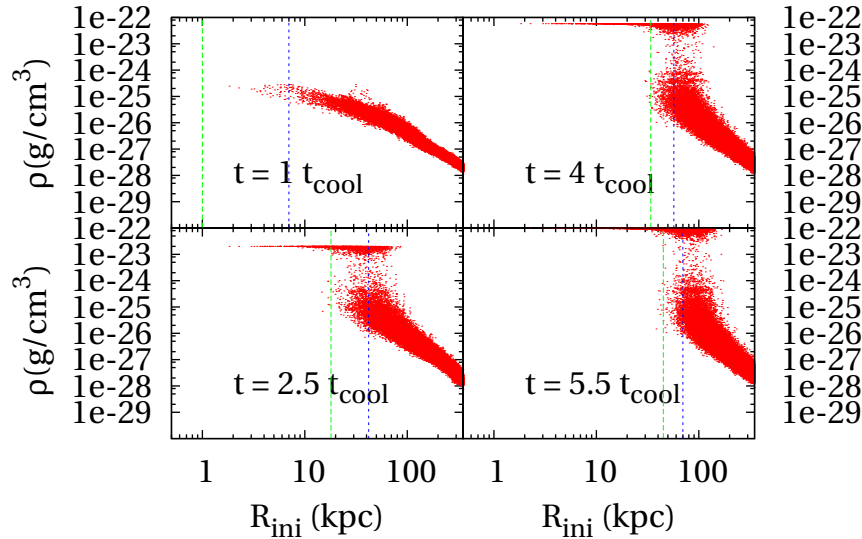
Figure 7.11: Density vs initial positions of gas particles in simulation no.1 at 4 times. We overplot the cooling radius as predicted by "classical model" (*green line*), and the cooling radius as predicted by "MORGANA model" (*blue line*).

In order to perform the same comparison using the prediction of the MORGANA model with the closure of the cooling hole, we plot the density and the temperature of the particles at a given time $t_\star$ in the simulations versus their position at $t_\star$. In fact this model attempts to follow the physical evolution of the system and then the cooling radius should be interpreted as an Eulerian quantity (see figure 7.13). This shows the stability of the cooling region in the Eulerian space, to be compared with the prediction of the closed MORGANA model $r_{M,ch}$. Despite the simplified modeling of the closure of the cooling hole, the closed MORGANA model is able to predict a stable cooling region. Very similar conclusions are drawn by analyzing the corresponding density profiles.

Figure 7.14 and 7.15 shows the predicted values of all cooling radii compared respectively to the size of the Lagrangian and Eulerian regions estimated by computing the point at which the average temperature profile crosses the level 10^4 K. It shows that the better agreement of the r_M radius with the Lagrangian cooling region, with respect to the classical r_C, holds at all epochs, while the good agreement between $r_{M,ch}$ and the Eulerian cooling radius breaks at $t \sim 1.5$ Gyr or ~ 1.5 dynamical times. At this moment the average specific thermal energy of the hot gas, predicted by the closed MORGANA model, drops below the virial value. As explained in section 2.3, if extrapolated further the model predicts a catastrophic cooling of all the hot gas. A good reproduction of the cooled mass is obtained by simply dropping the $-c_s$ term in equation 4.13, i.e. the closure of the cooling hole
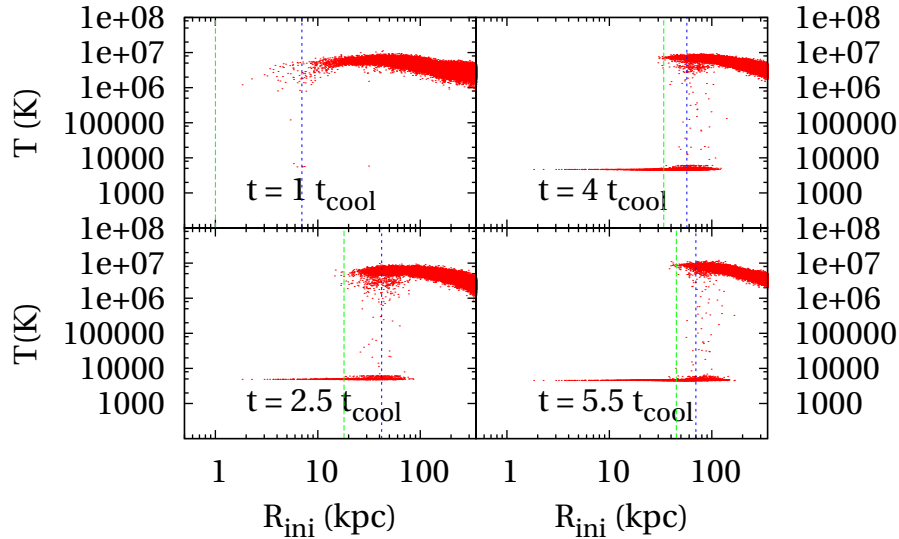
Figure 7.12: Temperature vs initial positions of gas particles in simulation no.1 at 4 times. We overplot the cooling radius as predicted by "classical model" (*green line*), and the cooling radius as predicted by "MORGANA model" (*blue line*).

is suppressed, with the consequence that the prediction of the radius of the cooling hole is spoiled. We have found no simple way to achieve a good fit of both cooled mass and cooling radius; the trick of halting the closure of the cooling hole is then regarded just as a simple, phenomenological way to achieve a good fit of at least the cooled mass fraction.

7.4 Summary

In this section we summarize the main results obtained through the comparison between the predictions of the different cooling recipes and the numerical simulations.

1. The drop in temperature from $\sim 10^6$ to $\sim 10^4$ is quite rapid. This is evident in the study of the variation of the temperature of the particles with respect to time and it is confirmed by the fact that there are only few "warm" particles in the snapshots. Both MORGANA and classical models assuming a sharp border between the hot and the cold phase reproduce this behavior.

2. The classical cooling model systematically underestimates the fraction of cooled mass with respect to simulations, especially at early times (compared to the central cooling time). This disagreement is ascribed to two main facts. Firstly, at early times the scatter in density and temperature of gas particles,
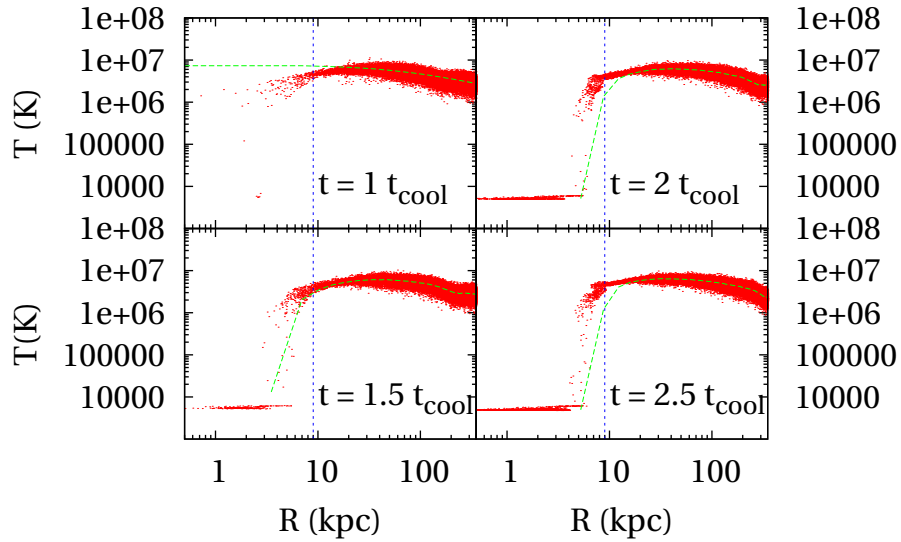
Figure 7.13: Particles' temperature vs particles' positions in simulation no.1 at 4 times. We overplot the cooling radius as predicted by "MORGANA model with the closure of cooling hole" (*blue line*) and the temperature profiles of the gas (*green line*)

Figure 7.14: Evolution of the Lagrangian cooling radii for simulation 1 (triangles), compared to the predicted r_C (classical model),red area, and r_M (unclosed MORGANA model),magenta area. As in figure 7.4 colored areas represent all the theoretical models in agreement with the initial conditions of simulation.

Figure 7.15: Evolution of the Eulerian cooling radius for simulation 1, compared to the predicted $r_{\mathrm{M,ch}}$ (closed MORGANA model). Colored area represents all the theoretical models in agreement with the initial conditions of simulation.
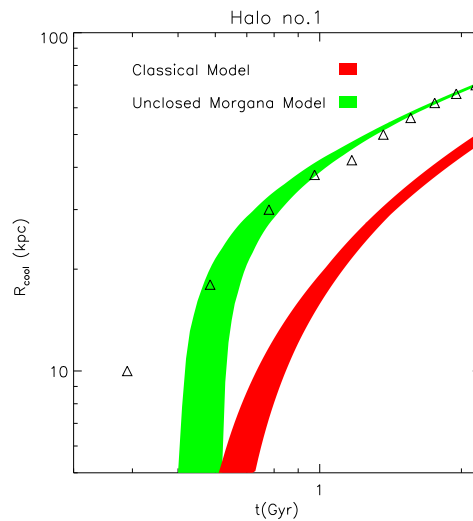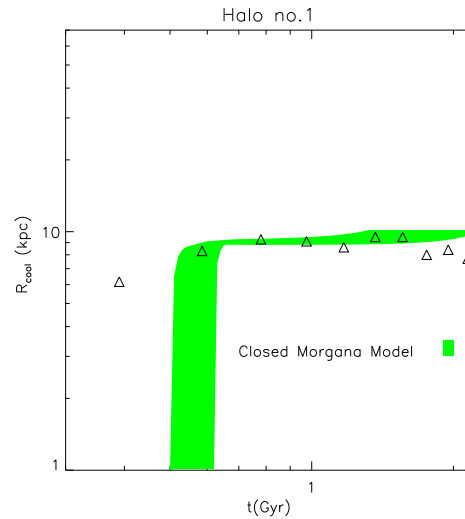
which naturally arises in the relaxed and thermalized gas configuration, increases the number of particles that are subject to early cooling. This effect is enhanced by the flatness of the density profile in the center, so that many shells contribute to cooling at the same time. Secondly, at later times pressure increases just beyond the cooling radius. This increase of pressure hastens the cooling process, so that less than a cooling time is required to a particle to get to 10^4 K (where the cooling function drops).

3. The unclosed MORGANA model gives a much better fit to both the cooled mass fraction and the position of the Lagrangian cooling radius, i.e. the radius which separates the hot and cold phases in the space of initial positions (the Lagrangian space). We are convinced that this improvement is not due to a specific modeling of the two points mentioned above (scatter in density and temperature of particles and increase of pressure) but to a relaxation of the strongest hypotheses of the classical model. In more detail, the "decay equation" (equation 4.8) used for cooling of mass shells implicitly can account (at least to some degree) for scatter in density and temperature. Cooling from several mass shells is esplicitely accounted for, and the equation for the cooling radius r_M does not require to assume that each mass shell cools in exactly one cooling time. These looser assumptions allow us to reproduce the quick onset of cooling (although cooling before the central cooling time is neglected by construction, and this does not allow to account for the first $\sim 10^{-3}$ cooled fraction) and the overall higher cooled mass fraction.

4. The closed MORGANA model further improves the fit of the simulated mass

fraction. Moreover, the predicted cooling radius $r_{\mathrm{M,ch}}$ can be compared with the actual (Eulerian) position of the cooling radius in the simulations. We find that the closed MORGANA model correctly reproduces the initial rapid increase and successive roughly constant value of the Eulerian cooling radius. The main reason for the improvement of the closed with respect to the unclosed model is that the lower value of the cooling radius leads to an increase of the density of the cooling shell, simply because the gas is allowed to stay at smaller radii. The steepening of the density profile as the simulation evolves is reproduced only qualitatively. Unfortunately, the validity of this model breaks as soon as the energy of the hot gas (which decreases due to the decreasing temperature profile) drops below the virial value. In this case we still obtain a good match of the cooled mass fraction by simply dropping the sound speed term responsible for the closing of the cooling hole.

5. The closed MORGANA model gives a good fit, within 20-50 per cent, of the cooled mass fractions for all the simulations presented in this Thesis.

Chapter 8

Conclusion

The main goal of this Thesis was to study in detail the process of radiative cooling of gas in DM halos. Gas cooling is the basic process in galaxy formation due to the fact that it controls the available amount of cold gas that forms the reservoir for star formation. There are two possible approaches to the problem of studying galaxy formation: Semi–Analytical Models and numerical simulations. In the first approach the background cosmological model uniquely predicts the hierarchical build–up of the DM halo and the gas cooling is modelized through very simple recipes. On the contrary numerical simulations follow in details (by integrating the hydrodynamical equations described in chapter 5) the evolution of the cosmic baryons during the shaping of the large scale–cosmic structure. In this Thesis we have compared the two approaches and in particular we used numerical simulations to test the hypothesis on which the different cooling recipes implemented in SAMs are based. The cleanest approach to perform this comparison is to turn-off, both in SAMs and in numerical simulations, the complications associated to the hierarchical merging of the halos (such as the virialization of the gas after a merging) and all the possible physical process, such as feedback mechanisms, that can affect the gas behavior.

We have therefore simulated isolated halos making, for DM and gas component, the same hypotheses on which the cooling recipes in SAMs are based on. In particular we have assumed that the DM density profile can be described by an NFW profile, that the gas is in hydrostatic equilibrium and that a polytropic relation between the gas temperature and density holds. In this way the initial conditions in the simulated halos and in the cooling models are the same and, due to the fact that cooling is the only process turned on, we can perform a reliable comparison of the gas behavior seen in the simulations and the ones predicted by the different recipes.

In the literature it is possible to find two different modeling of gas cooling: the so–called "classical model" (White & Frenk, 1991), implemented in the largest part of SAMs, and the so–called "MORGANA model" (Monaco et al., 2007). They are based on different hypotheses, and therefore they give different predictions for example about the amount of cold gas at a fixed time. The first goal of this Thesis was to clarify the main differences between the two models. We can summarize

them as follow: the classical model assumes that, at a fixed time $t_\star$, the amount of cold gas is given by the integral of the initial density profile up to a radius, called the "cooling radius", which is defined as the radius at which the cooling time (computed on the initial conditions) is equal to $t_\star$. This means that, by definition, it is not possible for a gas shell outside the cooling radius to contribute to the cold mass at $t_\star$. On the contrary, the MORGANA model weights the contribution of a gas shell to the cold mass at a time $t_\star$ with the shell cooling time (calculated on the initial conditions) and then it assumes that a sharp border is anyhow preserved and uses this to compute the cooling radius. In other words, according to the MORGANA model, there is a non–vanishing contribution to the cold mass by all the gas shells. Both these two models, due to the fact that the computation of cold mass fraction is performed starting from the initial density profile and assuming that the temperature profile is constant, assume intrinsically that cooling is isobaric, i.e. that there is no evolution of the pressure profile. We have discussed in Chapter 2 how the assumption that the gas is pressure–supported at the cooling radius is in general false, and in Chapter 7 we have shown that the pressure of the gas in the simulations is not constant in time. Therefore we presented a variation of the MORGANA model, the so–called "Closed MORGANA Model", in which the "cooling hole" is allowed to close at the sound speed. In this way it is possible to follow the evolution of the system in a more detailed way.

Having clarified the differences among the models, we have performed with the `GADGET-2` code a set of simulations of isolated halos in which gas cooling is turned on. For each simulation we have defined a "cold phase" ($T < 10^4 K$) and we calculated the evolution with time of the cold gas fraction. As a first test, we have verified that this quantity is not dependent on the resolution of the simulation and on the choice of gravitational softening, which guarantees the numerical robustness of our results.

We concluded that the best model for gas cooling is the Closed MORGANA Model. This is due to the following facts:

1. The Closed MORGANA Model, as the Unclosed MORGANA Model, does not make any assumption on the time that each gas shell takes to cool down. We have shown how this fact is important if we want to reproduce the simulations. This is especially true at the beginning, when, due to the flatness of the density profile and the scatter in particle density there are a lot of particles at $r > r_{cool}(t_\star)$ with a cooling time shorter than $t_\star$, that contribute at $t_\star$ to the cold mass;

2. The Closed MORGANA Model mimics the increase of the density profiles near the cooling radius that is seen in the simulations. In this way, the computed cooling times are shorter and the cooling rate larger as seen in the simulations.

Once again we want to stress here that the better prediction of MORGANA models with respect to the classical one is neither due to a specific modeling of scatter in temperature and density seen in the simulations, nor to a specific modeling of the increase of pressure. It is rather related to a relaxation of the strongest hypotheses

of the classical model. Therefore MORGANA models must be considered as effective models, which can be used to obtain reliable predictions on the specific aspect of the gas cooling processes, such as the mass deposition rate.

In the wider context of galaxy formation, cooling of hot virialized gas represents the starting point for all the astrophysical processed involved in the formation of stars (and super-massive black holes) and their feedback on the interstellar and intra-cluster media. Clearly, a good modeling of cooling is needed both to obtain reliable results and to limit the freedom of these models. We find that the classical model, used in most semi-analytic models of galaxy formation, leads to a significant underestimate of the cooled mass at early times. This result is apparently at variance with previous claims of an agreement of models and simulations in predicting the cooled mass (Benson et al. (2001); Helly et al. (2003); Cattaneo et al. (2006)). These papers used cosmological boxes with simulated halos and SPH hydrodynamics with cooling and no heating, compared to the results of semi-analytic models run on the simulated merger trees. Given the much higher complexity of the initial conditions used, a direct comparison of the results is hard to perform. Here we only want to stress the advantage of performing simpler and more controlled numerical tests in order to constrain a single process at a time.

It is well possible that the different behavior of simulations and of the classical cooling model is less visible when more complicated initial conditions are considered.

Once the process of cooling has been safely constrained, the approach of this Thesis can be extended by successive sophistication to address many problems. For example it will be possible to simulate the merging of such equilibrium halos to constrain the process of gravitational heating of gas, with particular attention to the time-scale needed for the gas to reach a new equilibrium configuration, or it will be possible to use cooling halos to study feedback from jets emitted by massive black holes accreting mass from the same cooling gas. These studies will eventually lead to a decrease in the parameter freedom of galaxy formation models, and then to a net increase of their predictive power.

Appendix A

Cosmological framework

In this appendix we give the most important equations in cosmology without demonstration and with only a brief discussion. In order to have a more detailed treatment we suggest to read for example Coles & Lucchin (2002) or Peacock & Murdin (2002).

A.1 General relativity and the cosmological principle

Every model for the universe is based on the so called Cosmological Principle, that is the universe is homogeneous and isotropic in its spatial components. The metric for a space-time in which is valid such principle can be written as:

$$ds^2 = (cdt)^2 - a(t)^2 \left[\frac{dr^2}{1 - Kr^2} + r^2(d\vartheta^2 + \sin^2 \vartheta d\varphi^2) \right] \qquad (A.1)$$

Here we use spherical coordinates : r, ϑ, φ are comoving coordinates, t is the proper time, $a(t)$ is the universe expansion factor, K is the curvature parameter and can assume only three value : $1, 0, -1$ (open, flat,closed universe). This metric is called *Robertson-Walker metric*.

With this metric it is possible to solve the Einstein equation for gravitational field:

$$G_{ik} = R_{ik} - \frac{1}{2}g_{ik}R - \Lambda g_{ik} = \frac{8\pi G}{c^4}T_{ik} \qquad (A.2)$$

for a homogeneous and isotropic fluid with pressure p and rest energy density ρc^2. Λ is the so-called "cosmological constant". The solutions are called Friedmann cosmological equations and read, for $\Lambda = 0$, as :

$$\ddot{a} = -\frac{4}{3}\pi G\left(\rho + 3\frac{p}{c^2}\right)a \qquad (A.3)$$

$$\dot{a}^2 + Kc^2 = \frac{8}{3}\pi G\rho a^2 \qquad (A.4)$$

From A.4, we can get the curvature of the universe:

$$\frac{K}{a^2} = \frac{1}{c^2}\left(\frac{\dot{a}}{a}\right)^2\left(\frac{\rho}{\varrho_c} - 1\right) \qquad (A.5)$$

where

$$\rho_c = \frac{3}{8\pi G}\left(\frac{\dot{a}}{a}\right)^2 = \frac{3H^2}{8\pi G} \qquad (A.6)$$

is called critical density and has the value $1.88 \cdot 10^{-29}h^2 g/cm^3$, while the quantity $H(t)$ is called *Hubble constant*. At present time it is parameterized as follow:

$$H_0 = h \cdot 100km \cdot s^{-1} \cdot Mpc^{-1} \qquad (A.7)$$

The space will be closed, open or flat if the density parameter:

$$\Omega(t) = \frac{\rho}{\rho_c} \qquad (A.8)$$

will be grater, smaller or equal to one.

A.2   The density of the universe

The Friedmann equations are valid for a perfect fluid and can be solved assuming an equation of state:

$$p = \omega\rho c^2 \quad with \ \ 0 \le \omega \le 1 \qquad (A.9)$$

where $\omega = 0$ for collisionless non–relativistic matter, $\omega = 1/3$ for radiation and $\omega = -1$ for the vacuum.

If we assume that the expansion of the universe is adiabatic we can write:

$$d(\rho a^3) = -3\frac{p}{c^2}a^2 da \qquad (A.10)$$

Solving together equations A.8and A.9 we get:

$$\rho a^{3(1+\omega)} = const. \qquad (A.11)$$

If we consider now a non relativistic fluid ($\omega = 0$) we have :

$$\rho_m = \rho_{m0}(1 + z)^3 \qquad (A.12)$$

while for the radiation ($\omega = 1/3$) we get:

$$\rho_\gamma = \rho_{\gamma 0}(1 + z)^4 \qquad (A.13)$$

where z is the *redshift* and it is linked to the expansion parameter a in this way:

$$(1 + z) = \frac{a(t_0)}{a(t)} \qquad (A.14)$$

Once the ratio between density and radiation increases with redshift we can conclude that at high z the universe was radiation dominated. The transition between the radiation dominated epoch and the matter dominated one is called *equivalence* ($z \simeq 5900$).

We will report now the solution of the Friedmann equations for some particular cosmological models. All this universe scenario has a time at which $a \to 0$ and consequently $\rho \to \infty$. This singularity in the space-time is called *Big Bang*.

1. Einstein-de Sitter universe (EdS):

$$\Omega_m = 1, \omega = 0 \ (matter \ dominated) \Rightarrow a(t) \propto t^{\frac{2}{3}} \qquad (A.15)$$

$$\Omega_m = 1, \omega = \frac{1}{3} \ (radiation \ dominated) \Rightarrow a(t) \propto t^{\frac{1}{2}} \qquad (A.16)$$

The expansion factor a grows indefinitely with time; moreover an Einstein–de Sitter universe approximates the expansion of flatness universe in the first epochs when the curvature term in Friedmann equation is negligible.

2. Open universe :

$$\Omega_m < 1 \qquad (A.17)$$

As in the previous case the expansion factor grows indefinitely with time. If $\Omega = 0$ it is $a(t) \propto t$. The expansion is linear with time. This kind of universe approximates the expansion of an open universe when $a(t)$ is large, so that the density term is small and the deceleration term ($\ddot{a} \simeq 0$) is negligible.

3. Closed universe :

$$\Omega_m > 1 \qquad (A.18)$$

In this case it is possible to show that, at a certain time, the expansion factor becomes negative. The solution is therefore symmetric with respect time and consequently there are two singularities, the Big Bang and the so–called the Big Crunch

4. de Sitter universe:

$$p = -\rho \qquad (A.19)$$

This situation correspond to the vacuum domination. The expansion is in this case exponential:

$$a(t) \propto exp(Ht) \qquad (A.20)$$

A.3 Standard cosmological model

In this section we will summarize the main points of the standard cosmological model.

1. The expansion of the universe implies the Big Bang singularity;

2. In the first epochs of the universe the baryonic matter was fully ionized and all the particle (photons included) were in thermodynamical equilibrium. Consequently the universe was opaque and we are not able to detect any radiations coming from this epochs;

3. At high redshift the universe was radiation dominated. At $z \simeq 5900$ (*equivalence*) the energy and the matter density were the same. After the equivalence the universe was matter dominated;

4. When the photon temperature became lower than $10^4 K$, proton and electron bounded together into hydrogen atoms and the photons had their last interaction with the baryonic matter. This epoch is called *recombination* ($z \simeq 1090$);

5. From the recombination epoch the primordial photons travelled freely in the universe and their frequencies were shifted into microwaves. Today we observe that photons as the cosmic microwave background (*CMB*). The CMB spectrum confirms that the universe were at the beginning in thermodynamical equilibrium;

6. There are small fluctuations in temperature ($\delta T/T \simeq 10^{-5}$) in the CMB. This fluctuations are induced by the perturbation in the radiation and baryonic field and also in the field of a weak interactive particle that we call *dark matter*. The large scale structure of the universe depends on this small perturbations as it will be discussed in section B;

7. According to observations we live in a flat universe with $\Omega_m \simeq 0.3$ and $\Omega_\Lambda \simeq 0.7$;

There are basically two problems that cannot be solved inside this model:

1. Why the universe is flat ?

2. Why the CMB is isotropic ?

Both this two problems can be solved inside the so called *inflationary theories*. According to these theories after the Big Bang there was an accelerate expansion that amplified the scale factor of the universe of a factor e^{60}. In this way the horizon became smaller in cosmological unit and therefore regions that were before causally connected after this expansion period were causally disconnected. In this way the isotropy of the CMB can be explained. Another effect of the inflation is to stress the curvature term in such a way that today it is not possible to distinguish from a flat to a non–flat universe.

Appendix B

Cosmological perturbations

The main assumption we made in Appendix A to solve the Einstein equation is the homogeneity and isotropy of the universe. Even if this assumption is correct on large scale it is wrong on small scale where we see stars, galaxies, clusters of galaxies not distributed in an homogeneous way. These inhomogeneities can be related to the fluctuations in the temperature field seen in the CMB. In the following we will show the main ideas to describe the time evolution of these small perturbations and consequently the growth of the structures in the universe.

B.1 Gravitational instability

Let us consider a collisionless gas that in Newtonian approximation is possible to describe through the continuity equation, the Euler equation and the Poisson equation:

$$\frac{\partial \rho}{\partial t} + \nabla \cdot \rho \bar{v} = 0 \tag{B.1}$$

$$\frac{\partial \bar{v}}{\partial t} + (\bar{v} \cdot \nabla)\bar{v} + \frac{1}{\rho}\nabla p + \nabla \phi = 0 \tag{B.2}$$

$$\nabla^2 \phi - 4\pi G \rho = 0 \tag{B.3}$$

where ρ is the gas density, $\bar{v}$ is its velocity and p is the pressure. The system has a static solution $\rho = \rho_0$, $\bar{v} = 0$, $p = p_0$ and $\nabla \phi = 0$. The idea is now to perturb infinitesimally that solution and to study the first order solution of the perturbed system. Particularly we are looking for solutions like:

$$\delta u_i = \delta u_{0i} \exp(i\bar{k} \cdot \bar{r}) \exp(i\omega t) \tag{B.4}$$

where i denotes the physical quantity (density, velocity...) and δu_{0i} the amplitude of the perturbation. The system of equations can be solved now by assuming an expanding background and considering the limit $|\delta| \ll 1$. The solution is:

$$\ddot{\delta} + 2\frac{\dot{a}}{a}\dot{\delta} + (v_s^2 k^2 - 4\pi G\rho)\delta = 0 \tag{B.5}$$

where $v_s = \left(\frac{\partial p}{\partial \rho}\right)^{1/2}$ is is the sound speed.

For a collisionless and non-radiative fluid, the solution can be written as:

$$\delta = At^{2/3} + Bt^{-1} \tag{B.6}$$

The evolution of the non–linear perturbations ($\delta >> 1$) can be followed using N–body simulations. In the classical cosmological scenario the formation of the structure is driven by the DM. If the DM is "hot" (i.e. the DM particles decouple when they are still relativistic) the first structures that were formed are clusters of galaxies ($M \sim 10^{15} M_\odot$). This scenario is called *top down* and is not able to reproduce the galaxy distribution at $z = 0$ and the observed galaxy formation at $z \sim 3 - 5$. On the contrary if the DM is "cold" (i.e. the DM particles decouple when they are not relativistic) the scenario can be defined "bottom up": the large scale structure is the result of following merging of small clumps of DM. According to the observations this is the most reliable case.

B.2   Spherical collapse

Let consider a perturbation with an uniform over-density $\langle\delta\rangle$ and radius R. According to the Birchoff theorem the matter outside the sphere doesn't exert any pressure onto the matter inside the sphere. Due to this fact we are able to write the equation of motion for the perturbation radius:

$$\frac{d^2 R}{dt^2} = -\frac{GM}{R^2} = -\frac{4\pi G}{3}\langle\rho\rangle(1 + \langle\delta\rangle)R \tag{B.7}$$

Integrating once this equation we obtain:

$$\frac{1}{2}\frac{dR}{dt} - \frac{GM}{R} = E \tag{B.8}$$

where E is the energy and it is a negative quantity due to the fact that the system is gravitationally bound. This equation has a parametric solution in the form:

$$\frac{R}{R_m} = \frac{1}{2}(1 - \cos\eta) \tag{B.9}$$

and

$$\frac{t}{t_m} = \frac{1}{\pi}(\eta - \sin\eta) \tag{B.10}$$

where R_m is the maximum radius reached by the sphere at t_m. Therefore the perturbation grows until the value R_m is reached and then it starts collapsing. During the collapse pressure gradients and thermal shocks take place and consequently the problem cannot be studied in spherical symmetry. The final state will not be characterized by a singularity, as if the collapse is spherical, but by an extended region with finite density, a certain radius R_{vir} and a mass M. Neglecting mass and

energy loss, and assuming that the over-density is the same at the collapse epoch and at the virialization epoch, we can infer some relations that depend only on the cosmological model. In particular, in the case of an Einstein de Sitter universe, the computation is very easy. Expanding equation B.9 and B.10 in Taylor series at the lower order, we can get:

$$\frac{R}{R_m} = \frac{1}{4}\left(\frac{6\pi t}{t_m}\right)^{2/3}\left(1 - \frac{1}{20}\left(\frac{6\pi t}{t_m}\right)^{2/3} + ...\right) \tag{B.11}$$

The first multiplicative term represents the unperturbed evolution of $R(t)$ for a EdS universe. The mean over-density will be:

$$\langle\delta\rangle = \frac{\rho}{\langle\rho\rangle} - 1 = \frac{(R/R_m)^3_{unp}}{(R/R_m)^3} = \left(1 - \frac{1}{20}\left(\frac{6\pi t}{t_m}\right)^{2/3}\right)^{-3} - 1 \simeq \frac{3}{20}\left(\frac{6\pi t}{t_m}\right)^{2/3} \simeq 1.06 \tag{B.12}$$

The collapse takes place at $t = 2t_m$ and the over-density in the linear theory is therefore:

$$\delta_c = \langle\delta\rangle(2t_m) = \frac{3}{20}(12\pi)^{2/3} = 1.689 \tag{B.13}$$

Once the the collapse is basically non–linear this is not the "correct" value for the critical over-density. It is possible to show that in the case of an EdS universe at $t = t_m$ the non-linear density contrast is $\delta_c(t_m) = 5.55$ and the collapsed structure reaches a radius that is half than the maximum expansion radius and the over-density is $\delta_c(2t_m) = 178$.

Bibliography

Baldry I. K., Glazebrook K., Brinkmann J., Ivezić Ž., Lupton R. H., Nichol R. C., Szalay A. S., 2004, ApJ, 600, 681

Balogh M. L., Baldry I. K., Nichol R., Miller C., Bower R., Glazebrook K., 2004, ApJ, 615, L101

Barnes J., Hut P., 1986, Nature, 324, 446

Baugh C. M., 2006, Reports of Progress in Physics, 69, 3101

Baugh C. M., Cole S., Frenk C. S., 1996, MNRAS, 283, 1361

Baugh C. M., Lacey C. G., Frenk C. S., Granato G. L., Silva L., Bressan A., Benson A. J., Cole S., 2005, MNRAS, 356, 1191

Benson A. J., Bower R. G., Frenk C. S., Lacey C. G., Baugh C. M., Cole S., 2003, ApJ, 599, 38

Benson A. J., Pearce F. R., Frenk C. S., Baugh C. M., Jenkins A., 2001, MNRAS, 320, 261

Binney J., Tremaine S., 1987, Galactic dynamics. Princeton, NJ, Princeton University Press, 1987, 747 p.

Blumenthal G. R., Faber S. M., Primack J. R., Rees M. J., 1984, Nature, 311, 517

Bond J. R., Cole S., Efstathiou G., Kaiser N., 1991, ApJ, 379, 440

Bower R. G., 1991, MNRAS, 248, 332

Bower R. G., Benson A. J., Lacey C. G., Baugh C. M., Cole S., Frenk C. S., 2001, MNRAS, 325, 497

Bower R. G., Benson A. J., Malbon R., Helly J. C., Frenk C. S., Baugh C. M., Cole S., Lacey C. G., 2006, MNRAS, 370, 645

Bryan G. L., Norman M. L., 1998, ApJ, 495, 80

Buchert T., Ehlers J., 1993, MNRAS, 264, 375

Bullock J. S., Dekel A., Kolatt T. S., Kravtsov A. V., Klypin A. A., Porciani C., Primack J. R., 2001, ApJ, 555, 240

Catelan P., 1995, MNRAS, 276, 115

Catelan P., Theuns T., 1996, MNRAS, 282, 455

Cattaneo A., Dekel A., Devriendt J., Guiderdoni B., Blaizot J., 2006, MNRAS, 370, 1651

Cole S., Lacey C. G., Baugh C. M., Frenk C. S., 2000a, MNRAS, 319, 168

Cole S., Lacey C. G., Baugh C. M., Frenk C. S., 2000b, MNRAS, 319, 168

Coles P., Lucchin F., 2002, Cosmology: The Origin and Evolution of Cosmic Structure, Second Edition. Cosmology: The Origin and Evolution of Cosmic Structure, Second Edition, by Peter Coles, Francesco Lucchin, pp. 512. ISBN 0-471-48909-3. Wiley-VCH , July 2002.

Crone M. M., Evrard A. E., Richstone D. O., 1994, ApJ, 434, 402

Croton D. J., Springel V., White S. D. M., De Lucia G., Frenk C. S., Gao L., Jenkins A., Kauffmann G., Navarro J. F., Yoshida N., 2006, MNRAS, 365, 11

Davis M., Efstathiou G., Frenk C. S., White S. D. M., 1985, ApJ, 292, 371

De Grandi S., Molendi S., 2002, ApJ, 567, 163

Dekel A., Silk J., 1986, ApJ, 303, 39

Dubinski J., Carlberg R. G., 1991, ApJ, 378, 496

Efstathiou G., Frenk C. S., White S. D. M., Davis M., 1988, MNRAS, 235, 715

Efstathiou G., Jones B. J. T., 1979, MNRAS, 186, 133

Eke V. R., Navarro J. F., Frenk C. S., 1998, ApJ, 503, 569

Fall S. M., Efstathiou G., 1980, MNRAS, 193, 189

Fillmore J. A., Goldreich P., 1984, ApJ, 281, 1

Firmani C., Avila-Reese V., 2000, MNRAS, 315, 457

Fontanot F., Monaco P., Cristiani S., Tozzi P., 2006, MNRAS, 373, 1173

Frenk C. S., White S. D. M., Davis M., Efstathiou G., 1988, ApJ, 327, 507

Gao L., Springel V., White S. D. M., 2005, MNRAS, 363, L66

Gingold R. A., Monaghan J. J., 1977, MNRAS, 181, 375

Granato G. L., De Zotti G., Silva L., Bressan A., Danese L., 2004, ApJ, 600, 580

Gross M. A. K., Somerville R. S., Primack J. R., Holtzman J., Klypin A., 1998, MNRAS, 301, 81

Gunn J. E., Gott J. R. I., 1972, ApJ, 176, 1

Harker G., Cole S., Helly J., Frenk C., Jenkins A., 2006, MNRAS, 367, 1039

Helly J. C., Cole S., Frenk C. S., Baugh C. M., Benson A., Lacey C., 2003, MNRAS, 338, 903

Helly J. C., Cole S., Frenk C. S., Baugh C. M., Benson A., Lacey C., Pearce F. R., 2003, MNRAS, 338, 913

Hernquist L., 1993, ApJS, 86, 389

Hernquist L., Katz N., 1989, ApJS, 70, 419

Hoffman Y., 1988, ApJ, 328, 489

Hoffman Y., Shaham J., 1985, ApJ, 297, 16

Holmberg E., 1941, ApJ, 94, 385

Hoyle F., 1949, MNRAS, 109, 365

Hoyle F., 1953, ApJ, 118, 513

Jenkins A., Frenk C. S., White S. D. M., Colberg J. M., Cole S., Evrard A. E., Couchman H. M. P., Yoshida N., 2001, MNRAS, 321, 372

Kato T., 1976, ApJS, 30, 397

Kauffmann G., Charlot S., 1994, ApJ, 430, L97

Kauffmann G., Heckman T. M., White S. D. M., Charlot S., Tremonti C., Peng E. W., Seibert M., Brinkmann J., Nichol R. C., SubbaRao M., York D., 2003, MNRAS, 341, 54

Kauffmann G., White S. D. M., Guiderdoni B., 1993, MNRAS, 264, 201

Komatsu E., Seljak U., 2001, MNRAS, 327, 1353

Lacey C., Cole S., 1993, MNRAS, 262, 627

Lacey C., Cole S., 1994, MNRAS, 271, 676

Larson R. B., 1974, MNRAS, 169, 229

Lemson G., Kauffmann G., 1999, MNRAS, 302, 111

Lucy L. B., 1977, AJ, 82, 1013

Makino N., Sasaki S., Suto Y., 1998, ApJ, 497, 555

Markevitch M., Forman W. R., Sarazin C. L., Vikhlinin A., 1998, ApJ, 503, 77

Martin C. L., 1997, ApJ, 491, 561

Martin C. L., 1998, ApJ, 506, 222

Martin C. L., 1999, ApJ, 513, 156

Menci N., Fontana A., Giallongo E., Grazian A., Salimbeni S., 2006, ApJ, 647, 753

Mo H. J., Mao S., White S. D. M., 1998, MNRAS, 295, 319

Monaco P., Fontanot F., Taffoni G., 2007, MNRAS, 375, 1189

Monaco P., Theuns T., Taffoni G., 2002, MNRAS, 331, 587

Monaghan J. J., 1992, ARAA, 30, 543

Monaghan J. J., Lattanzio J. C., 1985, A&A, 149, 135

Moore B., Governato F., Quinn T., Stadel J., Lake G., 1998, ApJ, 499, L5+

Moutarde F., Alimi J.-M., Bouchet F. R., Pellat R., Ramani A., 1991, ApJ, 382, 377

Nagai D., Kravtsov A. V., 2005, ApJ, 618, 557

Nakamura T. T., Suto Y., 1997, Progress of Theoretical Physics, 97, 49

Navarro J. F., Frenk C. S., White S. D. M., 1995, MNRAS, 275, 720

Navarro J. F., Frenk C. S., White S. D. M., 1996, ApJ, 462, 563

Navarro J. F., Frenk C. S., White S. D. M., 1997, ApJ, 490, 493

Navarro J. F., Hayashi E., Power C., Jenkins A. R., Frenk C. S., White S. D. M., Springel V., Stadel J., Quinn T. R., 2004, MNRAS, 349, 1039

Ott J., Walter F., Brinks E., 2005, MNRAS, 358, 1453

Peacock J., Murdin P., 2002, Encyclopedia of Astronomy and Astrophysics

Peacock J. A., Heavens A. F., 1990, MNRAS, 243, 133

Peebles P. J. E., 1969, ApJ, 155, 393

Peebles P. J. E., 1970, AJ, 75, 13

Peebles P. J. E., 1980, The large-scale structure of the universe. Research supported by the National Science Foundation. Princeton, N.J., Princeton University Press, 1980. 435 p.

Peebles P. J. E., 1982, ApJ, 263, L1

Percival W. J., Scott D., Peacock J. A., Dunlop J. S., 2003, MNRAS, 338, L31

Poli F., Giallongo E., Menci N., D'Odorico S., Fontana A., 1999, ApJ, 527, 662

Power C., Navarro J. F., Jenkins A., Frenk C. S., White S. D. M., Springel V., Stadel J., Quinn T., 2003, MNRAS, 338, 14

Press W. H., Schechter P., 1974, ApJ, 187, 425

Preto M., Tremaine S., 1999, AJ, 118, 2532

Quinn P. J., Salmon J. K., Zurek W. H., 1986, Nature, 322, 329

Quinn T., Katz N., Stadel J., Lake G., 1997, ArXiv Astrophysics e-prints

Reed D. S., Bower R., Frenk C. S., Jenkins A., Theuns T., 2007, MNRAS, 374, 2

Rees M. J., Ostriker J. P., 1977, MNRAS, 179, 541

Romeo A. D., Portinari L., Sommer-Larsen J., 2005, MNRAS, 361, 983

Rybicki G. B., Lightman A. P., 1986, Radiative Processes in Astrophysics. Radiative Processes in Astrophysics, by George B. Rybicki, Alan P. Lightman, pp. 400. ISBN 0-471-82759-2. Wiley-VCH , June 1986.

Saro A., Borgani S., Tornatore L., Dolag K., Murante G., Biviano A., Calura F., Charlot S., 2006, MNRAS, 373, 397

Sheth R. K., Mo H. J., Tormen G., 2001, MNRAS, 323, 1

Sheth R. K., Tormen G., 2004, MNRAS, 350, 1385

Somerville R. S., Primack J. R., 1999, MNRAS, 310, 1087

Somerville R. S., Primack J. R., Faber S. M., 2001, MNRAS, 320, 504

Springel V., 2005, MNRAS, 364, 1105

Springel V., Frenk C. S., White S. D. M., 2006, Nature, 440, 1137

Springel V., White S. D. M., Jenkins A., Frenk C. S., Yoshida N., Gao L., Navarro J., Thacker R., Croton D., Helly J., Peacock J. A., Cole S., Thomas P., Couchman H., Evrard A., Colberg J., Pearce F., 2005, Nature, 435, 629

Springel V., Yoshida N., White S. D. M., 2001, New Astronomy, 6, 79

Sutherland R. S., Dopita M. A., 1993, ApJS, 88, 253

Suto Y., Sasaki S., Makino N., 1998, ApJ, 509, 544

Vikhlinin A., Markevitch M., Murray S. S., Jones C., Forman W., Van Speybroeck
L., 2005, ApJ, 628, 655

Warren M. S., Abazajian K., Holz D. E., Teodoro L., 2006, ApJ, 646, 881

Warren M. S., Quinn P. J., Salmon J. K., Zurek W. H., 1992, ApJ, 399, 405

Wechsler R. H., Zentner A. R., Bullock J. S., Kravtsov A. V., Allgood B., 2006,
ApJ, 652, 71

White M., 2002, ApJS, 143, 241

White S. D. M., 1976, MNRAS, 177, 717

White S. D. M., 1984, ApJ, 286, 38

White S. D. M., Frenk C. S., 1991, ApJ, 379, 52

White S. D. M., Rees M. J., 1978, MNRAS, 183, 341

Wu K. K. S., Fabian A. C., Nulsen P. E. J., 2000, MNRAS, 318, 889

Yoshida N., Stoehr F., Springel V., White S. D. M., 2002, MNRAS, 335, 762

Zaroubi S., Naim A., Hoffman Y., 1996, ApJ, 457, 50

Zhu G., Zheng Z., Lin W. P., Jing Y. P., Kang X., Gao L., 2006, ApJ, 639, L5

Zurek W. H., Quinn P. J., Salmon J. K., 1988, ApJ, 330, 519

Acknowledgments

Non è facile scrivere quest'ultimo capitolo della mia Tesi di laurea specialistica, sia perchè sono tante le persone da ringraziare (e non vorrei dimenticarne qualcuna), sia perché vuol dire mettere la parola fine alla mia esperienza di studente universitario e anche ad un lungo periodo della mia vita passato nella mia città natale.

Grazie mamma e grazie papà! Grazie anzitutto per avermi messo al mondo, grazie per l'amore che in questi anni mi avete sempre dimostrato. Grazie per avermi saputo trasmettere l'importanza dell'impegnasi (anche a costo di sacrifici) sia nello studio che nella vita. Grazie per avermi sempre spronato a mettere a frutto le mie capacità senza cercare scorciatoie cercando sempre di puntare in alto. Grazie infine per avermi lasciato sempre libero di scegliere la strada che credevo migliore per me, senza mai mettermi i bastoni tra le ruote!

Grazie Elisabetta e grazie Federico! Grazie per la pazienza che avete avuto con me nelle piccole cose di ogni giorno e scusatemi se in questi anni sono stato poco con voi a causa dello studio e degli impegni associativi.

Non posso non ringraziare in questa circostanza tutti gli amici dell'Azione Cattolica e del Movimento Studenti in particolare, con cui tanto tempo,quasi tutto il tempo libero, ho passato in questi anni. Non potrò dimenticare la vostra amicizia e i tanti campi, convegni e incontri pensati e realizzati assieme. Non potrò nemmeno dimenticare la tante, talvolta forse troppe, riunioni fatte assieme che mi hanno fatto capire il valore aggiunto di lavorare in squadra mettendo in gioco le proprie idee. Ringrazio tra tutti, due in particolare, con cui ho condiviso la mia responsabilità di segretario diocesano e di incaricato regionale. Grazie Stefano e Peo per esservi fatti carico, quando io causa l'università non ho potuto essere presente, delle numerose cose da fare e grazie per la vostra fede limpida e la vostra bella amicizia!

Voglio ringraziare poi i miei compagni di università con i quali ho condiviso le fatiche, spesso le arrabbiature, ma anche i momenti belli di questi 5 anni prima al dipartimento di fisica e poi a quello di astronomia. Voglio ringraziarli per la loro amicizia e per avermi spesso fatto vedere le cose da un punto di vista diverso e talvolta opposto al mio. In particolare voglio ringraziare Paolo, compagno di viaggi, di discussioni serrate e di chiaccherate sul nostro futuro (e un po' anche di sano babezo!); Enrico il "saggio" e il moderato del trio che con i suoi NI alla fine metteva d'accordo tutti (o quasi). Grazie poi al Tava, con il quale ho seguito tutti i corsi della Laurea Specialistica e con il quale abbiamo preparato, spesso in modo scanzonato e facendoci vicendevolmente coraggio, quasi tutti gli esami. Grazie alla paziente Denija che ha sopportato i miei strali sul mondo e sull'università, e che

soprattutto negli ultimi mesi della Tesi mi è stata vicina in osservatoro quando sembrava che tutto dovesse andare storto.

Un grazie speciale va al mio relatore, Stefano Borgani. Grazie per tutte le cose che mi hai insegnato, grazie per la pazienza e per le correzioni che mi hai fatto senza mai urlare, grazie per essere riuscito a trasmettermi la tua passione e dedizione per la ricerca. Grazie ancora perché, pur non condividendo fino in fondo il mio desiderio di andare a fare il Phd all'estero, non mi hai fatto pesare questa decisione. Grazie ai miei due correlatori, Pierluigi Monaco e Giuseppe Murante. Grazie Pierluigi per la pazienza nell'ascoltarmi ogni volta che mi veniva in mente una possibile interpretazione dei modellini di cooling e per tutte le volte che sono venuto nel tuo ufficio ad assilarti con i miei dubbi. Ringrazio Giuseppe invece per avermi accompagnato soprattutto nelle prime fasi di questa Tesi, mettendomi a disposizioni le condizioni iniziali per le "palle" di gas e materia oscura.

Grazie anche a tutti i ragazzi e ragazze del dipartimento che hanno reso piacevoli questi 10 mesi di permanenza in Villa Bazzoni.

Voglio concludere questa lunga lista di ringraziamenti dicendo un grazie speciale agli amici di vecchia data, che mi hanno sostenuto soprattutto nei momenti più difficili e di sconforto durante questi 5 anni di università. Grazie Alessandro, Paolo, Lella, Eliana, Marina, Francesca e Sandra !

Voglio concludere questa mia Tesi con l'ultimo verso del "Sabato del villaggio" di Leopardi che spesso mi è venuto in mente in questi mesi e che è l'augurio che mi faccio per il futuro:

Godi, fanciullo mio; stato soave,
stagion lieta è cotesta.
Altro dirti non vo'; ma la tua festa
ch'anco tardi a venir non ti sia grave.